Detection of Brain Stroke in Simulation and Realistic 3-D Human Head Phantom using Microwave Imaging

Author:
Behnaz Sohani

Supervisors:
Mohammad Ghavami
Gianluigi Tiberi

A thesis submitted in partial fulfilment of
the requirements for the award of
Doctor of Philosophy

in

London South Bank University
Electrical and Electronic Engineering Department

August 2020

Declaration of Authorship

I, declare that this thesis has been written by myself with support of my supervisor. The thesis is submitted for examination in consideration of the award of a degree of Doctor of Philosophy in Electronics and Electrical Engineering. This thesis is my personal effort and that the work has not been submitted for any other degree or professional qualification. I put special effort to ensure that the work is original and to the best of my knowledge, this work has not been taken from other sources except where such work has been adapted, cited, and acknowledged within the text.

Date:

_____

Behnaz Sohani

LONDON SOUTH BANK UNIVERSITY

Abstract

Electrical and Electronic Engineering Department

Doctor of Philosophy

Detection of Brain Stroke in Simulation and Realistic 3-D Human Head Phantom using Microwave Imaging

by Behnaz Sohani

Brain stroke is globally one of the most widespread sorts of brain abnormalities. There are common symptoms between the transient ischemic attack (TIA), strokes and generic medical conditions like fainting, migraine, heart problems and seizures. Therefore, the other health conditions should not be misdiagnosed with stroke. It is well known that providing immediate medical attention for a patient with a brain injury is of vital importance. Every second, from the moment of brain injury, millions of brain cells die, leading to irreparable and permanent damage or even death. Thus, if medical staff diagnose stroke, and perform an appropriate drug treatment within a few hours of the symptoms onset, they play a crucial role in saving a patient's life. The key factor in treatment is to reliably diagnose the stroke immediately. Hence, a portable diagnosic system is pivotal on the spot for rapid diagnosis of brain injuries. Initially, a clinical examination using a neurological assessment is performed by a general practitioner (GP). Compared to CT and MRI scanners, microwave imaging (MWI) can provide a portable detection system, and allow initial diagnosis of various emergency, life-threatening circumstances such as strokes due to brain injury, whilst patients are still being taken by ambulance to hospital, and saving critical time. In recent years, MWI has emerged as a promising non-ionising and non-invasive technology for a range of applications, particularly medical applications. In the current thesis, radar-based MWI is proposed as a procedure for brain haemorrhagic stroke detection. This imaging procedure has also more advantages such as low cost, being portable, fast, and easy to use with a good potential for brain haemorrhage detection. In MWI, the imaging of different human head tissues relies on their different response (i.e., electric contrast) to an applied microwave radiation. MWI is a screening technology for detection and monitoring of

haemorrhagic stroke, tumours and cancerous cells, based on the significant contrast in the dielectric properties at microwave frequencies of normal and abnormal tissues. This thesis deals with the use and validation of an innovative low complexity MWI procedure for brain imaging, where antennas operate in free space. In particular, we employ only two microstrip antennas, operating between 1 and 2 GHz for successful detection of the haemorrhagic stroke. Detection is achieved using both simulation and experimental measurements.

I. In the first stage, a wideband (WB) microstrip antenna with fractal ground plane is proposed, simulated and fabricated for brain haemorrhage detection. The designed antennas exhibit a WB working frequency between 1-2 GHz. This band has demonstrated to be ideal and optimal to do brain imaging; in addition, it is obviously emphasised that WB can enhance performance in lesion detection. The simulations have been performed applying an anthropomorphic human head model where a haemorrhagic stroke has been inserted (using CST Microwave studio). The simulation results concluded that the emulated brain haemorrhagic stroke can be distinguished at four different positions of 0°, 5°, 40°, and 45°.

II. The second stage of this study presents a hemi-ellipsoidal human head phantom with a millimetric cylindrically-shaped inclusion to emulate brain haemorrhage (suitable to be used inside the anechoic chamber) and a human head phantom (suitable to be applied in MWI device). The process has been performed based on the following procedures:

- In the second, stage, first, multi-biostatic frequency-domain measurements have been performed to collect the transfer function (S21) between two proposed mono-static radar system based antennas inside an anechoic chamber using a multi-layered phantom mimicking a human head. This procedure is used to measure the received signal (S21). A Vector Network Analyser (VNA) is linked to the mentioned antennas, and the measured (S21) are recorded when they changed the position to every new observation position. Subsequently, the measured (S21) are post-processed in order to generate microwave images with emphasising the object (e.g. the tumour or the stroke). In this stage, on the basis of the measurement results, it is concluded that the object (brain haemorrhagic stroke phantom) can be successfully detected at four different positions of 0°, 90°, 180° and 270°.

- Secondly, since the results coming from measurements inside the anechoic chamber are not as realistic as clinical trials reports and also there is a medical requirement for a brain

stroke portable imaging device, we have come to a decision on applying different signal pre-processing methods to the imaging results collected from a portable MWI device for brain haemorrhage imaging. A portable MWI device, which operates in free space with two azimuthally-rotating antennas, has been used for brain haemorrhage detection. Measurements are performed by recording the complex (S21) in a multi-bistatic fashion, i.e. for each transmitting position the receiving antenna is moved to measure the received signal every 4.5°, leading to a total of 80 receiving points. In conclusion, based on the results of the MWI device, the inclusion emulating the brain haemorrhage may be detected at four different positions of 0°, 90°, 180° and 270°.

In this thesis, all images have been obtained through Huygens Principle (HP). To reconstruct the image, signal pre-processing techniques are used to reduce artefacts (which may be due to the direct fields and the fields reflected by the first layer). Subtraction artefact removal method between the data of a healthy head and the data of a head with stroke has been initially employed in simulation and measurements. Accordingly, an "Ideal" image would be generated using this artefact removal method to prove the concept of the technology. This would mean that the "Ideal" image performed as a reference for the comparison with the resulting image from using other artefact removal methods. It is important to point out that, for the purposes of real scenario, there is no possibility of applying this artefact removal method to medical imaging, where the ideal response is not calculated or known. Hence, in clinical trials this artefact removal method cannot be helpful. In addition to the subtraction artefact removal method, in this research, four more methods have been introduced and investigated. These methods consist of rotation subtraction, average subtraction, differential symmetric receiver type, and summed symmetric differential. The subtraction and rotation subtraction artefact removal methods have been used both in simulations and measurements. It has been verified that all artefact removal procedures allow detection. Subsequently, 6 dedicated image quantification procedures have been implemented in order to assess the detection capability. These procedures comprise area difference, centroid difference, signal-to-noise ratio, structural similarity index metric, image quality index, and signal-to-clutter ratio. Validation of the techniques through both simulation and experimental measurements have been performed and presented, illustrating the effectiveness of the methods.

List of publications during candidature

Peer-reviewed journal papers:

1. **Sohani, B.**, Khalesi, B., Ghavami, N., Ghavami, M., Dudley, S., Rahmani, A. and Tiberi, G., 2020. Detection of haemorrhagic stroke in simulation and realistic 3-D human head phantom using microwave imaging. Biomedical Signal Processing and Control, 61, p.102001.

2. **Sohani, B.**, Puttock, J., Khalesi, B., Ghavami, N., Ghavami, M., Dudley, S., and Tiberi, G., 2020. Investigation of artefact removal algorithms allowing stroke detection using a dedicated Microwave device. Sensors 2020, 20, 5545.

3. Khalesi, B., **Sohani, B.**, Ghavami, N., Ghavami, M., Dudley, S. and Tiberi, G., 2019. A Phantom Investigation to Quantify Huygens Principle Based Microwave Imaging for Bone Lesion Detection. Electronics, 8(12), p.1505.

4. Khalesi, B., **Sohani, B.**, Ghavami, N., Ghavami, M., Dudley, S. and Tiberi, G., 2020. Free space operating microwave imaging device for bone lesion detection: a phantom investigation. IEEE Antennas and Wireless Propagation Letters (Under review).

Conferences:

1. **Sohani, B.**, Tiberi, G., Ghavami, N., Ghavami, M., Dudley, S. and Rahmani, A., 2019, June. Microwave imaging for stroke detection: validation on head-mimicking phantom. In 2019 PhotonIcs & Electromagnetics Research Symposium-Spring (PIERS-Spring) (pp. 940-948). IEEE.

2. Tiberi, G., Khalesi, B., **Sohani, B.**, Dudley, S., Ghavami, M. and Ghavami, N., 2019, June. Phase-weighted UWB Imaging through Huygens Principle. In 2019 PhotonIcs & Electromagnetics Research Symposium-Spring (PIERS-Spring) (pp. 949-952). IEEE.

3. Puttock, J., **Sohani, B.**, Khalesi, B., Ghavami, M., and Tiberi, G., 2020. UWB Microwave Imaging for Inclusions Detection: Methodology for Comparing Artefact Removal Algorithms. EAI BODYNETS (Accepted).

4. Khalid, B., Khalesi, B., **Sohani, B.**, Dudley, S., Ghavami, M. and Tiberi, G., 2020.3D Breast Phantom Fabrication and Testing Using UWB Microwave Imaging Technology (Submitted).

Contributions by others to the thesis:

I acknowledge the contributions by others to this thesis. Prof. Mohammad Ghavami and Dr. Gianluigi Tiberi as the main supervisors contributed closely in defining the research problem, revising, and directing the thesis. All the antennas and imaging platforms utilised in this thesis are designed partly by Dr. Navid Ghavami.

Statement of parts of the thesis submitted to qualify for the award of another degree:
"None"

Acknowledgements

First of all I would like to express my deep sincere gratitude to my supervisors Prof. Mohammad Ghavami and Prof. Sandra Dudley-McEvoy for their valuable advice, instructions and guidance through the course of my PhD degree.

I am truly grateful to the close supervision of Dr. Gianluigi Tiberi during his fellowship at the London South Bank University in my PhD degree. A huge thank you to Dr. Gianluigi Tiberi, for his guidance, direction and fountain of knowledge in analysing my results.

I am also thankful for the valuable help and guidance provided by Dr. Navid Ghavami.

I would like to say thank you to all staff at London South Bank University, especially Mr. Mehdi Zahir.

I am thankful for the supportive research environment that I have experienced in School of Engineering from Dr. Perry Xiao and Dr. Suela Kellici. In addition, special thanks to London Doctoral Academy (LDA) team represented by, Mr. John Harper, Prof. Peter Doyle, and Mrs. Louise Thompson (Campbell).

I am grateful to my colleagues for their occasional technical help and valuable contribution. I would like to thank all my PhD peers and roommates; James Puttock, Robert Brown, Banafsheh Khalesi, Bilal Khalid, Mahreen Riaz, Maitreyee Dey, and Soumya Parkash Rana. I also thank my close friends Zahra Echresh Zadeh and Fereshteh Hojatisaeidi who morally support me on the PhD journey.

Many thanks to my relatives for their company and kind moral support.

Last but definitely not least, I have to thank my spouse Amir, my beloved parents and my brother Amin for their encouragement, patience and support during the time spent on this project.

Contents

List of Figures

List of Tables

List of Abbreviations

ArD	**Ar**ea **D**ifference
CD	**C**entroid **D**ifference
CST	**C**omputer **S**imulation **T**echnology
CT	**C**omputerised **T**omography
EMTs	**E**mergency **M**edical **T**echnician**s**
FDTD	**F**inite **D**ifference **T**ime **D**omain
GP	**G**eneral **P**ractitioner
HP	**H**uygens **P**rinciple
IT'IS	**I**nformation **T**echnologies **I**n **S**ociety
MRI	**M**agnetic **R**esonance **I**maging
MWI	**M**icro**W**ave **I**maging
MWT	**M**icro**W**ave **T**omography
MEG	**M**agneto **E**ncephalo **G**raphy
NIRS	**N**ear **IR**nfrared **S**spectroscopy
PCB	**P**rinted **C**ircuit **B**oard
PEC	**P**erfect **E**lectric **C**onductor
PET	**P**osition **E**mission **T**omography
PVC	**P**oly**V**inyl **C**hloride
RF	**R**adio **F**requency
Rx	**R**eceiver
SAR	**S**pecific **A**bsorption **R**ate
S/C	**S**ignal to **C**lutter Ratio
SNR	**S**ignal to **N**oise **R**atio
SPECT	**S**ingle **P**hoton **E**mission **C**omputed **T**omography
SSIM	**S**tructural to **S**imilarity **I**ndex **M**etric
TIA	**T**ransient **I**schemic **A**ttack
Tx	**T**ransmitter
UWB	**U**ltra-**W**ide**B**and
VNA	**V**ector **N**etwork **A**nalyser
WB	**W**ide **B**and

List of Symbols

3-D	Three dimensional
σ	Electrical conductivity
ε_r	Dielectric constant (relative permittivity)
ε_{eff}	Effective dielectric constant
L_{eff}	The effective length
Δ_L	The length extension
L_P	The actual length of patch
W	Width of the microstrip patch
B	Bandwidth
μ	Permeability
ZL	The total characteristic impedance of the microstrip transmission line
TL	Microstrip transmission line
tx_m	Transmitting source
rx_{np}	Receiving positions
V	Volume of interest
F	Frequency
k	Wave number
N_{PT}	Number of measured points
Δ_s	Spatial sampling
Δ_f	Frequency sampling
N_f	Summation truncation value
m	Number of transmitting sources (sampling interval)
np	Number of receiving positions (sampling interval)
A	Matrix
I	Intensity
S, R, C	Matrices

Chapter 1

Introduction

1.1 Research Motivation

Strokes are the leading cause of adult disability in the world and are the number two cause of death worldwide [1]. Stroke is definitely a devastating disease which has great impact on all human neurological conditions. For all global data sources on the stroke, roughly 5.5 million deaths are reported annually. In addition to the high number of deaths from stroke, there is a huge number of disability-adjusted life-years lost which is around 44 million around the world. Stroke is called as a serious illness of aging. Recently, the rapid worldwide spread of the stroke seems quite likely to rise considerably because the world-wide population of over sixty-five years old remains to be increased by about nine million people per annum [2]. The population of people over sixty-five years old is expected to be around eight hundred million people around the world, of whom 67% are estimated to reside in developing countries, mostly in Asia and Latin America [3]. Regarding these significant changes, all over the world, the researchers and scientists study and investigate the observation challenges, risk factors, financial influence, burden of illness and the effective solutions for detection and treatments, during the decades ahead. To be able to completely evaluate the international burden of this disease, fundamental epidemiological data are mandatory for whole areas. Regrettably, fewer than 33 % of all countries in the world are reporting even simple measures for instant death. So those, the majority of available data are received from developed countries [2]. With regards to the expected growth of the aging population, it comes to be more and more vital to create consistent techniques for the investigation of accurately and correctly measuring the burden, mortality and incidence of the stroke, globally.

Comprehensively, the approximate number of people who experienced a first-ever stroke in the year 2005, is sixteen million, with an approximate prevalence of 6.2 million survivors. In the scientific estimation, the approximate increase in the number of people who experienced a first-ever strokes to twenty-three million and deaths of 7.8 million is shown by 2030, which is due

to the lack of clinical and public-health interventions [4]. Roughly, the total number of people who died is fifty-six million in the world, with about fourteen million deaths from vascular disease. The two leading sources of death in the world belong to the mortality from ischemic heart disease with 7.2 million and stroke with 5.5 million people annually. Particularly, 9.7 % of the deaths globally are attributed to stroke [4]. In the developed countries, the prevalence of stroke has been extremely high, also the stroke mortality has shown to be as a top reason of death. For example, in the U.S., stroke has shown to be the number three cause of death by over one hundred forty thousand people who die from stroke annually. Since the epidemiological transition of the illnesses expands rapidly into the developing countries all over the world, the total number of worldwide deaths from stroke is very likely to rise dramatically. In middle-income and low-income countries, the death rate of stroke is very likely to rise a lot more than high-income countries, over the period of two decades, as shown in Figure 1.1 [4].

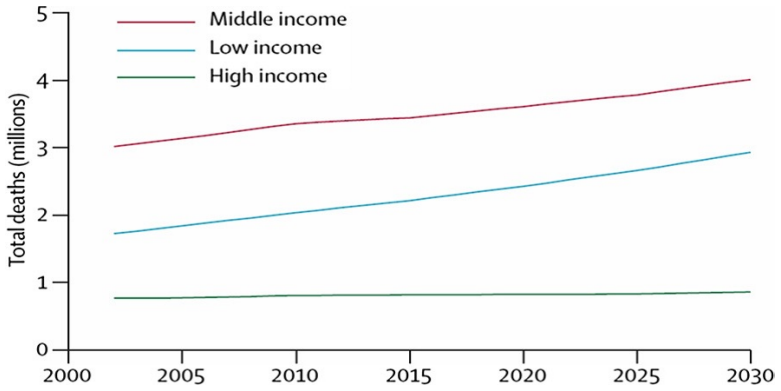

FIGURE 1.1: Predicted increase in the death rate of stroke provided by World Bank income group, considering the years 2002 to 2030 [4].

Severe brain injuries include acquired and traumatic injuries that are caused by external forces (such as falls or accidents) or internal incidences (such as stroke and tumours), respectively. Brain strokes occur when cerebral blood circulation fails as a result of a blocked or burst blood vessel, causing an ischemia or a haemorrhage, respectively. There are common symptoms between the haemorrhagic stroke and the generic medical conditions like fainting, migraine, heart problems and seizures [5]. Therefore, the other health conditions should not be misdiagnosed with haemorrhagic stroke. It is well known that providing the immediate medical attention for a patient with a brain injury is of vital importance to medical professionals. Every second, from the moment of brain injury, millions of brain cells die, leading to irreparable and permanent damage or even death. Thus, if medical staff diagnose haemorrhagic stroke, receiving an appropriate drug treatment within 4.5 hours of the onset symptoms plays a crucial role in saving a patient's life [6]. Hence, a portable diagnosis system is pivotal on the spot for rapid

diagnosis of brain injuries. Initially, a clinical examination using a neurological assessment is performed by a general practitioner (GP) [6]. However, this assessment cannot afford a definite conclusion as many non-vascular conditions can appear as the haemorrhagic stroke symptoms. As such, medical professionals mainly rely on imaging analysis like the computed tomography (CT) scan and magnetic resonance imaging (MRI) in the process of diagnosis. The complexity of stroke diagnosis highlights the vital need of MRI and CT scan systems. They are however, neither fast nor portable (owing to pertinent dimensions of the devices), nor are they usable at rustic medical centres, or carried by first response service which are seen as essential for saving a person experiencing haemorrhagic stroke. Beside this, the highly costly and time-consuming diagnostic processes are major shortcomings of MRI system [7]. Compared to CT and MRI scanners, MWI may potentially provide a portable detection system, and thus, is able to present the initial diagnosis of various emergency life-threatening circumstances such as strokes due to brain injury, whilst patients are still being taken by ambulance to hospital, and save critical therapy time [8]. The underlying purpose and motivation of this work is to showcase the feasibility of utilising MWI techniques for diagnosis of haemorrhagic stroke. The images from the suggested procedure, with the addition of physical and cognitive features enable emergency medical technicians (EMTs) to not only prove the presence of the stroke, but also recognise the location of it and provide the necessary medication promptly on site. The radar-based MWI procedure is presented as a stroke detection technique.

1.2 Research Investigations, Novelty and Challenges

Further to the mentioned advantages of our imaging procedure, there is another novelty that in this thesis I present the results of both simulation and measurements. The technique has been validated through simulations on a three-dimensional (3-D) head model with a target inclusion representing the haemorrhagic stroke. Experimental result on a head phantom containing an inclusion imitating the blood indicates the capability of the algorithm to detect the inclusion inside the head phantom. The main components of MWI in this study are the imaging system design based on Wideband (WB) antennas, the design of brain phantom, signal (Artefact removal methods) processing methods. In this thesis, the following challenges have been addressed.

1.2.1 Microwave Imaging Technique

Microwave technology, applied to imaging systems has been a focus of recent research [9], specifically to detect head diseases such as strokes and intracranial hematomas. Diagnostic MWI exploits the differences in tissues' dielectric properties [9]. It has been demonstrated that brain haemorrhagic stroke changes the dielectric properties of the tissues [10]. Haemorrhagic stroke results in a significant increase in the dielectric properties (up to 20%) with respect to the dielectric properties of white/grey matter [11]. MWI for stroke detection is based on the high differences in electrical properties difference between haemorrhagic stroke and surrounding tissues. The electromagnetic properties of electromagnetic wave interacting with a medium mainly depend on the relative permittivity and conductivity of that medium. A wide range scale of studies [11]-[13] revealed that the content of water in tissues determines their relative permittivity. Tissues with high water content, such as haemorrhage have higher relative permittivity compared to low water tissues such as fat. The relative permittivity of the tissue is related to its electromagnetic energy storability, while the conductivity of the tissue indicates the attenuation of microwave energy when the microwave interacts with it. In this thesis, MWI is proposed as a stroke detection method. Current research on microwave stroke and tumour imaging is divided chiefly into radar techniques and microwave tomography (MWT) [14]. MWT endeavours to reconstruct the dielectric property profile of the head by finding a solution to a relatively nonlinear and ill-posed inverse scattering problem [15],[16]. One of the detrimental points of MWT is the solution instability resulted from the complex mathematical formulations. In contrast, radar imaging entails finding a solution to a simpler problem of discovering the scattering map based on contrast amongst the dielectric properties of human head tissues. Examples of such radar imaging technique have been proposed [17]. Furthermore, the focus of this work is on an approach, approximately similar to radar imaging, which has the objective to localise strong scatterers. In contrast to tomography, our approach does not reconstruct the dielectric properties inside the domain, but it investigates the presence of the main scattering centre.

1.2.2 Wideband Antenna Design and Simulation

Currently, several antennas are designed and fabricated for microwave brain imaging [9],[18],[19]. A difficulty of MWI technology is how to conform more antennas together to coat the restricted region of human tissues [20]. It has been shown that the coupling medium can optimise antenna penetration, however, with great complexity [21]. Moreover, the antenna is required to be immersed in a 90% glycerine-water mixture to achieve broadband operation and couple energy more efficiently into the head [18]. Thus, for lower complexity, in this project, I employ

one transmitting antenna and one receiving antenna (coupled through a vector network analyser (VNA)) which rotate all around the object in order to collect the signals in a multi-bistatic fashion. Another significant aspect of this research is that the antennas are working in free space, so there is no need to use neither metamaterials [18] nor matching mediums [11],[21].

1.2.3 Brain Phantom Design and Experimental Setup

The phantom design for the WB transmission can be simplified and approximated as a multi-layer model, with each phantom layer corresponding to a particular layer of the brain.

1.2.4 Signal Processing

It is the main advantage of Huygens principle (HP), which requires a very simple hardware set-up. HP is a signal processing technique that reconstructs the differences in dielectric properties of the object. Among linear scattering techniques, the HP based technique allows the detection of dielectrics inhomogeneities in the frequency domain [22]. Hitherto, HP has been exploited for several cancer detection applications, notably for breast and skin cancer detection [23],[24]. The aim of this research is not only to provide the results on the efficacy of HP MWI for haemorrhagic stroke detection but also to locate a haemorrhagic stroke in a multi-layered head phantom. Conversely, an important aspect of any imaging system for stroke and cancer detection is the artefact removal algorithm. A large number of such existing algorithms work on the basis of the simplified assumptions regarding the degree of commonality in the artefacts across all channels. A wide spectrum of current artefact removal algorithms, coupled with algorithms altered from ground penetrating radar applications, are provided for comparison with a variety of suitable performance metrics [25]. The methods of artefact removal used in this research were basically derived from the literature of reference [25].

In this thesis, the fabricated WB antennas have been presented using MWI technique on the basis of the HP used on a multi-layered head phantom including an inclusion depicting a haemorrhagic stroke. The simplicity of HP obviates the need for finding a solution to the inverse problems when forward propagating the waves. Also, HP allows capturing the contrast such that different material properties within the region of interest could be differentiated in the final image. Moreover, the rotation subtraction and subtraction of the data of a healthy head model from the data of a head model with haemorrhagic stroke have been employed in pursuing the goal of detecting haemorrhagic stroke. Accordingly, an "Ideal" image would be generated using substraction artefact removal method to prove the concept of the technology. This would mean that the "Ideal" image performed as a reference for the comparison with the resulting image from

using other artefact removal methods. In addition to the subtraction artefact removal method, in this research, four more methods have been introduced and investigated. These methods consist of rotation subtraction, local average subtraction, differential symmetric receiver type, and summed symmetric differential. The subtraction and rotation subtraction artefact removal methods have been used both in simulations and measurements. It has been verified that all artefact removal procedures allow detection. Subsequently, five dedicated image quantification procedures have been implemented in order to assess the detection capability. These estimations comprise area difference, centroid difference, signal-to-noise ratio, structural similarity index metric, and signal-to-clutter ratio. Validation of the techniques through both simulation and experimental measurements have been performed and presented, illustrating the effectiveness of the methods.To the best of my knowledge, such research has not been performed previously.

1.2.5 The Preliminary Study of Brain Stroke Detection

In the presented study, brain stroke detection is considered since a new procedure may provide a fast and portable imaging device which plays an important role in saving the critical therapy time. The human head has a spherical shape, and moreover is composed of different layers. The human head can be considered as layers of skin, skull bone and grey/white matter layers [26]. From electromagnetic theory, the discontinuities of the boundaries cause strong reflections of incident electromagnetic wave [27]. Another significant issue is the ability of microwaves to penetrate into tissue. In stroke detection, the human head has a complicated structure of skull, grey and white matter [26] and might reflect energy. This could be the most important challenge in detection of the stroke. Moreover, different artefact removal techniques have been introduced and investigated in order to find the best method for removing the artefact and detecting the stroke.

1.3 Research Aim

The aim of this research is to develop an MWI technique for brain stroke detection, further goal is to validate the simulation results using designed WB antennas with measurements. Another aim of this research is to provide the results on the efficacy of HP microwave imaging for haemorrhagic stroke detection, and also to locate a haemorrhagic stroke in a multi-layered head phantom.

1.4 Research Objectives

The main objectives in this thesis are as follows:

1. To design and fabricate the WB antennas for brain stroke detection,
2. To design and fabricate a brain phantom for the MWI system,
3. To employ the methods of signal processing for removing the clutter,
4. To employ a signal processing method for distinguishing stroke from healthy tissues and
5. To validate the simulation results and procedure with measurements (one inside the anechoic chamber and then with MWI device).

1.5 Novelty

The novel and significant aspects of the presented work are as follows:

1. Providing a novel procedure using only two antennas for brain stroke detection,
2. Another significant aspect of this research is that the antennas are working in free space,
3. A novel procedure may provide a fast and portable imaging device which is playing an important role in saving the critical therapy time,
4. The technique validates through simulations and measurements,
5. Five methods of signal processing are applied to the collected scattering signals. These five approaches can eliminate the unwanted parts of signals for instance clutter and artefact,
6. Microwave images on the basis of the receiving and transmitting antennas configurations are designed to indicate haemorrhagic stroke position. A haemorrhagic stroke with radius of 10 mm is clearly detected,
7. Five dedicated image quantification metrics have been implemented in order to assess the detection capability,
8. A study of brain stroke detection based on the MWI is carried out. To my best knowledge, research such as this has never been conducted before.

1.6 Thesis Structure

A succinct overview and background of issues with regards to the brain stroke is presented, in Chapter 2. These contain the physiology of the brain strokes, presently employed clinical diagnostic methods and microwave imaging (MWI) for brain stroke detection.

Next in Chapter 3, first the principles and significant parameters of the microstrip antenna with fractal ground plane are analysed and reviewed. Then, the final optimised microstrip antennas and the simulation data are presented. Two microstrip antennas with fractal ground plane which are modified from the original microstrip antenna design are proposed in this section. These two antennas are simulated using Computer Simulation Technology (CST) software and fabricated in-house at London South Bank University (LSBU) with the aim of detecting the brain haemorrhage.

The multi-layered head phantoms with haemorrhagic stroke with two different moulds are proposed, in Chapter 4. These phantoms are used in anechoic chamber and with MWI device for experimental measurements. Two designed and fabricated microstrip antennas are also proposed and employed to measure the head phantom inside the anechoic chamber.

The signal processing methods for the received scattering signals are discussed in Chapter 5. Five artefact removal methods are proposed and applied to remove the clutter and artefact. In this chapter, imaging procedure, HP, and five image quantification methods will also be discussed.

In Chapter 6 (results), the received scattering signals which are obtained from the microstrip patch antennas are employed to produce the microwave images to indicate the location of the haemorrhagic stroke. Then the signal processing techniques are proposed and employed to discriminate between healthy human head tissues and haemorrhagic stroke. At the end, five dedicated image quantification metrics have been implemented to assess the detection capabality.

Finally, the conclusions of the study and suggestions for future work are discussed in Chapter 7.

1.7 Summary

MWI-based brain stroke detection has the capability to be applied for brain stroke diagnosis and to replace presently applied clinical methods, due largely to its efficiency, non-ionising radiation, small dimensions and low cost. MWI may provide a fast and portable imaging device (owing to pertinent dimensions of the device) which is usable at rustic medical centres, or

carried by first response service. The study of MWI-based stroke detection should concentrate on the design and fabrication of the antennas and human head phantom and signal processing.

Chapter 2

Background

2.1 Introduction

This chapter considers the background of brain stroke regarding the physiology of brain stoke, human head, and current brain stroke detection methods. This section provides essential and critical background information for the following chapters, specifically for the brain stroke phantom design, which will be presented in Chapter 4. The structure of this chapter is organised as following. First, the physiology of the brain is presented; followed by a discussion of recent brain stroke detection methods. In the end, the final section focuses on the introduction of MWI for brain stroke detection, which will be followed in Chapter 5.

2.2 Physiology of Human Head

2.2.1 Anatomy of Human Head

The anatomy of the brain [28] and its surrounding tissues are illustrated in Figure 2.1 (a) [29]. In general, the human head is composed of skin, skull, and brain tissue [28].

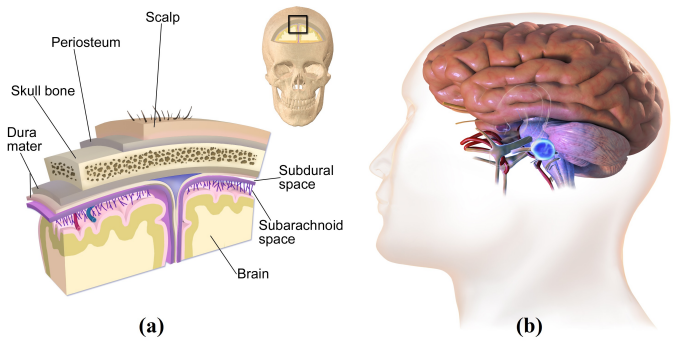

FIGURE 2.1: (a) Layers covering the Brain, (b) Anatomy of the human head [30].

The main function of the skull is to protect the human brain.

2.2.2 Brain Stroke and Stroke Burden Worldwide

Brain stroke is one of the greatest ordinary cardiovascular disorder (disease), with an annual incidence of around fifteen million cases all over the world, causing permanent injuries or even death. Throughout the previous years, the age-standardised stroke morbidity and mortality rates have shown a continual decrease, in many developed countries. This means that during recent years, younger patients are suffering from stroke. Over a period of twenty years, since 1990 to 2010, the total incidence rate of haemorrhagic and ischemic stroke rose to 47 and 37 %, respectively. Whilst, the number of deaths from both haemorrhagic and ischemic stroke rose to 20 % during the same period of time. The total number of deaths from stroke is expected to be increased by 12 million deaths by 2030 [31]. Figure 2.2 shows the global burden of strokes with hotspots of high stroke incidence, and mortality in East and Southeast Asia, Central Africa, Oceania, and Eastern Europe. The global burden of strokes highlights the great significance of medical diagnosis and appropriate treatments.

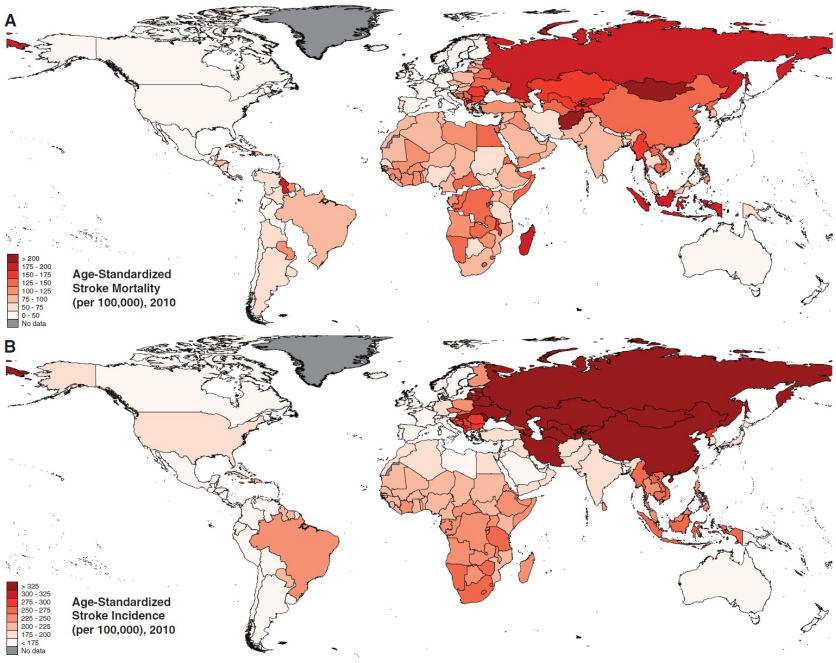

FIGURE 2.2: Age-standardised stroke mortality, and (b) incidence per 100,000 [31].

Severe brain injuries include acquired and traumatic injuries that are caused by external forces (such as falls or accidents) or internal incidences (such as stroke and tumours).

TABLE 2.1: Stroke mortality by age: share of stroke in all deaths for age 30-44, 45-59, and 60-64 (%) [31].

Country	**Age Group**	**Share of stroke in all deaths (%)**
United States	30-44	2.1
	45-59	4.1
	60-64	3.6
England/Wales	30-44	4.0
	45-59	5.5
	60-64	6.8
Ireland	30-44	5.1
	45-59	5.6
Finland	30-44	5.0
	45-59	6.2
	60-64	6.5
Sweden	30-44	2.4
	45-59	4.7
Norway	30-44	3.0
	45-59	4.2
	60-64	5.5
Denmark	30-44	3.1
	45-59	4.1
	60-64	4.6
France	30-44	3.1
	45-59	4.5
Switzerland	30-44	2.2
	45-59	3.5
	60-64	4.3
Italy	30-44	5.5
	45-59	7.1
	60-64	7.8
Spain	45-59	6.8
Portugal	30-44	4.2
	45-59	11.4

The brain strokes occur when cerebral blood circulation fails as a result of a blocked or burst blood vessel, causing an ischemia or a haemorrhage, respectively. To be exact, a stroke is characterised as a neurological shortfall affected by an infarction of the central nervous system in a specified region of a vascular disruption (intracerebral haemorrhage) or a focal ischemic injury on the basis of symptoms continuing longer than 24 hours till death [32]. A stroke can take place in any portion of the brain. It causes cell death in the nervous system and leads to post-stroke disabilities. Early symptoms and signs of a stroke comprise the lack of ability to feel and move one side of the body, difficulties of speaking and/or understanding, and failing eyesight on one side of the body [33]. These injuries are contingent upon the localisation and size of the lesion. Generally, strokes are the most important reason for long-term disability [34] and are the number one source of motor handicap in Europe [35]. Ordinary and persistent disabilities include lower and upper extremity deficits, incontinence, cognitive dysfunction, and speech difficulties [36],[37].

Roughly 80 % of patients who suffered from strokes, experience a unilateral motor deficit, which limits engagement and functionality in their life, obliging them to request for aid and support in the several everyday activities of living. There are common symptoms between the transient ischemic attack (TIA), strokes and generic medical conditions like fainting, migraine, heart problems and seizures [5]. To provide appropriate medical treatment for patients, the other health conditions should not be misdiagnosed with stroke. It is well known that providing immediate medical attention for a patient with a brain injury is of vital importance. Every second, from the moment of brain injury, millions of brain cells die, leading to irreparable and permanent damage or even death. Thus, if medical staff diagnose stroke, and perform an appropriate drug treatment within a few hours of the symptoms onset, they play a crucial role in saving a patient's life [38]. Based on medical history, diagnostic tests and clinical examination, including brain imaging, a subclassification of stroke is feasible. Hence, a portable diagnosis system is pivotal on the spot for rapid diagnosis of brain injuries.

The word "stroke" was used as a replacement on behalf of apoplectic seizure as early as 1599 and is a quite correct translation of the Greek term [39]. Strokes can be mainly classified as haemorrhagic stroke and ischemic stroke. In 1658, in his "Apoplexia", Johann Jacob Wepfer (1620-1695) recognised the source of haemorrhagic stroke while he recommended that people, who had died of apoplexy, had bleeding in their brains. In addition, he found the main arteries supplying the brain, the vertebral and carotid arteries, and found the source of ischemic stroke while he recommended that apoplexy could be initiated by a blockage of those vessels [39]-[41]. Stroke can be due to haemorrhage or ischemia (shortage of glucose and oxygen supply) produced by embolism or thrombosis [42].

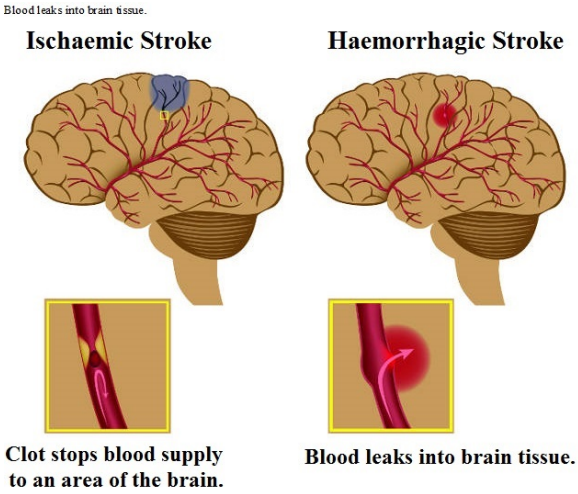

FIGURE 2.3: Stroke types [43].

The discrimination between haemorrhagic stroke and ischemic stroke is chiefly based on the content of water within the strokes. An increase in water content in stroke shows the deterioration of cells, and this enhances the values of the dielectric constant and conductivity of the strokes [10],[11]. Moreover, morphology [11] is another important characteristic in discriminating between haemorrhagic stroke and ischemic stroke in terms of their size and shape, as shown in Figure 2.3. These two main criteria are regularly employed in medical diagnosis, such as when using magnetic resonance imaging (MRI) and ultra-sonic imaging.

Many issues have regularly been identified to be correlated with an increased risk of stroke, and provided the burden of stroke, prevention is a most important public health concern [44]. The correlation of these issues with stroke is endorsed by a huge body of epidemiological and experimental scientific work. Risk factors for stroke might be categorised as nonmodifiable and modifiable. Fortunately, the record of nonmodifiable risk factors is shorter than the record of modifiable factors. Nonmodifiable risk factors for stroke are comprised of male gender, hereditary syndromes, advanced age and ethnicity. Modifiable risk factors for stroke are comprised of dyslipidaemia, hypertension, obesity, physical inactivity, diabetes mellitus, alcohol abuse, smoking, and atrial fibrillation, among others [45].

2.2.3 Electrical Properties

Electromagnetic based MWI for stroke detection is on the basis of the electrical properties of strokes and nearby tissues. The electrical properties of the tissues comprise two major factors

known as conductivity and relative permittivity. The electromagnetic properties of the electromagnetic wave interacting with a medium rely on its conductivity and relative permittivity. Numerous researches [13],[26],[46] have revealed that the content of water in a tissue determines its relative permittivity. Tissues with high water content for instance haemorrhagic stroke and tumour have greater relative permittivity than those with low water content for example white / grey matter.

A tissue's relative permittivity is correlated with the storability of electromagnetic energy in the tissue whilst the tissue's conductivity shows the attenuation of microwave energy when the microwave interacts with it. The differences in electromagnetic properties between healthy and unhealthy (i.e. stroke, tumour) tissues is employed to detect the strokes on the basis of MWI. The contrast for the conductivity (σ) and relative permittivity (ε_r) of healthy and haemorrhagic stroke tissues across 1 GHz -4 GHz range have been shown in Figure 2.4 [47].

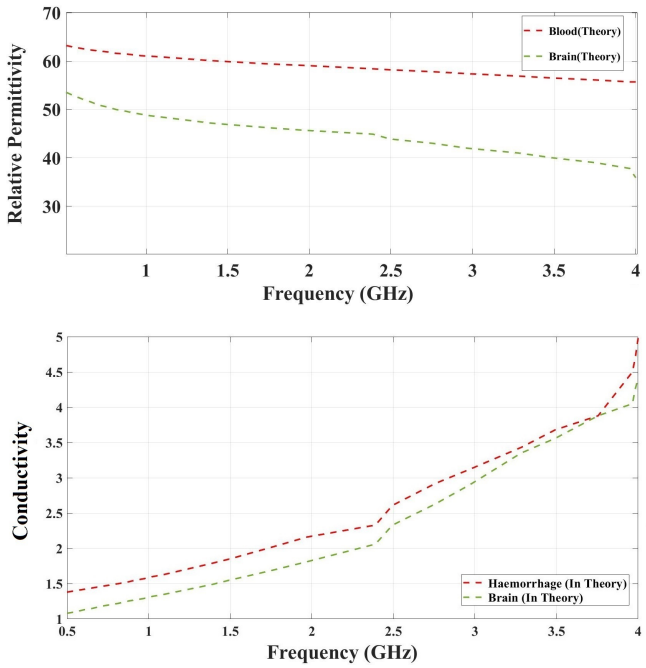

FIGURE 2.4: Dielectric properties (the relative permittivity (ε_r) and conductivity (σ) of the average human brain tissues including the average of grey and white matter, and blood clot (representing haemorrhagic stroke), in theory [47].

2.3 Currently Used Clinical Diagnostic Methods

Receiving a proper medication treatment for a stroke patient within 4.5 hours of the onset symptoms has a vital and essential role in saving a patient's life. Initially, a clinical examination using a neurological assessment is performed by a GP [48]. However, this assessment cannot afford a definite conclusion as many non-vascular conditions can appear as the haemorrhagic stroke symptoms. As such, medical professionals mainly rely on imaging analysis like ultrasound, the CT scan and MRI in the process of diagnosis. Ultrasound is one of the medical imaging techniques which are currently applicable to the patients. But in the case of head imaging, this procedure has difficulties in passing through skull. As ultrasound has low penetration depth and also in the case of brain imaging the most important thing is to have higher penetration depth in order to penetrate through the skull (head bone) which is the hardest part of human head [8]. Therefore, it is definitely not an option for head imaging and detection of the brain strokes or brain tumours.

The most regularly applied clinical diagnostic techniques for brain stroke detection are X-rays and MRI. The complexity of stroke diagnosis highlights the vital need of MRI and CT scan systems. They are however, neither fast nor portable (owing to pertinent dimensions of the devices), nor are they usable at rustic medical centres, or carried by first response service (FRS) which are seen as essential for saving a person experiencing haemorrhagic stroke. There is a variety of different imaging techniques which enable the study of the brain. This section presents a brief overview of the different imaging methods. The principles of these methods are summarised as follows.

2.3.1 Computed Tomography Scan and X-rays

Brain imaging techniques are classified according to the captured information in two main categories: the functional and structural imaging. CT and MRI are the most popular and effective structural imaging techniques which are also known as anatomical imaging techniques. These two neuroimaging modalities concentrate on visualising the different tissues and structures of the brain. CT is creating detailed images of a patient's body by employing X-ray technology which is on the basis of the absorption of X-rays beams as they pass through the different tissues of the human body. CT images are created through employing a string of X-ray beams which revolve around the patient's head. The CT image is shown in Figure 2.5. Each beam produces a 2D image at a specific angle that is employed to construct a 3D volume by tomographic reconstruction. CT scans are well contrasted and provide high-resolution images. However, using

ionising radiation is the major disadvantage of this method.

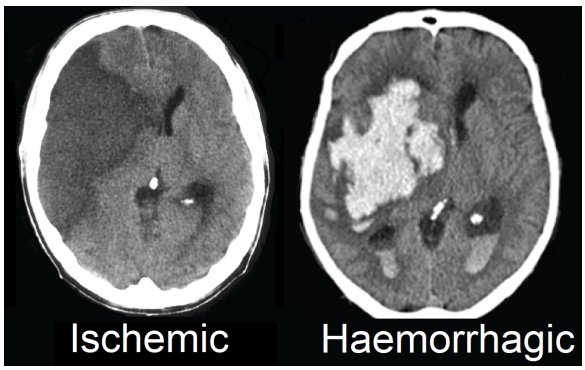

FIGURE 2.5: Computed tomography (CT) scan images: (left) ischemic stroke and (right) haemorrhagic stroke [49].

X-rays are another technique of medical imaging which is not able to provide detailed information on the organs of body. The created images demonstrate different parts of human body in different shades of white and black due to the fact that different tissues can absorb various quantities of radiation. With no doubt X-rays with ionising property will not be the first suggestion in the case of brain imaging. However, X-rays are easy to use and inexpensive [50].

2.3.2 Magnetic Resonance Imaging

One of the common imaging procedures for medical applications is MRI. This procedure is on the basis of employing magnets to make an extremely strong magnetic-field used to create a pathological image [50]. To be exact, MRI is a type of scan that depends on the magnetic property of the hydrogen nuclei present in significant amount in the body. MRI is used for brain investigations because of its non-ionising property and high tissue contrast and details. It is a great technique used in brain studies and brain imaging, specifically for detecting brain strokes and tumours. Since MRI is a non-ionising and non-invasive imaging method which provides images with high tissue contrast and details. The great sensitivity of MRI gives us the high-resolution images of soft tissues. For imaging, the patient lies on an examination table, then radio waves and strong magnetic fields are used by an MRI scanner, to construct detailed images of human body. The image of human head with stroke is shown in Figure 2.6. It is however, neither fast (due to the time-consuming diagnosis process) nor portable (owing to pertinent dimensions of the devices), and is not utilisable at small medical centres.

During the past decade, different methods have been employed for instance Diffusion Tensor Imaging (DTI). This method allows reconstruction of the white matter tracts connecting various portions of the neural systems in human brain by measuring the anisotropic diffusion of water

within the human body tissues. Modality such as perfusion MRI which is a method employing the measurement of the relative cerebral blood volume by using a contrast agent, may make the additional information available for study of brain tumours and specifically the diagnosis [48].

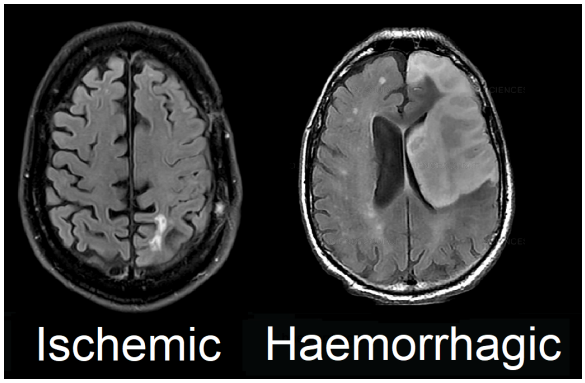

FIGURE 2.6: Magnetic Resonance Imaging (MRI) images: (left) ischemic stroke and (right) haemorrhagic stroke [49].

2.3.3 Other Imaging Modalities

A specific aim of the functional imaging is to study the brain's function on the basis of the physiological changes brought about by the activity of the human brain. Magnetoencephalography (MEG) and Electroencephalography (EEG) are methods which suggest approach of measuring the activity of the human brain. The magnetic flux changes are measured by MEG with employing several sensors placed on the human head. EEG distinguishes the electrical impulses within the brain tissues owing to the neuronal activity through electrodes positioned closed to the human head. These techniques are prevalent because of their considerable ease, very high temporal resolution and non-aggressive procedures. A great disadvantage of these techniques is that a precise determination of the spatial origin of the detected signal is difficult.

Single Photon Emission Computed Tomography (SPECT) and Position Emission Tomography (PET) are using the nuclear imaging procedures which measure the changes within the cerebral blood flow and the metabolism of the tissue. A biological molecule is shown through a radioactive isotope, then it is injected with the bloodstream and amassed in the regions where the molecule has affinity. The radioactive tracer is able to be designed particularly for targeting the determined tissues or procedures of an illness and this is a great advantage of SPECT and PET. However, these procedures are not only invasive and potentially detrimental as a consequence of employing the radioactive tracers; but also, they are costly and difficult especially in producing the isotopes. Currently, a combination of PET and CT technologies in one device is

to combine the metabolic data which has been collected from the PET scans with the anatomical data recovered from the CT scans.

As previously mentioned in this section, the positive and negative points of diagnostic technique for brain stroke detection may be categorised according to portability, accuracy, safety, and cost. The limitations of the mentioned techniques encouraged scientists to design and create a low-cost, more efficient, non-ionising and less harmful diagnosis technique for brain stroke detection. Compared to CT and MRI scanners, MWI can provide a portable detection system, and allow initial diagnosis of various emergency life-threatening circumstances such as strokes due to brain injury, whilst patients are still being taken by ambulance to a hospital, saving critical time [8]. For this purpose, researchers are highly motivated to develop a diagnosis method by employing MWI. MWI is introduced in the next section. Figure 2.7 shows current different medical imaging techniques of human head.

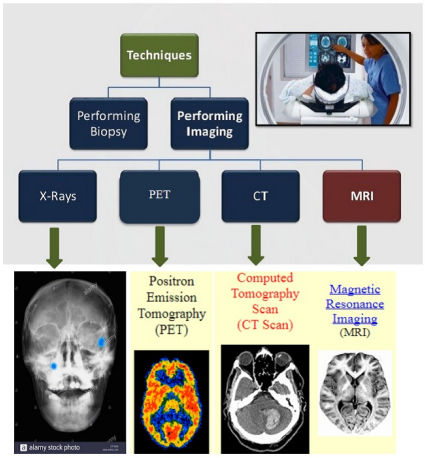

FIGURE 2.7: Various methods of Brain imaging [50].

2.4 MWI for Brain Stroke Detection

MWI may be applied for detection and monitoring of a variety of diseases due to the fact that there is a significant contrast at microwave frequencies between the dielectric properties of healthy tissues and tissues with lesions [8]. Specifically, MWI for brain abnormalities has motivated many research groups, due to the several positive points such as portability, low-cost and non-ionising radiation. Several forms of MWI techniques, which may be categorised as active or passive MWI, have been recently suggested. Active MWI is dependent on the marked differences between the electromagnetic properties of the healthy tissues and those of

the stroke tissue. Two common methods of active MWI are radar-based imaging [51] and MWT [52]. Passive MWI is another form of MWI technique which is dependent on the difference between high temperature of the stroke or cancerous tissue and healthy tissues while the brain is illuminated with microwave radiation [53]. To collect and transmit the signals, a radiometer is mostly applied. Then the collected signals are employed to map the distribution of temperature for diagnosis purposes. However, detecting the radiated power by stroke is not easy and it is a major challenge to the medical staff of using passive MWI. The radiometer should have enough capability to show a high sensitivity to the small changes in radiated power. Also, the performance of the radiometer can simply be disrupted by the environmental heat source. Finally, active MWI is of most interest in the current project and used in this thesis. This form of MWI technique is explained more in the next section.

2.4.1 Active MWI (Microwave Tomography)

Recently, various system prototypes using microwaves for brain stroke diagnostics have been suggested. Currently, two major active MWI methods, namely radar based MWI and MWT are employed in the stroke's detection studies and investigations. The MWT pursues the electrical profile reconstruction inside the human body by solving inverse scattering problems [52]. This approach requires solving nonlinear functions that triggers the problems of image reconstruction and signal processing. One example is the Stroke finder, developed at Chalmers University [54], which detects and classifies different types of intracranial bleedings (ischemic or haemorrhagic). Stroke Finder comprises three components:

- An antenna system which strongly resembles a helmet and is placed on the patient's head, as shown in the Figure 2.8
- A microwave unit
- A computer used for controlling the paraphernalia and collecting the signals and data in order to proceed to signal processing

To be exact, the device is comprised of 12 Tx/Rx triangular patch antennas fixed on a helmet made of plastic. The plastic balloons filled with water, between the head and the patch antennas, are used to act as matching medium. The clinical and medical experiments are proceeding in Gothenburg at Sahlgrenska University Hospital with the purpose of verifying the mentioned system.

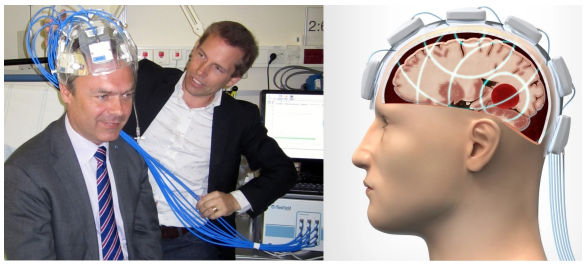

(a) **(b)**

FIGURE 2.8: A helmet-shaped antenna system is placed on the (a) human head and (b) human head model [55].

Another system, the BRIM G2 has been developed at EMTensor [56] for brain imaging.

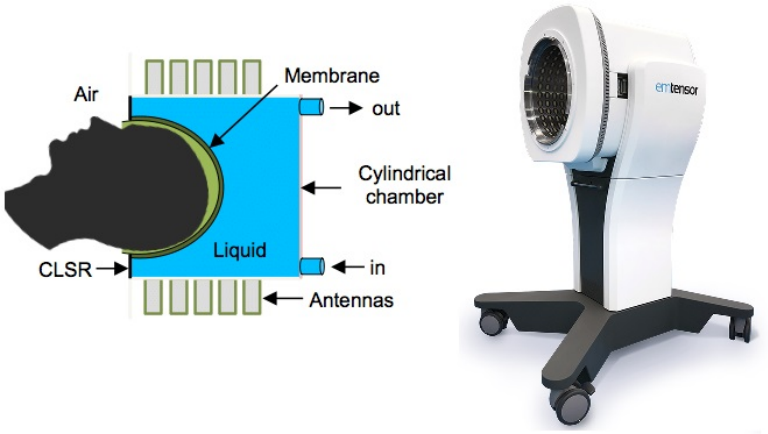

FIGURE 2.9: The microwave imaging system prototype developed by EMTensor GmbH [57].

This system is comprised of 177 rectangular ceramic-loaded waveguide antennas fixed on a hemi-spherical stainless-steel chamber. The antennas are spaced evenly at eight rings, with different heights. Moreover, these rectangular antennas are operating at 1 GHz. The matching medium used in this system is a glycerine-water mixture.

2.4.2 Active MWI (Radar-Based MWI)

The radar-based imaging technique is based on ground penetrating radar and was first offered and used for detecting breast cancer. It concentrates on the recognition of substances like haemorrhagic or ischemic strokes with created images on the basis of the high dielectric difference between the healthy tissues near the stroke and a haemorrhagic or ischemic stroke. Radar-based MWI method with aim of concentrating on the detection of an inclusion/object (stroke) location,

provides images by employing back-scattering signals. In comparison with MWT, radar-based MWI emphasises on imaging the stroke rather than the whole human head or brain. Hence, a signal processing method which is employing the radar-based MWI, can be relatively simpler than the one which is using MWT. Moreover, radar-based MWI exploit a Wideband (WB) Pulse that is comprised of low to high frequency band. While high frequencies can confirm the adequate resolution of the subsequent images, low frequencies can confirm the adequate depth of penetration. Therefore, both low and high frequencies allow the brain abnormalities detection, specifically low frequencies are suitable for the brain strokes detection. Radar-based MWI systems are mainly categorised into mono-static radar [58] and multi-static radar systems [51].

- **Multi-static radar system**

  In this method, a pulse, which is created by a frequency sweep, is radiated inside the specific part of human body employing a transmitting antenna, and the scattered signals which are collected from one or more receiving antenna(s) located on the human body, for instance on the head or breast. Researchers at University of Bristol developed a hemispherical antenna array on the basis of multi-static radar system [51]. The mentioned array antenna is designed using sixteen cavity backed aperture stacked patch antennas which are linked to the electro-mechanical switches network with coaxial cables. The electro-mechanical switches network has made it possible to select every antennas pair of the array antenna and link these pair of antennas to VNA with 120 measured transmission coefficients (S21) collected for post-processing. Then, the measured S21 are time-shifted to add consistently with the aim of reducing the clutter and enhancing the object (e.g. the tumour or the stroke) response. To generate microwave images containing the highlighted stroke, the post-processed data mentioned above are applied.

- **Mono-static radar system**

  Tissue Sensing Adaptive Radar (TSAR) has been offered as a technique of radar-based MWI for early tumour detection of the human breast. TSAR has been fabricated on the basis of the mono-static radar system [58], as shown in Figure 2.11. This technique senses whole tissues in the volume of adapts and involvement. TSAR also has been suggested and fabricated for detecting the brain tumour [59].

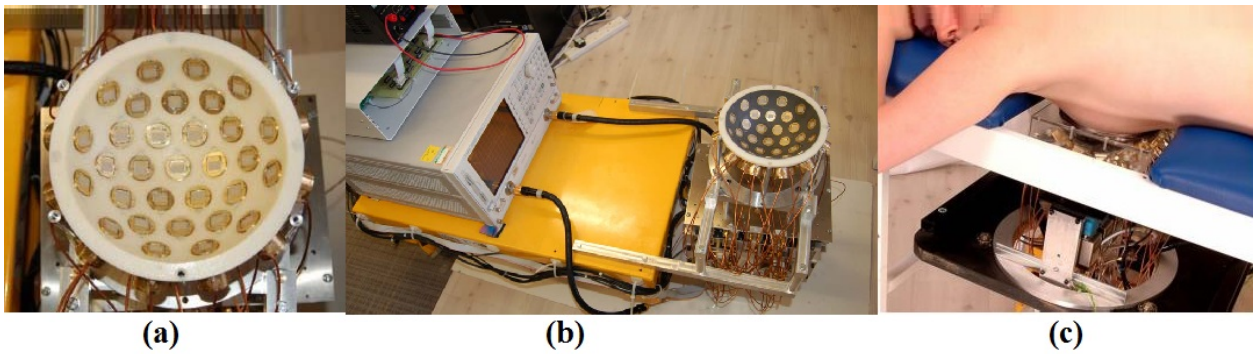

FIGURE 2.10: (a) The multi-static radar system designed and fabricated at the University of Bristol and (b) the clinical setup used for detecting the breast cancer [51].

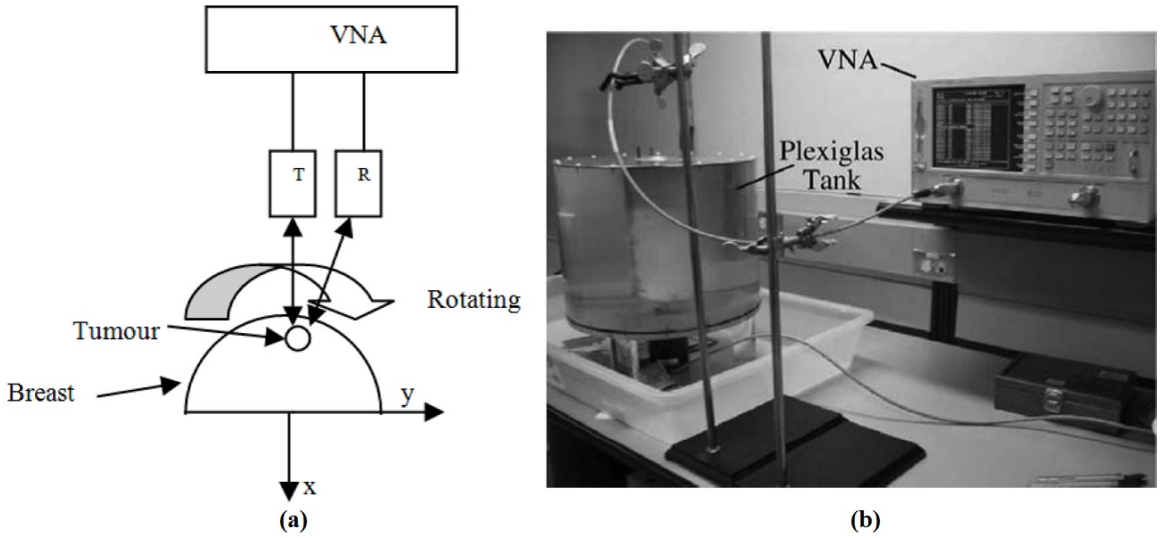

FIGURE 2.11: (a) The prototype setup, and (b) The experimental setup of the mono-static radar-based MWI system for detecting the breast cancer [58].

Mono-static radar system employs two antennas positioned on both sides of the breast, with the movement applied to rotate and scan the breast. The space between transmitting and receiving antennas is considered to reach the maximum sensitivity. A VNA is linked to the mentioned antennas, and the measured S21 are recorded when they change the position to every new observation position. Subsequently, the measured S21 are post-processed in order to generate microwave images with emphasising the object (e.g. the tumour or the stroke). The other existed mono-static radar prototype system, which is recently designed and fabricated at Queensland university, is used for imaging intracranial haematomas [60]. This system is comprised of a ring of 16 tapered and corrugated slot

antennas, which operate from 1 to 4 GHz. The antennas are in air, without the use of a matching medium. The stroke imaging only relies on the monostatic data (i.e., the reflection coefficient at each antenna).

- **Antenna design for radar-based brain stroke detection**

  The prototype of the mono-static radar-based system can be compared with the multi-static radar-based system based on their structure and the complexity, the resolution of the achieved images, and signal processing. One of the disadvantages of multi-static radar-based MWI is that, it employs an antenna array with the switch network controller. Also, the array antenna is comprised of over 10 antennas for collecting a large number of S21 to achieve high resolution in the images. Another disadvantage belongs to the antenna geometrical sizes which should be as small as possible for being able to maximise the quantity of the antennas applied for the array. This becomes a reason for enhancing the operating frequency and minimising the electromagnetic penetration depth inside the human body [20]. Moreover, a difficulty of MWI technology is how to conform more antennas together to coat the restricted region of human tissues as discussed in [20].
  In reference [21], it has been shown that the coupling medium can optimise antenna penetration, however, with great complexity. Moreover, in reference [18] the antenna is required to be immersed in a 90% glycerine-water mixture to achieve broadband operation and couple energy more efficiently into the head. In reference [18], King's College London develop an antenna array for brain imaging with the dimensions of 30 mm for height, 24 mm for width, and 4.88 mm for depth. The dimensions of the substrate, patch, partial ground, and transmission line are shown in Figure 2.12.

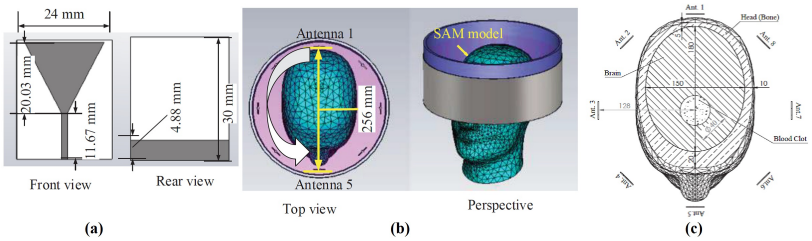

FIGURE 2.12: (a) Antenna structures, (b) array structures simulated using CST studio, and (c) the cross section of the model at the centre plane of the antenna array which represents the brain lesion, and the blood clot [18].

In reference [51], a wide slot antenna with the dimensions of 13 mm for height, 14 mm for width, and 1.25 mm for depth has been designed and fabricated at the University of

Bristol. As shown in Fig 2.13 (a), a cavity has been applied at the back of the proposed antenna for decreasing mutual coupling and absorbing the back scattered radiation. From the other point of view, mono-static radar-based MWI employs only one or two antenna(s) to scan a part of human body with mechanical movement, as shown in Figure 2.13 (b) [61]. Therefore, the antenna's design only focuses on the gain, fidelity, and bandwidth of the antenna. In Addition, when the quantity of antenna reduces, the required signal post-processing complexity and the mutual coupling will be decreased. Other important issue of this procedure is the resolutions of the obtained image.

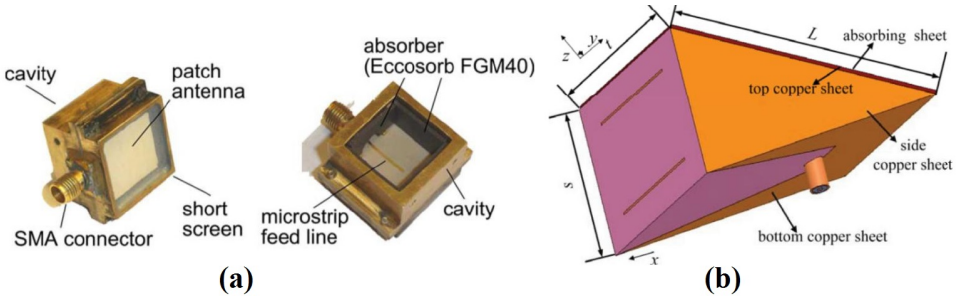

FIGURE 2.13: (a) The designed and fabricated antennas which has been employed multi-static imaging systems by Bristol University [56], and (b) the designed antenna which has been employed for mono-static imaging system [61].

2.5 Conclusion

Chapter 2 presented the background of brain stroke and the existing brain stroke diagnosis procedures and systems. In this chapter, the anatomy of the brain based on the classification of the strokes was explained. A stroke can be cast into two major categories, haemorrhagic and ischemic stroke. A haemorrhagic stroke occurs when a blood vessel bursts inside the brain; the blood accumulates and compresses the surrounding brain tissue. An ischemic stroke occurs when cerebral blood circulation fails as a result of a blocked vessel. The course of treatment for ischemic and haemorrhagic strokes is different. An initial examination done by a physician is typically clinical using a neurological exam. This however is not always conclusive as many non-vascular conditions can simulate stroke symptoms. As such, medical professionals rely on the CT scan and the MRI. They are however, neither fast nor portable (owing to pertinent dimensions of the devices) and are not utilisable at small medical centres. Compared to CT and MRI scanners, MWI can provide a portable detection system, and allow initial diagnosis of various emergency life-threatening circumstances such as strokes due to brain injury, whilst patients are still being taken by ambulance to a hospital, saving critical time [8]. MWI for

stroke detection has not only the advantage of being cost-effective, but also using non-ionising radiation, which has drawn the attention of several academic and research teams.

The discrimination of stroke and healthy tissues is chiefly on the basis of their electrical properties. It has been demonstrated that tissue malignancies, blood supply, hypoxia, acute ischemia, and chronic infarction [62] change tissue dielectric properties. A high dielectric contrast between tissues with high water content (e.g., muscle tissue) and low water content (e.g., bone) presents an additional complication for MWT imaging. MWI techniques may be mainly categorised as active and passive microwave imaging. Passive MWI is one form of MWI technique which is dependent on the difference between high temperature of the stroke or cancerous tissue and healthy tissues while the brain is illuminated with microwave radiation. However, detecting the radiated power by stroke is not easy and it is a major challenge to the medical staff using passive MWI. This problem is created due to the fact that detecting the power reflected by the object (e.g. the tumour or the stroke) is not easy. Active MWI is another form of MWI technique which is dependent on the marked differences between the electromagnetic properties of the healthy tissues and those of the stroke tissue. Two common methods of active MWI are radar-based imaging and MWT. Radar-based MWI only concentrates on the detection of the object (e.g. the tumour or the stroke). A great advantage of radar-based MWI technique is that the signal processing for radar-based MWI is significantly simpler than that for MWT. Two main categories of radar-based MWI prototype system consist of mono-static and multi-static radar systems. In this chapter, the antenna design, principles and prototypes of these two categories of radar-based MWI techniques have been reviewed, explained, and analysed in full detail. In this thesis, mono-static radar-based MWI technique is used.

Chapter 3

Antenna Design and Simulation for Head Imaging

3.1 Introduction

The radar-based MWI technique aims to determine the position and location of the stroke by generating images applying back scattering signals received from the stroke inside the human head. The radar-based MWI prototype procedures may be categorised as two different systems of mono-static and multi-static radar systems. The mono-static radar-based MWI system [58] employs a pair of antennas or only one antenna in order to scan the human head using mechanical movement. On the other hand, the multi-static radar-based MWI system [63], employs an antenna array with a switch network controller. This antenna array typically is comprised of more than two antennas to select and collect a huge number of the transmission coefficients' data in order to get images with high resolution. The design of the antenna is a crucial part of the radar-based MWI system. Conventional techniques of designing antenna considered that the antenna should be in free-space. It has been considered for the design of a radar-based MWI antenna that the antenna should be positioned on the human head and near to the brain in the near field. The produced pulse by antenna is emitted inside the phantom tissue. The mentioned phantom tissue and the real body tissue that surrounds the brain stroke are alike in many ways, such as electrical properties and dimensions. Multi-static radar-based MWI system employs an antenna array, therefore the geometrical feature and size of the antenna should be as small as possible with the purpose of maximising the quantity of antennas employed in the array, so that, it will be effective in increasing the operation frequency.

Other important factor of designing antenna for detection of brain stroke is mutual coupling. Mutual coupling indicates that an antenna is able to produce an induced current caused by the current flowing through nearby antennas. This current can change the radiation pattern, the

scattering parameters, and the antenna impedance. These changes would make the properties of the antenna unstable and unpredictable. Therefore, the biggest challenge of designing antenna for multi-static radar-based MWI procedure could be the mutual coupling and the antenna dimensions [64]. The current issue has been resolved for the mono-static MWI procedure, as this system applies a pair of antennas or only one antenna. This is the reason why the designing of the antennas just concentrates on its bandwidth, fidelity, and gain. Moreover, the decreased quantity of the antennas reduces not only the signal post-processing complexity but also the mutual coupling.

For a very long period of time, WB technology has been commonly utilised in the fields of wireless communication and radar. These techniques apply short pulses, typically a few nanoseconds [65]. Employing WB technology offers numerous improvements, for instance low power transmission, high reliability and capacity [65]. Also, a crucial additional use of WB is radar-based MWI for medical applications. Employing WB technology gives the final images high resolution because of the high bandwidth spectrum. Typically, the WB operating frequency includes both high and low frequency components. The low operating frequency content offers the possibility for having the high penetration capability to detect the brain stroke whilst the high operating frequency content lacks the penetration capability. Therefore, the mentioned distinctive aspect may be particularly appropriate to the needs of the radar-based MWI brain stroke detection. Moreover, the brain stroke is frequently buried at shallow layers. So, the essential depth penetration can be in the form of only some centimetres. However, at issue here is the human head skull (bone) which should be carefully considered in our evaluations due to its hardness. The corresponding operating frequency may typically be considered to set between 1-2 GHz. This band has demonstrated to be ideal and optimal to do brain imaging [8]; in addition, it is obviously emphasised that WB can enhance performance in lesion detection [66]. Hence, a WB antenna which works efficiently across that band is a vital factor on the success of the suggested system.

WB antenna can also be fitted with the mono-static radar system in order to reduce the complexity of designing the imaging system. The theory of microstrip patch antenna for designing a highly appropriate antenna to detect the brain stroke is completely described. In this chapter, both the design of the antenna and the simulation procedure will be explained and presented. The aim of this section is to offer a coherent account of the design, analysis, and theory of the microstrip patch antenna, as well as to explain the medical application of this antenna by using imaging the human head in the simulation part. The chapter then explains the geometry of the microstrip patch antenna, feeding technique, and material considerations, in overall terms.

3.2 Theory of the Microstrip Patch Antenna

The planar type antenna is making the majority of WB antenna prototypes. One of the most successful choices of the radar-based MWI for brain stroke detection, is the planar topology, due to the rather minor dimensions of the planar type antenna. Therefore, several studies have selected this sort of antenna owing to the positive points of easy integration and ordinary construction. Construction of the microstrip patch antennas are on the basis of the printed circuit board (PCB), which puts forward the suggestion for high accuracy and very low cost. Moreover, another advantage of the microstrip patch antenna is that this kind of antenna may be simply integrated into the PCB board through the MWI system on the basis of the photoetching technique and technology, which raises the integration of the system and leads to decreased prices and costs. Some of the nonplanar antennas for instance the log period antenna and the horn antenna employ resistive loading for expanding the bandwidth of their antennas, which causes low efficiency. Most of the planar antennas for example the bowtie antenna, stacked patch antenna, and the monopole antenna, excluding the horn antenna, are employed for the multi-static radar-based MWI systems by reason of their physical large sizes [67].

In this thesis, the mono-static radar-based MWI procedure is applied to the prototype for the suggested imaging system. As it has been discussed in this section, the mono-static radar-based MWI procedure employs one antenna or a maximum of two antennas to mechanically scan the human head in order to detect the brain stroke. Therefore, the sizes of the antenna cannot be a major factor. In this research, the triangular microstrip patch antenna with fractal ground plane has been used as the prototype for the brain stroke detection.

3.2.1 A Basic Explanation and Background of the Microstrip Patch Antenna

Microstrip patch antenna is a sort of planar antenna that has been studied and used widely during the previous years. Recently this kind of antenna has become more and more popular, and employed in several applications of wireless communication systems. Not only is it employed in the military area, but also in the commercial area. A fundamental concept of the microstrip patch antenna is derived from employing printed circuit technology or both the circuit, transmission lines components and the electronic system radiating factors. Initially, the idea of using this antenna was first offered by Deschamps in the 1950's [68], although it has not been used until the 1970's. Since the 1970's, researchers draw inspiration from Deschamps's idea in developing and using microstrip patch antenna. There are quite a lot of studies leading to several

publications, books, articles, and handbooks on the idea of applying and developing microstrip patch antenna [68]. The positive aspects of the microstrip patch antenna are as below [68]:

1. Being planar; microstrip patch antenna can be created appropriately for the specific shaped surfaces,
2. Being easy to feed,
3. Low cost,
4. Light weight,
5. Being easy to design, analyse and fabricate,
6. Ability to manufacture via the printed circuit tools,
7. Being able to be united by the elements of circuit,
8. Having the small physical dimensions (The microstrip patch antenna has a small size, although the measured electrical size in wavelength is not small.), and
9. Low radar cross section.

The mentioned positive aspects of the microstrip patch antenna make them mostly appropriate for commercial mobile, wireless communication systems, aircraft, and spacecraft. Due to the positive aspects listed above, this type of antenna has also been applied and developed for different medical applications, such as monitoring and medical imaging for diagnosis purposes. This antenna includes a single-layer design that contains normally four portions of the feeding part, ground plane, patch, and the substrate. There are several various substrates which are employed in the designing of microstrip patch antenna, their dielectric constants are typically between a range of 2.2 to 12 ($2.2 \leq \varepsilon_r \leq 12$). The most desirable substrates for good performance are the ones which have more thickness and the dielectric constant is in the lower end of the above mentioned range, as these substrates offer a greater bandwidth, an increased efficiency, loosely bound fields with the aim of radiation into space. Substrates with the lower thicknesses and greater dielectric constants are used in the form of microwave circuitry, as they need firmly bound fields minimise unsuitable coupling and radiation, that may cause minor element dimensions [68].

3.2.2 Patch of the Microstrip Antenna

The microstrip patch antennas have been technically used to design and fabricate several procedures and devices due to being easy for construction and analysis, cost-effective, low weight, and their ease of feed and attractive radiation features [68]. The microstrip patch antenna has one single-layer that comprises normally four portions: ground plane, substrate, feeding, and microstrip patch part [67]. Basically, a simple microstrip patch antenna's structure has been presented in Figure 3.1. This antenna is comprised of metallisation's area, over the ground plane, which is supported by a small thickness of a dielectric substrate and fed with the ground in a suitable position. In principle, the shape of microstrip patch antenna can be designed based on funcation, e.g. cut corner to have circular polarisation, matching feeding network. Some common shapes of microstrip patch antennas consisted of the circular, the rectangular and triangular forms, as shown in Figure 3.1 (b). From which, rectangular and triangular forms are mostly used.

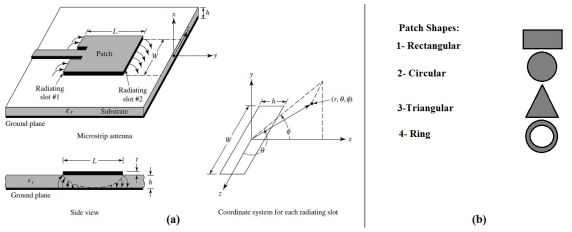

FIGURE 3.1: (a) A simple microstrip patch antenna's structure, (b) Four different common shapes of microstrip patch.

The triangular and rectangular patches are definitely the most commonly employed shape and configuration of the microstrip patch antenna. Here, the proposed triangular microstrip patch antenna is derived from an initial design of a rectangular microstrip patch antenna, and the process and the reason will be discussed more in this chapter. The microstrip patch antennas, as also has been shown in Figure 3.1 (a) contains low thickness metallic patch (called strip, $t \ll \lambda_0$, λ_0 is the wavelength of the free-space) which is located on the ground plane (a minor fraction of a full-wave length, $h \ll \lambda_0$ where h is typically equal to $0.003\lambda_0 \leq h \leq 0.05\lambda_0$). The pattern maximum of the microstrip patch antenna is designed to be normal to the patch (broadside radiator). It can be accomplished by appropriately selecting the field configuration of the excitation under the microstrip patch. As shown in Figure 3.1 (a), the ground plane and the microstrip patch (or strip) have been detached from each other via a dielectric sheet (by the name of substrate).

3.2.3 Feeding Approaches

Another important part of designing a microstrip patch antenna is the feeding approaches. There are several formations and approaches of microstrip patch antennas' feeding. These approaches (methods of feeding) can be classified into 2 categories non-contacting and contacting. In the non-contacting scheme, electromagnetic field coupling is done to transfer power between the microstrip line and the radiating patch. Whilst in the contacting approach, the RF power is fed directly to the radiating patch using a connecting element such as a microstrip line. In the non-contacting scheme, electromagnetic field coupling is done to transfer power between the microstrip line and the radiating patch. The four most common microstrip patch antennas' feeding approaches include the microstrip line, coaxial probe (both contacting schemes), aperture coupling and proximity coupling (both non-contacting schemes).These microstrip patch antennas' feeding approaches are as shown in Figure 3.2.

Microstrip line feed:

In microstrip line feed approach, a conducting strip has been linked in a straight line to the edge of the antennas' patch as shown In Figure 3.2 (a). The conducting strip is smaller in width in comparison to the patch and this sort of feeding approach benefit from this fact that the feed can be etched on the same substrate to offer a planar structure. The aim of the inset cut in the patch is to match the impedance of the feed line to the patch without the need for any additional matching element. This is achieved by controlling the inset position. Henceforth this feeding approach is with low complexity (easy method), meanwhile it offers simplicity in construction and ease of modelling in addition to impedance matching. It is important to be mentioned, as the thickness of the dielectric substrate being used, increases, surface waves and spurious feed radiation also increases, which hampers the bandwidth of the antenna [67].

Coaxial feed:

One of the common feeding approach is coaxial feed or probe feed. Coaxial-line feed which has been presented in Figure 3.2 (b), where the internal coax conductor is connected to the radiation patch whilst the external coax conductor is linked to the ground plane, are likewise widely applied. The coaxial probe feed can easily be designed, fabricated and matched. The coaxial probe feed has low spurious radiation. Though, it similarly has narrow bandwidth and it is much more hard to design and model, particularly with using the thick substrates ($h > 0.02\lambda_0$) [67].

Aperture coupled feed:

The aperture coupling feed, which has been shown in Figure 3.2 (c), is the most arduous methods of all four to construct. In addition to that, the aperture coupling feed has narrow bandwidth. The aperture coupling feed consists of two substrates detached through a ground plane. There is a microstrip line feed on the lowest side of the bottom substrate, that the energy is coupled to the patch over a slot on the ground plane isolating these two substrates. Characteristically, a high dielectric material has been employed and applied in the lowest substrate. The ground plane in the middle of the substrates correspondingly separates the feed of the radiating element. The main difficulty of this feeding method is the challenge to construct it, because of multiple layers, which also rises the thickness of the antenna. The current feeding arrangement also offers narrow bandwidth [67].

Proximity coupled feed:

This feeding method is also known as the electromagnetic coupling arrangement. In the proximity coupled feed, which has been shown in Figure 3.2 (d), two dielectric substrates have been employed such that the feed line is between the two substrates and the radiating patch is on top of the upper substrate. The chief benefit of this feeding method belongs to the ability of it in eliminating spurious feed radiation and providing high bandwidth [67]. The main difficulty of this feeding method is the challenge to construct Microstrip Line Patch owing to the two dielectric layers which require appropriate alignment. Furthermore, there is a rise in the overall thickness of the antenna [67].

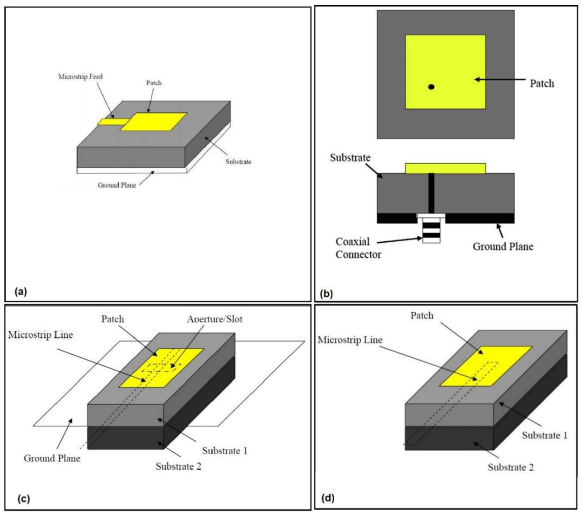

FIGURE 3.2: Four different common feeding approaches for microstrip patch antenna [67].

To summarise this section, of four feeding approaches which have been described here, the proximity coupling feed can offer the highest bandwidth. It can easily be designed and modelled, and also has short spurious radiation. But the fabrication of the proximity coupling feed has greater difficulties than other four methods [67],[69]. Here, in this thesis the microstrip line feed method has been selected, since this method not only has the advantage of easier fabrication and design, but also has the advantage of being simply matched.

3.2.4 Methods of Analysis

The other significant part of designing microstrip patch antenna which should be carefully evaluated and considered during calculation and designing stage is the approaches of analysis. There are several various approaches of analysis applied to designing the microstrip patch antennas. The most common approaches are as below:

1. The transmission-line method
2. Cavity method
3. Full wave (which include primarily integral equations/Moment Method) method

The easiest of all methods belongs to the transmission-line method which provides good physical insight, however, the transmission-line method has fewer accuracy and more difficulties for model coupling. In comparison with the transmission-line method, the cavity method has more accuracy but also it is much more complex. Though, the cavity method also provides good physical insight and has again much more difficulties in modelling the coupling, even though this method has been employed effectively. Finally, the full-wave methods have more accuracy and they are very adaptable. But the full-wave methods have much more complexity and typically provide fewer physical insights. In this thesis, the transmission-line model has been chosen, as it was the easiest of all. We will discuss more about it in the next section.

3.2.5 Transmission-line Model (Fringing Effects, Effective Length, Resonant Frequency, and Effective Width)

As it has been discussed in the earlier section, the transmission-line model is the easiest method in compared to all methods. This model has some physical insight which needs to be discussed. The fields at the edges of the microstrip patch undergo fringing due to the fact that the microstrip patch's size and dimensions are finite along the width and length. In Figure 3.3 (a) and (b), the fringing for the two radiating microstrip antenna slots is shown alongside the length and also

the similar one applies to the width. The fringing quantity can be a function of the substrate's height and the microstrip patch's dimensions. Fringing can be calculated by a function of the patch's length ratio (*L*) to the substrate's height (*h*) and the substrate's dielectric constant or relative permittivity (ε_r), for E-plane (xy-plane). *L/h*$\gg$1 should be considered in calculations of designing the microstrip Patch antenna, since with this consideration not only fringing is decreased, but also the resonant frequency of the antenna is affected. Also, the similar definition applies to the width.

A microstrip line-feed has been shown in Figure 3.3 (a), and in Figure 3.3 (b), electric-field lines are illustrated. For explaining effective dielectric constant, first consider the microstrip line's centre conductor with its principal and basic height and dimensions over the ground plane which is embedded in a dielectric, as illustrated in Figure 3.3 (c). The effective dielectric constant can be described as a constant dielectric material which is also called the dielectric constant. Therefore, the line of Figure 3.3 (c) has the same electrical features as the real line of Figure 3.3 (a), chiefly propagation constant. For the line with the air over the substrate, the values of the effective dielectric constant (ε_{eff}) is between one and the dielectric constant (ε_r), 1< ε_{eff} < ε_r. In the most applications that the relative permittivity is much larger than unity ($\varepsilon_r \gg 1$), the value of the effective dielectric constant (ε_{eff}) will be same as the one for the actual substrate's dielectric constant (ε_r). ε_{eff} is similarly a function of frequency.

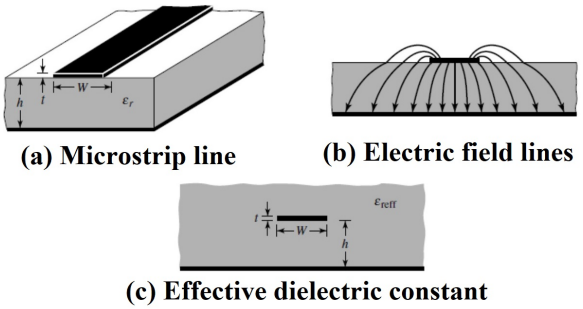

FIGURE 3.3: Microstrip line and electric field lines of the microstrip line, and the geometry of the effective dielectric constant [69].

With an increase in operation frequency, the majority of electric-field lines focus on the substrate. As a result of this fact, the microstrip line acts further similar to the one dielectric homogeneous-line (to be exact, just similar to the substrate), also the value of the effective dielectric constant is close to the one of substrate's dielectric constant. For the intermediate frequency range, the value of the effective dielectric constant starts evenly increasing and at last will be close to the value of the substrate's dielectric constant. The first effective dielectric

constant's values are given by reference [67], and mentioned as the static values.

$$\frac{W_p}{h} > 1, \varepsilon_{eff} = \frac{\varepsilon_r + 1}{2} + \frac{\varepsilon_r - 1}{2}[1 + 12\frac{h}{W_p}]^{1/2} \tag{3.1}$$

where W_p is the width of the patch, and *h* represents the height of the patch. Other important issues for the transmission-line model are the calculation of the values for effective Length, resonant frequency, and effective width. Due to the fringing effects, specifically the microstrip patch seems bigger than the physical sizes and dimensions of the microstrip patch. For the main E-plane (xy-plane), it is proved that in the situation which the patch's dimensions have been lengthened on each end to the distance of $\triangle L$, that $\triangle L$ is a function of the width to height ratio (W_p/h) and the effective dielectric constant (ε_{eff}), as calculated in Equation (3.5). It should be noted that to calculate the antennas' parameters in this chapter the Equations (from Equation (3.2) to Equation (3.13)) are given by reference [70].

$$\triangle L = 0.412h\frac{(\varepsilon_{eff} + 0.3)(\frac{W_p}{h} + 0.264)}{(\varepsilon_{eff} - 0.264)(\frac{W_p}{h} + 0.8)} \tag{3.2}$$

As the patch's length has been lengthened (on each side) to the distance of $\triangle L$, the patch's effective length is, as given in Equation (3.3).

$$L_{eff} = L + 2\triangle L \tag{3.3}$$

The resonant frequency of the microstrip patch antenna can be a function of the microstrip patch antenna's length. Typically it can be calculated by Equation (3.4).

$$f_r = \frac{1}{2L\sqrt{\varepsilon}_r\sqrt{\mu_0\varepsilon_0}} = \frac{1}{2L\sqrt{\varepsilon}_r} \tag{3.4}$$

As Equation (3.4) cannot be accounted for the fringing, this equation should be improved to contain the edge effects and must be calculated applying Equation (3.5).

$$f_r = \frac{1}{2L_{eff}\sqrt{\varepsilon}_{eff}\sqrt{\mu_0\varepsilon_0}} = \frac{1}{2(L + 2\triangle L)\sqrt{\varepsilon}_{eff}\sqrt{\mu_0\varepsilon_0}} = q\frac{1}{2L\sqrt{\varepsilon}_r\sqrt{\mu_0\varepsilon_0}} = q\frac{\vartheta_0}{2L\sqrt{\varepsilon}_r} \tag{3.5}$$

In the above Equation ϑ_0 is the light speed in free space. q factor has been considered and mentioned as the fringe factor. It represents the losses associated with the antenna. It should be

noted that if the height of the substrate rises, there will be a rise in the fringing, as well. This results in a greater parting of the radiating edges followed by the lower resonant frequencies.

3.3 Design of the Microstrip Patch Antenna for Brain Stroke Detection

3.3.1 Design Process

The triangular microstrip patch antenna is initially designed and derived from a rectangular microstrip patch antenna using CST Microwave Studio. As the simulation has been done in CST microwave studio, the triangular microstrip patch antenna cannot be designed at a single stage. The triangular shape of antenna should be derived from a rectangular shape. Hence, the rectangular microstrip patch antenna has been designed in CST microwave studio and then modified to a triangular microstrip patch antenna. The reason why the triangular microstrip patch has been chosen (instead of rectangular microstrip patch antenna) is to enhance the bandwidth of the antenna. Given the fact that the rectangular microstrip patch antenna draws a sharp distinction in the performance, in the form of bandwidth from the antenna gain [71].

In this part of thesis, different single and array microstrip antennas have been designed, in order to have an operating frequency between 1 and 2 GHz for successful detection of stroke, and also to propose an effective technique for increasing the bandwidth of the antenna and subsequently a better head image through designing a triangular patch antenna using fractal ground plain. In this chapter,we are going to discuss all useful corresponding designs of the antenna which have been tried in this project, and at the end, the best design of the antenna will be represented and discussed. In this part, first the designing of the rectangular microstrip patch antenna will be completely explained. Then, a designed rectangular multi patch antenna (also named as the array antennas) will be discussed and the calculation will be fully explained. After that, the design of the triangular microstrip patch antenna derived from the initial design of the rectangular microstrip patch has been explained and represented. Next, a designed triangular multi patch antenna (array antennas) has been proposed. Afterward, a designed triangular microstrip patch antenna with a Path-square shaped fractal ground plane has been proposed.

Finally, the proposed selected design will be used by applying the design of the fractal ground plain to that proposed designed antenna. The calculation and designing of the above mentioned antennas are provided in the next sections. This chapter investigates the improvement of the microstrip patch antenna. The improvement emphasises the bandwidth of the antenna in a specific range of frequency (1 to 2 GHz). The first goal in antenna design is to enhance

the bandwidth of the antenna, which can offer the ability to have a deeper penetration. A highly appropriate technique of increasing the bandwidth of the antenna is to enhance the antenna's dimension, which offers a lower operating band of frequency. But the mentioned technique can cause some difficulties in scanning the human head owing to the great size and dimension of the antenna. Hence one major goal of the design is to enhance the bandwidth of the antenna whilst preserving the antenna dimensions.

3.3.2 The First Stage: Designing Rectangular Microstrip Patch Antenna (Geometrical Parameters of the Microstrip Patch Antenna)

Before starting the calculation process for designing the antenna, an appropriate material for the substrate should be selected. Considering the dielectric substrate, FR-4 is a rank designation allocated to glass reinforced epoxy laminate rods, PCB, tubes, and sheets. The dielectric constant of FR-4 is equal to 4.4, and it is a compound material of woven fiberglass tissue and an epoxy resin binder which is resistant to flame. This material is widely applied as an electrical insulator possessing substantial mechanical strength. Figure 3.4 demonstrates a rectangular patch antenna using microstrip line feed approach which starts from one side of rectangular patch [70].

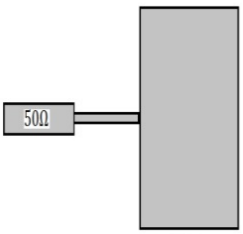

FIGURE 3.4: Rectangular microstrip patch antenna (feed from side) [70].

With regards to the effect of antenna dimensions length (*L*), width (*W*) and substrate parameters relative dielectric constant, substrate thickness (*h*) on the radiation parameters of bandwidth and beam-width. There are several calculation steps before starting to design the antenna. The design procedure is as follows:

- **Step 1**: In this step we should specify ε_r, f_r (in Hz), and *h*. Then both the width of the microstrip patch and the actual length of patch should be determined in the next steps. The width of the microstrip patch (W_P) can be calculated as [70]:

$$W_P = \frac{1}{2f_r\sqrt{\mu_0\varepsilon_0}}\sqrt{\frac{2}{\varepsilon_r+1}} = \frac{\vartheta_0}{2f_r}\sqrt{\frac{2}{\varepsilon_r+1}} \tag{3.6}$$

ϑ_0 is the free space velocity of the light.

$$W_p = \frac{c}{2f_0\sqrt{\frac{\varepsilon_r+1}{2}}} \tag{3.7}$$

f_0= 2.3 GHz, ε_r = 4.4, *c*=3.00 $\times$ 10^8 m/s
Then we got the width of the microstrip patch *W* equal to 39.5 mm.

- **Step 2**: The effective dielectric constant (ε_{eff}) can be calculated using Equation (3.1) [70]:

$$\varepsilon_{eff} = \frac{\varepsilon_r+1}{2} + \frac{\varepsilon_r-1}{2}[1+12\frac{h}{w}]^{1/2}$$

ε_r = 4.4, *h*=1.2 mm, *W*= 39.5 mm.

Then we got the effective dielectric constant equal to 2.3.

- **Step 3**: The effective length (L_{eff}) can be calculated as:

$$L_{eff} = \frac{c}{2f_0\sqrt{\varepsilon}_{eff}} \tag{3.8}$$

f_0= 2.3 GHz, ε_r = 4.4, c=3.00 $\times$ 10^8 m/s

Then we got the effective length equal to 32.9 mm.

- **Step 4**:The length extension ($\triangle$L) can be calculated using Equation (3.2):

$$\triangle L = 0.412h\frac{(\varepsilon_{eff}+0.3)(\frac{W_p}{h}+0.264)}{(\varepsilon_{eff}-0.264)(\frac{W_p}{h}+0.8)}$$

ε_{eff}=2.3, *h*=1.2 mm, *W*= 39.5 mm. Then we got the length extension equal to 0.62.

- **Step 5**: The actual length of patch (L_P) can be calculated using Equation (3.3):

$$L_p = L_{eff} - 2\triangle L$$
$$\triangle L = 0.62, L_{eff} = 32.9 \text{ mm}$$

- **Step 6**: The total characteristic impedance of the microstrip transmission line can be calculated as:

$$ZL = \sqrt{Z1 \times Z2} \tag{3.9}$$

$Z1$=the probe impedance=50Ω
$Z2$=the total input impedance of the rectangular patch antenna= 317.9778Ω
Then we got the total characteristic impedance of the microstrip transmission line (*ZL*) equal to 126.0908Ω.

- **Step 7**: The Length of the microstrip transmission line (*TL*) can be calculated as:

$$TL = \frac{\lambda}{4} = \frac{\lambda_0}{4\sqrt{\varepsilon_r}} \tag{3.10}$$

With:

$$\lambda_0 = \frac{c}{f_0} = 100 \text{ mm/sec} \tag{3.11}$$

f_0= 2.3 GHz, ε_r = 4.4, *c*=3.00 $\times$ 10^8 m/s. Then, we got the length of the microstrip *TL* equal to 16.8 mm.

- **Step 8**: The directivity is describing a parameter which is applied for measuring the maximum direction of radiation. The parameter is depicted as the ratio of the measured antenna's maximum radiation intensity to the radiation which a reference antenna has shown with the equal quantity of power. To be exact, the directivity of the reference antenna is given by reference [70]. The Directive Gain of the antenna can be calculated as:

$$G = e_r D \tag{3.12}$$

Then we got the Directive Gain of the antenna equal to 3.5066.
where D represents directivity and equals 2.2 $\times$ 10^{17} and e_r related to antenna efficiency factor and equals 1.6 $\times$ 10^{-17}.

So that, the computed values of W_P, L_P and *TL* are equal to 39.5 mm, 31.5 mm and 16.8 mm respectively. The overall dimension of the substrate and ground plane are $G_W \times G_L \times h_0$.

The length and width of the rectangular patch are L_p and W_p, as shown in Figure 3.5 (a). A plain ground plane is designed and used in this step, as shown in Figure 3.5 (b). In Figure 3.5 (c), the thickness of the substrate, patch and the ground is shown as *h*, *h1*, and *h0*, respectively. It should be noticed that FR-4 is the material of the substrate which is used here. The scatter parameters are typically applied to clearly define the energy which has been reflected [72]. Assume that we have a black box with two ports, port one and port two, that port one is the input port of the energy and port two is the output port. The S11 is describing the energy which has been reflected from the port one (the port one-reflected energy) whilst S21 demonstrates the energy which has been transferred from the port one to the port two. Both S21 and S11 are identified, namely the forward transmission coefficient and the reflection coefficient, correspondingly.

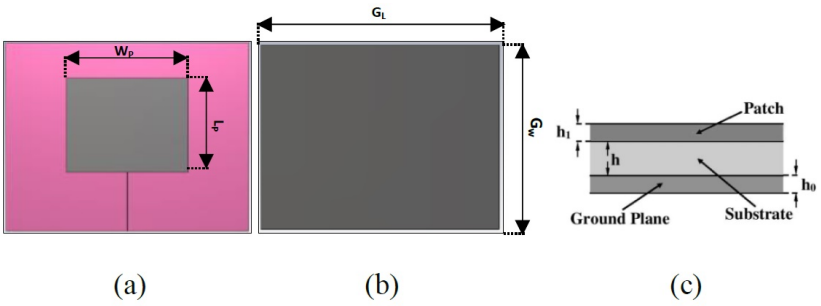

FIGURE 3.5: (a) Geometries of the designed rectangular microstrip patch antenna, (b) geometries of the plain ground plane, and (c) different thicknesses of the different layers of the antenna.

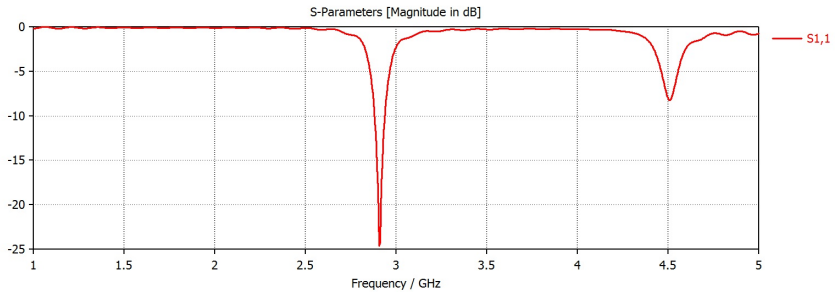

FIGURE 3.6: The return loss vs frequency S-parameter plot for the rectangular microstrip patch antenna.

S11 is the input port voltage reflection coefficient and S21 is the parameter representing the complex transfer function from the transmitting antenna to the receiving antenna. As it has been shown in Figure 3.6, the simulation shows a response at the exact frequency of 2.9 GHz through the return loss of -24.60 dB. It should be noticed that the negative value of the return loss displays the fact that the designed antenna had not many losses whilst transmitting the

signals. Also the bandwidth of the antenna could be calculated in the Figure 3.6 and using the following Equation [70]:

$$\text{Bandwidth} = \frac{f_2 - f_1}{\sqrt{f_1 f_2}} \times 100\% \tag{3.13}$$

Then we got the bandwidth of the rectangular microstrip antenna with plain ground plane equal to 1.57 % in -10 dB.

3.3.3 The Second Stage: Designing Rectangular Multi Patch Antenna (Array Antenna)

In this stage, in order to obtain more enhancements in bandwidth of the rectangular microstrip antenna and also to set the corresponding operating frequency between 1-2 GHz (as this band has demonstrated to be ideal and optimal to do brain imaging [8]), a multi patch rectangular microstrip antenna [72] which is also called an array antenna has been designed by modifying the initial design to a fourfold increase in the number of the rectangular microstrip patch antenna, as shown in Figure 3.7.

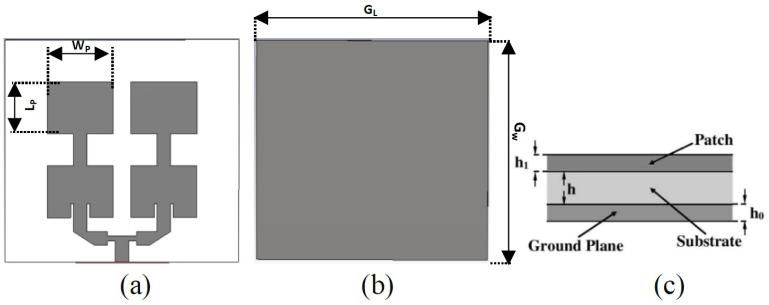

FIGURE 3.7: (a) Geometries of the designed rectangular microstrip array antenna, (b) geometries of the plain ground plane, and (c) different thicknesses of the different layers of the antenna.

Hence, the computed values of W_P, and L_P are equal to 11.86 mm and 9.31 mm, respectively. The overall dimensions of the substrate and ground plane are $G_W \times G_L \times h_0$ and equal to 39.72 mm, 41.86 mm and 0.01 mm, respectively. The length and width of the patch of the rectangular array antenna are L_P and W_P, as shown in Figure 3.7 (a). A plain ground plane is designed and used in this step, as shown in Figure 3.7 (b). In Figure 3.7 (c), the thickness

of the substrate, patch and the ground plane is shown as *h*, *h1*, and *h0*, which are equal to 0.79 mm, 0.01 mm, and 0.01 mm respectively. The return loss vs frequency S-parameter plot for the rectangular microstrip array antenna has been presented in Figure 3.8. It should be mentioned that although the bandwidth was not small, this antenna is ineffective for brain imaging, as the antenna is operating between 10 to 11 GHz (as shown in Figure 3.8). The ideal and optimal band of frequency is between 1 to 2 GHz for brain imaging [8].

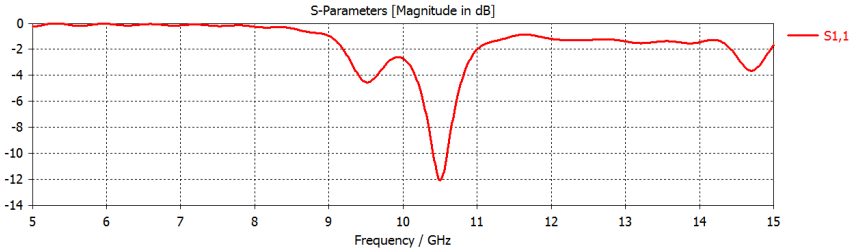

FIGURE 3.8: The return loss vs frequency S-parameter plot for the rectangular microstrip array antenna.

3.3.4 The Third Stage: Designing Triangular Microstrip Patch Antenna

As it has been explained before, in order to obtain enhancement in bandwidth (to increase the bandwith of the antenna) an isosceles triangular patch antenna (as shown in Figure 3.9) is designed by modifying the initial rectangular patch antenna, shown in Figure 3.5. Here, the goal is not only to increase the bandwidth the antenna, also to set the corresponding operating frequency between 1-2 GHz. The Geometries of the designed triangular microstrip patch antenna and its plain ground plane are shown in Figure 3.9 (a), (b), and also the thickness of each layer including patch, substrate, and the ground plane are shown in Figure 3.9 (c).

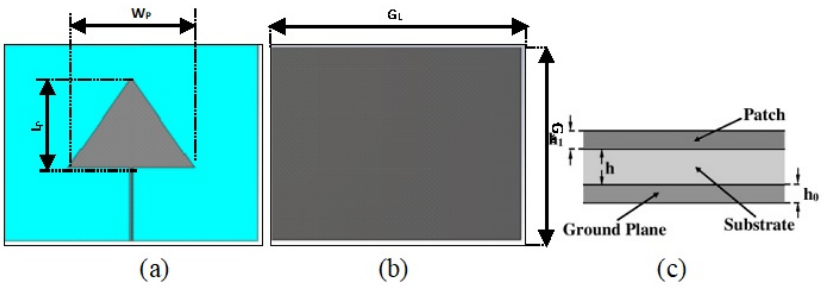

FIGURE 3.9: (a) Geometries of the designed triangular microstrip patch antenna, (b) Geometries of the plain ground plane, and (c) different thicknesses of the different layers of the antenna.

All the dimensions are exactly equal to the initial design of the antenna, the rectangular microstrip patch antenna. Therefore, the computed values of W_P, L_P and *TL* are equal to 39.5 mm, 31.5 mm and 16.8 mm respectively. The overall dimension of the substrate and ground plane are $G_W \times G_L \times h_0$. The length and width of the triangular patch are L_p and W_p, as shown in Figure 3.9 (a). The proposed design has an isosceles triangle patch with two equal sides of 37.18 mm . A same plain ground plane to the ground plane of the triangular microstrip patch antenna (as given in Figure 3.5 (b)) is designed and used in this step, as shown in Figure 3.9 (b). In this part, to design a triangular microstrip patch antenna, the substrate material of FR-4 and the thickness of 1.3 mm have been used.

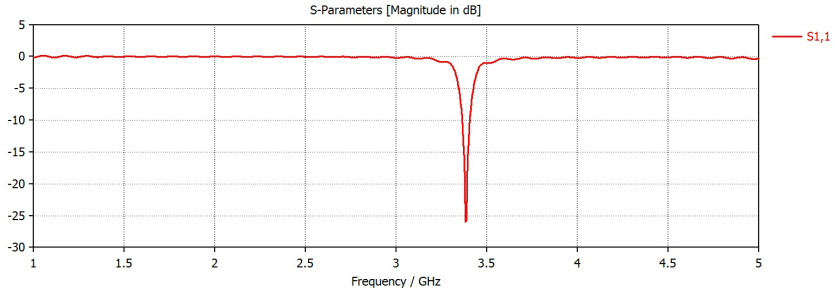

FIGURE 3.10: The return loss vs frequency S-parameter plot for the triangular microstrip patch antenna with plain ground plane.

As it has been shown in Figure 3.6, the simulation shows a response at the exact frequency of 3.38 GHz through the return loss of -25.93 dB. It should be noticed that the negative value of the return loss displays the fact that the designed antenna had not many losses whilst transmitting the signals. The bandwidth of the antenna could be calculated by using Figure 3.10 and Equation (3.13). We got the bandwidth of the triangular microstrip antenna with plain ground plane equal to 2.09 % in -10 dB. To improve the performance and enhance the bandwidth of the microstrip antenna, and also to set the corresponding operating frequency between 1-2 GHz, we decide to use fractal ground plane method in our designs.

3.3.5 The Fourth Stage: Designing Triangular Multi Patch Antenna (Antenna Array)

In this stage, with the aim of getting enhancement in bandwidth of the triangular microstrip antenna and setting the corresponding operating frequency between 1-2 GHz, a multi patch triangular microstrip antenna [73] which is also called an array antenna has been designed by modifying the initial design to a fourfold increase in the number of the triangular microstrip patch antenna, as shown in Figure 3.11.

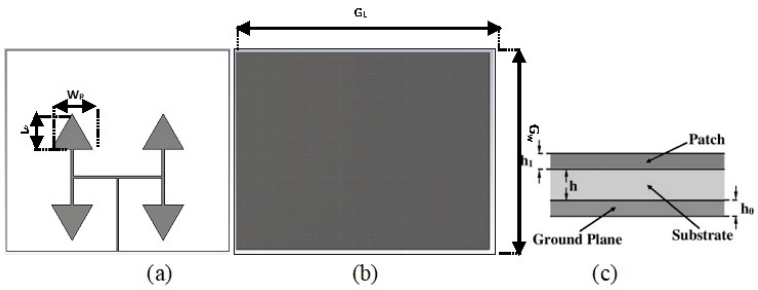

FIGURE 3.11: (a) Geometries of the designed triangular microstrip array antenna, (b) Geometries of the plain ground plane, and (c) different thicknesses of the different layers of the antenna.

Hence, the computed values of *Wp*, and *Lp* are equal to 28 mm and 24.27 mm, respectively. The overall dimensions of the substrate and ground plane are $G_W \times G_L \times h_0$ and equal to 137.52 mm, 153 mm and 0.01 mm, respectively. The length and width of the patch of the triangular array antenna are *Lp* and *Wp*, as shown in Figure 3.11 (a). A plain ground plane is designed and used in this step, as shown in Figure 3.11 (b). In Figure 3.11 (c), the thickness of the substrate, patch and the ground plane is shown as *h*, *h1*, and *h0*, which are equal to 1.6 mm, 0.01 mm, and 0.01 mm, respectively. Here, the calculated bandwidth of this design have not been mentioned and considered, since it was small and ineffective, as shown in Figure 3.12.

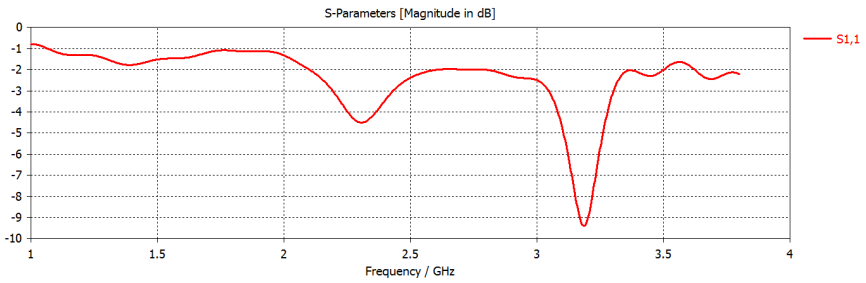

FIGURE 3.12: The return loss vs frequency S-parameter plot for the triangular microstrip array antenna with plain ground plane.

3.3.6 The Fractal Ground Plane

The structure of the fractal ground plane has been applied recently to improve the performance and characteristics of current common microstrip patch antenna. Through the previous decade, with adding the fractal method to the theory of the electromagnetic, an innovative sort of the radiating elements which has also been called the fractal antennas, has been fabricated. These fractal antennas are commonly printed configurations. Several different microstrip antennas

applying fractal techniques have been designed and created. Amongst those, some of the common fractal geometries are Sierpinski gasket or carpet, Hilbert fractal and Koch fractal [74]. Using the fractal ground plane in antennas' design will result in increasing the bandwidth of the antenna which is very important in designing the antenna.

3.3.7 The Fifth Stage: Designing Triangular Microstrip Patch Antenna with a Path-Square Shaped Fractal Ground Plane

To pursue the two primary goals which we have discussed previously for designing the antenna, the modified design of the initial design of the triangular microstrip patch antenna has been presented here. The plain ground plane of the previous design has been changed to the path-square shaped fractal ground plane, as shown in the Figure 3.13.

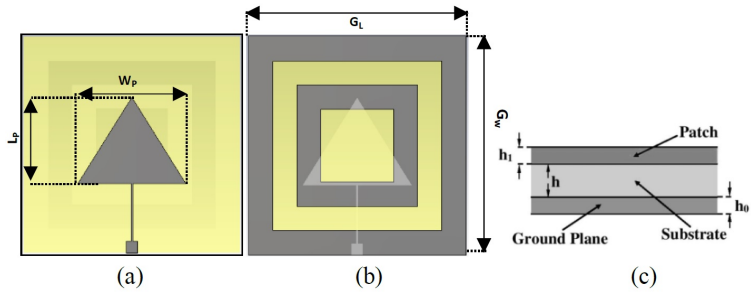

FIGURE 3.13: (a) Geometries of the designed triangular microstrip patch antenna, (b) Geometries of the path-square shaped fractal ground plane, and (c) different thicknesses of the different layers of the antenna.

The computed values of W_P and L_P are equal to 39.50 mm and 31.50 mm, respectively. The overall dimensions of the substrate and ground plane are $G_W \times G_L \times h_0$ and equal to 79 mm, 79 mm and 0.01 mm, respectively. The length and width of the rectangular patch are L_p and W_p, as shown in Figure 3.13 (a). A path-square shaped fractal ground plane is designed and used in this step, as shown in Figure 3.13 (b). In Figure 3.13 (c), the thickness of the substrate, patch and the ground plane is shown as *h*, h_1, and h_0, which are equal to 1.6 mm, 0.01 mm, and 0.01 mm respectively.

The bandwidth of the antenna could be calculated by using Figure 3.14 and Equation (3.13). we got the bandwidth of the triangular microstrip antenna with plain ground plane equal to 20.57 % in -10 dB. As it has been mentioned and discussed before the important issues in designing of the antenna are not only the enhanced bandwidth of the microstrip antenna, but also setting the corresponding operating frequency between 1-2 GHz. This design of the microstrip antenna is highly effective for the applications which work with the operation frequency between 1-10

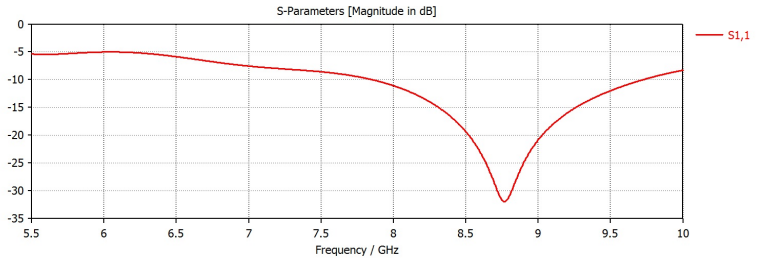

FIGURE 3.14: The return loss vs frequency S-parameter plot for the triangular microstrip patch antenna with the path-square shaped fractal ground plane.

GHz, but in the case of imaging the human brain, it cannot be useful. As, the corresponding operating frequency may typically be considered to set between 1-2 GHz. This band has demonstrated to be ideal and optimal for brain imaging [8].

3.3.8 The Final Stage: Designing Triangular Microstrip Patch Antenna with a Fractal Ground Plain

In this part, an effective microstrip patch antenna for imaging the human head with the aim of detecting intracranial haemorrhage and brain stroke is suggested and designed. The proposed procedure is based on the dielectric contrast of the healthy brain tissues and the haemorrhagic stroke tissues which can cause a strong microwave scattering. To achieve the desired outcome, we have designed several antennas. The last and the best design of the microstrip antenna for the stroke detection which operates between 1 and 2 GHz and has an enhanced bandwidth, has been presented as a triangular microstrip patch antenna with a fractal ground plain, as shown in Figure 3.15.

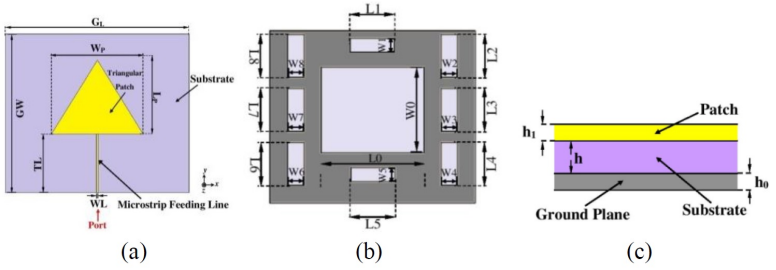

FIGURE 3.15: (a) Geometries of the designed triangular microstrip patch antenna, (b) Geometries of the fractal ground plane, and (c) different thicknesses of the different layers of the antenna.

This antenna has a single-layer structure and Figure 3.15 (a) shows the front view of triangular microstrip patch antenna. There are four different parts: triangular patch and microstrip

TABLE 3.1: Optimised dimensions of the proposed Triangular microstrip antenna with fractal ground plane (Unit: mm)

W_p = 39.5	W_L = 2.2	T_L = 16.8	L_0 = 39.50	L_P = 31.5
G_L= 79	G_W= 68.28	h = 1.2	$W_{(2,3,4,6,7,8)}$=6.61	h_0= 0.035
h_1= 0.035	$L_{(1,2,3,...,8)}$=17.07	W_0= 34.14	$W_{(1,5)}$=5.69	Sub = FR-4

feed line (at the top), the substrate (in the middle) and the fractal ground plane (at the bottom). The computed values of W_P and L_P are equal to 39.50 mm and 31.50 mm, respectively. The overall dimensions of the substrate and ground plane are $G_W \times G_L \times h_0$ and equal to 79 mm, 68.28 mm and 0.035 mm, respectively. The length and width of the triangular patch are L_P and W_P, as shown in Figure 3.15 (a). A fractal ground plane is designed and used in this step, as shown in Figure 3.15 (b). In Figure 3.15 (b), we can see the fractal ground plane, which consists of nine rectangles with different sizes. A fractal ground can be appropriately designed to ensure WB requirements [75]. In Figure 3.15 (c), the thickness of the substrate, patch and the ground plane is shown as h, h_1, and h_0, which are equal to 1.2 mm, 0.035 mm, and 0.035 mm respectively. The dimensions of the slots in the fractal ground plane are labelled by *L* and *W*. The 50 Ω discrete microstrip feeding structure is used at the bottom part of the patch. By optimizing the dimensions and shapes of the slots in the ground structure and the triangular antenna structure, the impedance bandwidth of this antenna can be clearly improved. The front view of the proposed antenna with the Fractal ground plane is shown in Figure 3.15 (a) and all the optimised dimensions of the proposed antenna are illustrated by Table 3.1.

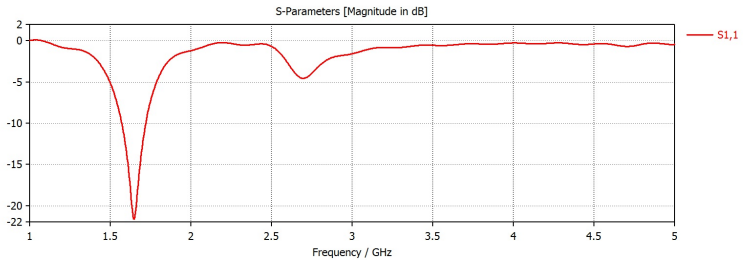

FIGURE 3.16: The return loss vs frequency S-parameter plot for the triangular microstrip patch antenna with the fractal ground plane

The bandwidth of the microstrip antenna could be calculated by using Figure 3.16 and Equation (3.13). We got the bandwidth of the triangular microstrip antenna with the fractal ground plane equal to 12 % in -10 dB. Moreover, the operating frequency of the proposed antenna is between 1 to 2 GHz (to be exact at 1.64 GHz), which is the optimal frequency for detection of the

stroke inside the human head. In the case of brain imaging the most important thing is to have higher penetration depth in order to penetrate through the skull (head bone) which is the hardest part of human head. The optimal frequency has been found in reference [8], from 1 to 2 GHz. Then we considered this range of frequency in whole part of this research including antenna design, phantom fabrication and imaging sections. In Chapter 6, the results are showing that the inclusion (which emulate the brain haemorrhage) can be seen in the mentioned frequency range (not in higher frequencies). This is due to the fact that higher frequencies do not alow good penetration inside the skull [8].

3.3.9 Design Flow

The stages of the design procedure are presented in the microstrip antenna design flow diagram, as shown in Figure 3.17. The first stage at the initial point of the diagram is the collection of an appropriate substrate, the corresponding sizes and dimensions of the microstrip patch antenna. All the parameters are accurately analysed and correctly simulated.

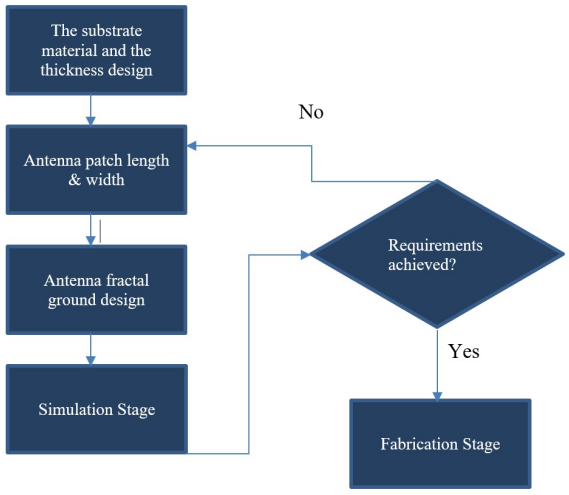

FIGURE 3.17: The microstrip patch antenna design flow diagram.

3.3.10 The Final Design of the Microstrip Patch Antenna

The last design of the constructed microstrip triangular patch antenna has been demonstrated in Figure 3.18; representing the designed antennas (a) front, (b) back and the fabricated antennas: (c) front, (d) back.

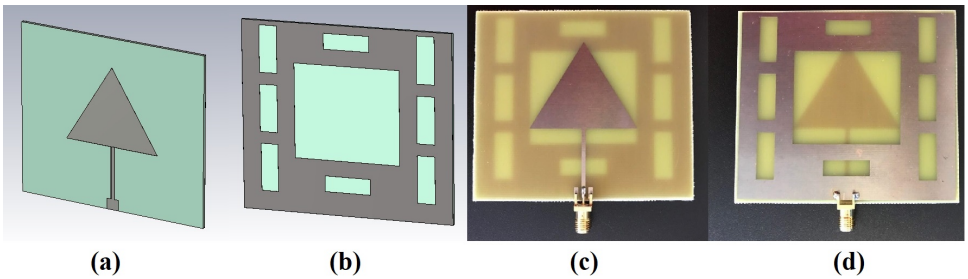

FIGURE 3.18: The designed triangular patch microstrip antenna: (a) front, (b) back and the fabricated antennas: (c) front, (d) back.

3.3.11 The Performance of the Proposed Microstrip Patch Antenna

The proposed Microstrop patch antenna has been simulated in the CST Microwave Studio 2017. VNA by the name of Anritsu MS2028C VNA Master manufactured by Anritsu EMEA Ltd has been used for the measurement part. As shown in Figure 3.19, the VNA is employed for measuring and displaying all four S-parameters of the microstrip patch antenna. The VNA Master MS2028C device is able to measure and cover a frequency band from 5 kHz to 20 GHz.

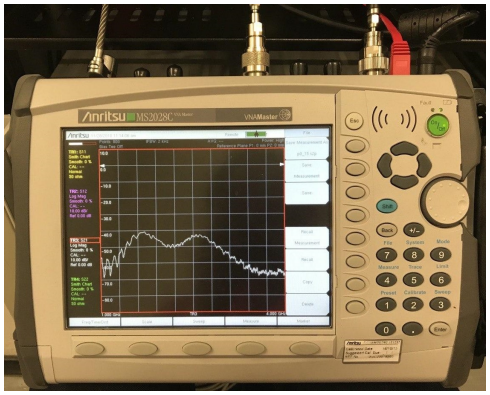

FIGURE 3.19: Anritsu MS2028C VNA Master manufactured by Anritsu EMEA Ltd used for the measurements in anechoic chamber.

The Frequency domain measurement is done in anechoic chamber employing a VNA arrangement for achieving the transfer function between two designed and fabricated microstrip patch antennas. The proposed fabricated microstrip patch antennas are positioned with their isosceles triangular axis of symmetry parallel to the y-axis of the reference system and omnidirectional at the azimuth plane and perform in free-space after completing the calibration.

3.3.12 Scatter Parameters

Figure 3.20 indicates both the measured and simulated scatter parameter S11 for the proposed microstrip patch antennas in free space, with an excellent and acceptable agreement from 1 to 5 GHz. Looking at Figure 3.16, the operational frequency is 1.6 GHz with a bandwidth over 10 %. As shown in Figure 3.18, the measured S11 in free space shows an excellent agreement with simulation results. Moreover, an operational bandwidth greater than 10 % centered at 1.6 GHz makes this microstrip patch antenna an ideal candidate for the brain imaging experiments. In actual fact, it has been shown in reference [76] that the higher frequencies are not suitable for the brain imaging due to the high signal attenuation, whilst lower frequencies will reduce the resolution [77]. There are some important factors which need to be mentioned, here. First, the constructed microstrip patch antenna's dimensions are exactly the same as the simulated microstrip patch antenna, as shown in Figure 3.18. Secondly, the S11 parameter is measured by using the VNA in anechoic chamber at the LSBU lab. To evade the influence from environment around the test site (normally lab site), the measurement were carried out in the anechoic chamber that can be effective in decreasing the influence from environment. At this time, the MWI cancer and stroke detection is rather too novel, so that the defined certification and quantitative evidence for defining the scatter parameters are still under investigation. Therefore, the definitions like good agreement, excellent agreement and acceptable agreement are on the basis of our experimental experience and observation, as the scatter parameters are completely linked to the imaging quality.

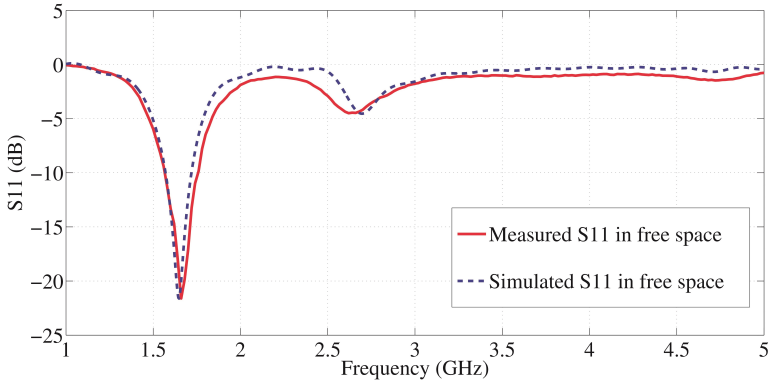

FIGURE 3.20: The simulated and measured reflection coefficient S11 of the patch antenna in free space.

3.4 Summary

This chapter presented and fully discussed the designing of a modified version of the WB microstrip patch antenna with fractal ground plane which has been provided to detect the brain stroke. The required performance of the antenna in terms of bandwidth and a specific operating frequency band, are obtained by optimising the dimensions and adding the fractal ground plane to the initial design of triangular microstrip antenna. The proposed designed microstrip patch antenna provides a WB operating frequency between 1 and 2 GHz. Therefore, the designed microstrip patch antenna completely meets the requirements for the detection of the brain stroke. The proposed triangular antenna has been fabricated in-house at London South Bank University (LSBU) and the correspondent S11 measurements have been taken in the anechoic chamber in free-space using a VNA device. The proposed microstrip antenna shows an excellent agreement between the simulation results and the experimental results. The proposed antenna is suggested to obtain a better performance of increasing the bandwidth of the antenna whilst preserving the same dimensions of the microstrip patch antenna. The final design obtains over 10 % increase in the bandwidth of the antenna. It is worth noting that the enhanced bandwidth offers the ability to have more penetration in order to detect the brain stroke.

Chapter 4

Human Head Phantom Design Experimental Measurements

4.1 Introduction

Same as most MWI recent researches on human head imaging using the electromagnetics simulations, we prepared a human head model for the simulation part and a human head phantom for experimental measurements. Chapter 4 explains the design of the human head phantom, with the simulation model in CST microwave studio and the construction of the human head phantom on the basis of the tissue emulating approach. The mono-static radar-based MWI procedure is presented then. The human head phantom is then applied to experimental measurements using the mentioned imaging procedure and the recorded scatter parameters in the frequency domain. Then in Chapter 5, the collected signals will be employed for creating microwave images to show the position of the haemorrhagic stroke inside the human head phantom.

In this chapter, we would only discuss the phantom design, simulation, and experimental setup. To follow Chapter 3, here we are using the designed antenna in a simulation with a human head model in two different stages. In the first stage, simulation will be performed once for a healthy human head which obviously means a head without stroke and then, for a human head with haemorrhagic stroke. In the second stage, simulation will be done at different positions of the antenna. These two approaches have been used through two different measurements procedures. For the first we have used anechoic chamber and for the second one we have used the MWI device which will be introduced and explained completely in this chapter.

4.2 Head Phantom

4.2.1 Simulated Phantom for Detecting the Brain Stroke

The design of the human head phantom for the WB transmission is comprised of several layers. So that, it is an approximation of a multi-layered model, by considering each layer to correspond to a specific tissue layer of the human body. For instance, the human head might be considered and modelled in different layers of skull (head bone), white matter and grey matter tissues. Brain stroke may then be constructed and added to the mentioned layers.

There are some parameters which should be considered, the one which plays a crucial role in indicating the properties of the layers belongs to the dielectric constant of each layer. The dielectric constant is frequency dependent. On the basis of the principle the head model is simulated in the CST microwave Studio software employing the finite-difference time-domain (FDTD) technique. The CST microwave Studio software has a library including a variety of the materials which are accessible with the aim of involving in the designing of the microwave devices in addition to the bio organs. This project has applied a simulation and model of the human body which will be described later, in this chapter. For the experimental measurements a human head phantom and a brain haemorrhagic stroke have been designed and fabricated. The proposed head phantom is a sort of hemi-ellipsoidal phantom which is able to provide a great realistic model.

4.2.2 Simulated Human Head (In CST Microwave Studio)

The Virtual Population (ViP) models consisted of a group of the accurate comprehensive high resolution body models formed basically from the data of the MRI collected from volunteers of different sex and age group, with different biological data. In this thesis, the latest design and creation of the phantoms called ViP3.1, has been used (provided by Information Technologies in Society (ITIS) Foundation, Switzerland). These models enhance the computational simulations within the 3D structures to an unparalleled level of details and precision by over 300 human organs and tissues for each model and the resolution of 0.5 mm $\times$ 0.5 mm $\times$ 0.5 mm.

For taking complete benefits of the mentioned resolution and also the realism, these models have been created by ‘state of the art’ physics solvers, which consist of thermal, acoustic, electromagnetic and computational fluid dynamics, and the models of the tissue, thus prevailing over the challenges met throughout model manipulation with the current commercial platforms. This sort of models is authenticated and the sufficiency among types has been evaluated for EM

simulations. Thereby, a 3D-model consisting of head tissues of the Ella model (ITIS Foundation, Switzerland) is employed with 2 mm $\times$ 2 mm $\times$ 2 mm isotropic resolution, as shown in Figure 4.1, where the antenna is positioned with its isosceles triangle axis of symmetry parallel to the y-axis of the reference system. The Ella model provides details of electric conductivity and relative permittivity for different tissues of a young and healthy female at the age of 26 [47],[78].

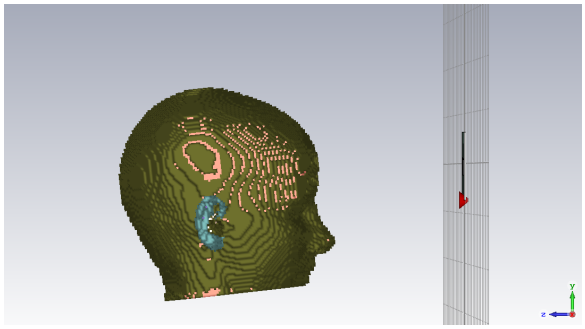

FIGURE 4.1: The simulated antenna and 3D head of the Ella model (ITIS Foundation, Switzerland) using CST software. The antenna is positioned with its isosceles triangle axis of symmetry parallel to the y-axis of the reference system; Ella model is positioned with its longitudinal axis parallel to the y-axis of the reference system [47],[78].

The applied human head phantom is presented in Figure 4.1. The mentioned 3D-human head model mainly contains a skin layer (with the thickness of 8 mm) [79], skull layer (with the thicknesses given in Table 4.1) [80], White Matter (with the thickness of over 50 mm) and Grey Matter (with the thickness of 2.5 mm) [79]. It is worth noting that the thickness of the skull layer varies in different parts of the human head (as given in Table 4.1). The skull bones are comprised of the rough layers with different thicknesses at variable points. The skull bones have not only the different thicknesses, but also they have different shapes which are varied due to the different subjects. So that, the occipital bone and the frontal bone have been shown as the thickest skull-bone and the second thickest skull-bone, respectively, as shown in Figure 4.2 [81] and given in Table 4.1 [80].

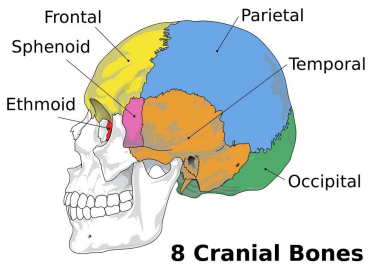

FIGURE 4.2: The skull bones (8 Cranial bones) [81].

The technologies which are employing electromagnetics, operate in the microwave frequency. Hence, in recent times there is an increasing focus on applying microwaves to the tissues which has encouraged the scientists to design phantoms. The mentioned phantoms are able to mimic the electrical properties of the real tissue at microwave frequencies.

4.2.3 Fabrication Method (Human Head Phantom)

Recently, numerous approaches for tissue representation have been projected [13],[82]. Several studies have been widely publicised in the literature, claiming the MWI system for scanning the human head abnormalities. The majority of these experimental measurements contain the simple human head phantoms [83],[84]. The mentioned researches have paid too little attention to the properties of head structures. Even though a few of the current studies defined the human head phantoms applying the electrical properties [85],[86], these researches still have privation of specific information of the brain fabrications. Therefore, to achieve effective experimental and scientific results of the head imaging, there is a pressing need for designing and fabricating

TABLE 4.1: Values of the thickness of the human skull bones [80].

Part of the skull	Males	Females
Frontal bone	6.3 mm	5.7 mm
Temporal bone	3.9 mm	3.4 mm
Occipital bone	7.7 mm	7.1 mm
Parietal bone	5.8 mm	5.6 mm
The majority of bones (All bones)	8.1 mm	7.4 mm
Central frontal bone	5-7 mm	5-7 mm
The majority of bones (Parietal and temporal bones)	3-4 mm	3-4 mm

a human head phantom with an inclusion of a brain haemorrhage. The most important components (after meeting the requirements) in the phantom fabrication consist of long-lasting, easy fabrication, and low cost. To experimentally validate a procedure for microwave explorations on the brain haemorrhages, a realistic phantom is required. In this chapter, a Three-dimensional (3-D) realistic human head phantom is designed and fabricated with the aim of performing the validation of the suggested imaging procedure.

A realistic phantom described in the literature [85] has concentrated mainly on a close similarity to the physical features of the head rather than to the actual dielectric properties. In this study [85], a substance with permittivity of 6 was employed to represent the exterior skull tissues including the bone. The phantom proposed in this work is instead primarily based on a close similarity to the real dielectric properties of the head tissues. Even though in reference [86], the authors assert that they provide a practical model for the detection of head damages, their research does not contain any proof and verification for the practical condition that includes several problems made by the neighbouring environment such as the electronics devices and computers. As so, the experimental measurement should be completed in anechoic chamber.

In this research, two human head phantoms have been proposed, first one for using with WB antennas with operating frequency of 1.6 GHz, and the second phantom for the MWI device. To achieve feasible fabrication, both phantoms have been fabricated using three layers, which mimics: I) Skull bone with realistic dielectric properties of cancellous and cortical bone, II) A combination of grey matter and white matter, III) Blood clot inclusion which will be described in a separate section, in future. Figure 4.3 demonstrates the mould for the hemi-ellipsoidal head phantom (the first head phantom). This phantom and the mould have been designed to be used on a rotatable table in anechoic chamber. The mould has been covered by a clear cellophane wrap (clear polypropylene rolls) to prevent the materials from spilling over the floor, whilst the table is rotating.

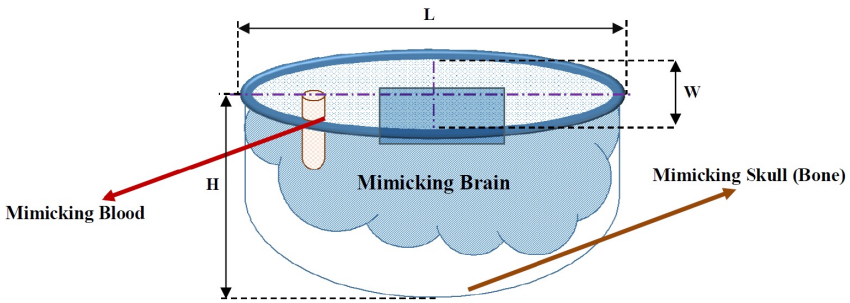

FIGURE 4.3: The design of the mould for the hemi-ellipsoidal head phantom for using in the anechoic chamber.

The dimensions of the designed mould should be as follows:

1. The horizontal axial diameters (L and W) and the height (H) of approximately 210 mm (back to front), 195 mm (sideways), and 120 mm, respectively for the phantom mimicking the skull.

2. The brain mould filled with white matter and grey matter equivalent material has horizontal axial diameters of 190 mm (back to front) and 165 mm (sideways), and height of 90 mm.

3. The brain haemorrhage mould/tube filled with blood clot equivalent material has a circular cross-sectional radius of 5 mm and a height of 35 mm.

These three steps define the fabrication process of the head phantom with haemorrhagic stroke which is designed to be appropriate for using in anechoic chamber. Since the phantom is used on the rotating table there is a restriction in the case of adding a cap to prevent the materials (specially liquids) from spilling over the floor, whilst the table is rotating. So that the mould has been covered by a clear cellophane wrap (clear polypropylene rolls). The other limitation regarding the phantom fabrication here is to consider the phantom with three layers/containers including the skull, the brain and blood clot layers/containers, as the quantities of white and grey matters are different amongst people, here we considered the average brain (average white and grey matters) in order to fabricate a phantom closer to the real tissues.

The suggested phantom is designed to mimic the skull bone with a thickness of roughly 10 mm, equivalent conductivity of 0.24 S/m and relative permittivity of 12 at 1.6 GHz. These values are presumed to provide an average value for the cancellous and cortical bone. In contact with the inner layer of the skull bone, there is dominating grey and white matter with an average conductivity of 1.01 S/m and permittivity of 44 at 1.6 GHz. The dielectric constant of each layer is given in Table 4.2, where the values have been derived from [44],[78],[87].

To simulate the dielectric properties of the human head different materials were used in order to approximate the values reported. The suggested phantom contains a solid representing skull filled with combination of the liquids imitating grey and white matter. Moreover, the selection of ingredients was driven by some further advantageous factors such as the low cost of materials, the ease of access (off-the-shelf) and the stability over long periods of storage time.

The details of the recipes for producing different mixtures are as follows [87],[88].
I. Skull mimicking tissue, as shown in Figure 4.4 (a):

-First, mix the flour and oil in a mixing bowl together and beat into a smooth batter. Stir until you no longer see dry clumps of flour. The stir should finish once the combination come

TABLE 4.2: Dielectric constant and conductivity at the frequency of 1.6 GHz [44],[78],[87].

Tissue	Relative Permittivity	Conductivity
Realistic human brain (combination of grey matter and white matter)	44	1.01 S/m
Skull	12	0.24 S/m

TABLE 4.3: Tissue representing ingredients for skull (bone) [87].

Ingredient (Grams)	Skull
Corn Flour	55
Sunflower Oil	35
Salt	0.3
Sugar	11
Deionised water	15

to be transparent with no air bubbles present. -Then, mix deionised water (which is at room temperature) with sugar and stir until the sugar was completely dissolved in the water. -Combine the two mentioned mixes until it formed a uniform shape. Carry on stirring the combination till all air bubbles evaporate and the combination gets uniform.

II. Brain mimicking tissue, as shown in Figure 4.4 (b): -In the mixing bowl, stir a mixture of glycerol and deionised water with ratios of 40 % and 60 %, respectively as given in reference [88]. It should be noticed that during describing the construction processes, the volumes of the chemical material (which have been used in providing the mixtures) were not mentioned. To fabricate each layer, the amounts of ingredients of the recipe for emulating the skull tissue have been shown in Table 4.3 [87].

Owing to the empirical use of only the top half of the head, a plain hemi-ellipsoidal shape with external horizontal axial diameters of 210 mm (back to front) and 195 mm (sideways), with height of 120 mm, was selected. Moreover, the brain mould filled with white matter and grey matter equivalent material has horizontal axial diameters of 190 mm (back to front) and 165 mm (sideways), and height of 90 mm. As Figure 4.5 shows, three different volumes of container are subsequently placed inside each other. Each layer of the head phantom has been fabricated using mixtures of the constituent materials with the proper ratios.

I use the Epsilon dielectric measurement device which is called Biox Epsilon Model E100

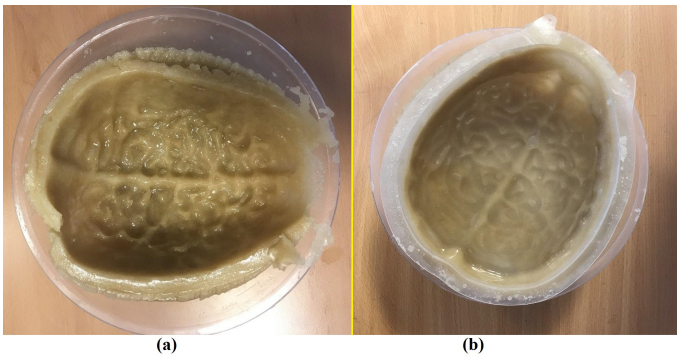

FIGURE 4.4: (a) The skull emulating phantom (one layer), and (b) the skull and the brain emulating phantom (two layers).

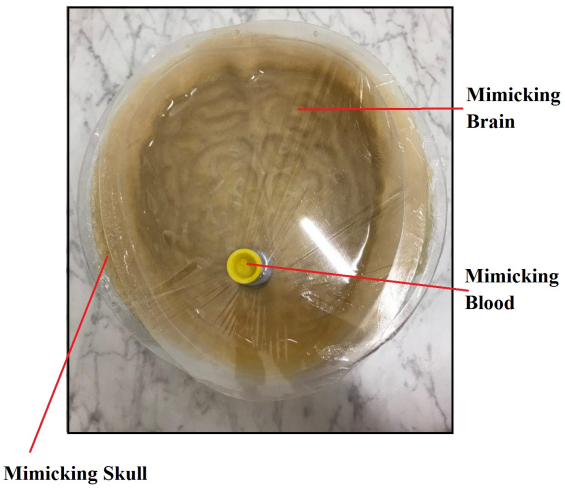

FIGURE 4.5: The fabricated head phantom is comprised of three different layers representing the skull (bone), human brain, and the brain haemorrhage.

and fabricated by Biox-System Company, in order to measure the dielectric properties of the tissue-indicating phantom ingredients. Epsilon is a device with a touching base structure applying a fingerprint sensor which replies to the capacitance. This measuring instrument is able to be applied for measuring liquids and soft solids. As presented in Figure 4.6 Epsilon dielectric measurement device comprises a base for mounting the probe through its sensor surface horizontal and facing upwards. To make sure of reliable measurements from time to time and from device to device, first this device has been calibrated by employing ingredients with the identified dielectric constant (ε). It is worth noting that the Epsilon dielectric measurement device cannot provide any data regarding the conductivity.

FIGURE 4.6: The Epsilon dielectric measurement devices, when used to measure the dielectric constant (ε) of the combination of the materials.

The dielectric properties of the skull imitating tissue's mixture were measured employing the Epsilon dielectric measurement device (Biox Epsilon Model E100 fabricated at Biox System Company Ltd) and for the mixtures of the brain and blood clot representing tissue, the dielectric probe (Keysight technologies, M9370A), connected to a network analyser was used to measure the electrical properties at room temperature.

The Epsilon is a device for contact measurement using a fingerprint sensor which reacts to capacitance. It is useful for measurements on isolated soft liquids and solids. It is worth mentioning that this device cannot provide the dielectric value at the frequency of interest, but can provide the permittivity values at frequency of 0 Hz. Nevertheless, this is appropriate for a material which is made up of constituents that do not experience any changes with frequency variation, such as flour and oil. Since the skull representing tissue comprises mainly a high percentage of corn flour and sunflower oil, the obtained measured permittivity with this device at 0 Hz frequency has been considered equivalent to its permittivity at a frequency of 1.6 GHz. This does not hold true for brain and stroke recipes that are fabricated chiefly by a high percentage of glycerine.

The above description is for the fabrication of the head phantom which then will be used in anechoic chamber. Frequency domain WB experimental measurements are done in LSBU anechoic chamber by employing a VNA device in order to achieve the transfer function among two proposed Microsrip patch antennas. This description will be described more in a specific section of measurements in anechoic chamber. There is another design of the phantom which is performed to use for MWI device. The second phantom has been fabricated with the same material as the first phantom. Only the mould is differently designed to be able to use specifically in MWI device. Figure 4.7 demonstrates the mould for the hemi-ellipsoidal head phantom (the second head phantom). This phantom and the mould have been designed to be used in MWI device. The dimensions of the designed mould should be as follows:

1. The diameter and the height of the bigger mould (the outer layer) are equal to 110 mm

(back to front), and 115 mm (top to bottom), respectively for the phantom emulating the skull.

2. The brain mould (the smaller mould and inner layer) filled with white matter and grey matter equivalent material has diameter of 100 mm (back to front), and the height of 105 mm.

3. The brain haemorrhage mould/ tube fill with blood clot equivalent material has a circular cross-sectional radius of 5 mm and a height of 35 mm (the tube is same in both sort of phantoms).

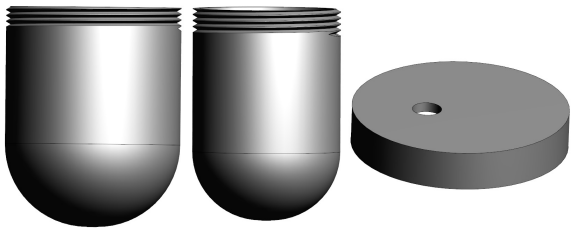

FIGURE 4.7: The design of the mould for the head phantom using with MWI device.

These three steps define the fabrication process of the head mould for the human head phantom with haemorrhagic stroke which is designed to be appropriate for using in MWI device. These moulds have been covered by a designed lip with the diameter of 110 mm (Back to front) to prevent the materials from spilling over the floor, during phantom rotation. The material which has been used for designing the mould is ABS-Plastic and the design has been done using Autodesk AutoCAD software.

Figure 4.8 shows the fabricated mould for the head phantom appropriate to the needs of the MWI device. The limitation regarding the phantom fabrication here is to consider the phantom with three layers/containers including the skull, the brain and blood clot layers/containers, as the quantities of white and grey matters are different amongst people, here we considered the average brain (average white and grey matters) in order to fabricate a phantom closer to the real tissues. Moreover, another limitation of phantom fabrication here is related to the size of the hole/a cup which allows the object (needed to be imaged) to insert. All the dimensions of the second phantom is limited to be appropriate to the dimensions of the hole/cup.

FIGURE 4.8: The fabricated head phantom is comprised of three different layers emulating the skull (bone), human brain, and the brain haemorrhage for using in MWI device.

I will discuss more about the MWI device in this chapter and in a separate section.

4.2.4 Simulated Spherical Brain Stroke (Using CST Microwave Studio)

In this thesis, a phantom validation of a low complexity MWI device operating in free space at the operating frequency of 1.6 GHz is presented. A sphere haemorrhagic brain stroke has been designed and simulated in CST microwave studio, as shown in Figure 4.9 (a). To simulate the existence of a haemorrhagic stroke inside the head model, we have considered a spherical region with the dielectric properties of blood clot, with radius of 10 mm, relative permittivity and conductivity of 60 and 1.79 S/m at 1.6 GHz, respectively in the head model [47],[78]. This haemorrhagic brain stroke target comprises of the blood clot properties and has been inserted into the frontal lobe of the human brain layer, as presented in Figure 4.9 (b).

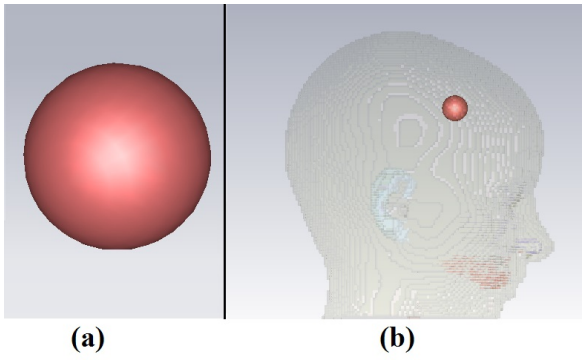

FIGURE 4.9: (a) A simulated brain haemorrhage, and (b) a 3-D human head model with an inserted spherical haemorrhagic brain stroke using CST Microwave software.

4.2.5 Fabrication Method (Brain Haemorrhage Phantom)

A realistic brain haemorrhage phantom is created to provide a prototype for the research of brain imaging. The fabrication process for the phantom of haemorrhagic brain stroke is completely similar in both human head phantoms. The only difference is the moulds which have been designed and applied. The mould for the first phantom is bigger and suitable for using at rotatable table in anechoic chamber (a more realistic head phantom than the second one), and the second phantom is appropriately designed and fabricated for application in the MWI device (a smaller head phantom). It is worth noting that, the external plastic mould in both head phantoms has been supposed to represent the skin layer. Figure 4.10 shows the brain haemorrhage phantom and mould. As it has been mentioned in previous section, the brain haemorrhage mould/tube filled with blood clot equivalent material has a circular cross-sectional radius of 5 mm and a height of 35 mm (the tube is same in both phantoms) with the relative permittivity and conductivity of 60 and 1.79 S/m at 1.6 GHz, respectively. The detail of the brain haemorrhagic stroke phantom fabrication method is as follows.

- **Blood clot mimicking tissue**:

The blood clot has been emulated using a mixture of glycerol and deionised water with ratios of 15 % and 85 %, respectively as given in reference [88].

FIGURE 4.10: A cylindrical tube with the brain haemorrhagic stroke mimicking mixture inside.

In reference [88], the authors present information and graphs of measured dielectric properties of different glycerol concentrations as a function of frequency. For fabricating the brain haemorrhage and the human brain, the information of reference [88] has been used. The dielectric properties of the skull representing tissue's mixture were measured and presented in a table in the results chapter.

4.3 Simulation

In Chapter 3, the design and fabrication of the proposed microstrip patch antenna have been discussed. In the current chapter, the 3-D human head model and a sphere representing the brain haemorrhage have been presented. The human head model has been simulated in the CST Microwave software. The aim of this section is to investigate the performance of the proposed microstrip antenna in the presence of the human head and compare the simulation results with the measurements results.

An antenna configuration is proposed and used to measure the human head phantom, with the scattering parameters recorded. This antenna passes a pulse through the head phantom, and then the same antenna receives the reflected wave. The Microwave patch antenna is placed on top of the head phantom, with the distance to the head surface being 17 cm. The front of the antenna is located towards the brain haemorrhagic stroke. This antenna is then moved to scan different locations in the steps of the angles of 0°, 5°, 40° and 45°. The dimensions of the 3-D human head model are 210 mm $\times$ 195 mm $\times$ 120 mm.

4.3.1 Simulation (Using the Proposed Antennas and 3-D Head Model)

Figure 4.11 demonstrates the measured and simulated scatter parameter S11 for the proposed antenna near the healthy human head. The measured S11 in free space has been discussed before, in Chapter 3. Now we are going to discuss the measured S11 in front of human head using the corresponding simulation data and measurement data.

The measured S11 in front of a healthy human head (same as the results with measured S11 in free space, as discussed in Chapter 3) indicates excellent agreement with the simulation results (using a healthy 3-D human head), as shown in Figure 4.11. In addition, measurements reveal that matching and the bandwidth slightly increase in the presence of the human head (in comparison to Figure 3.16, Chapter 3).

Furthermore, an operational bandwidth greater than 10 % centred at 1.6 GHz makes this antenna an ideal candidate for brain imaging experiments. In fact, it has been shown that higher frequencies are not suitable for brain imaging due to the high signal attenuation, while lower frequencies decrease the resolution [66].

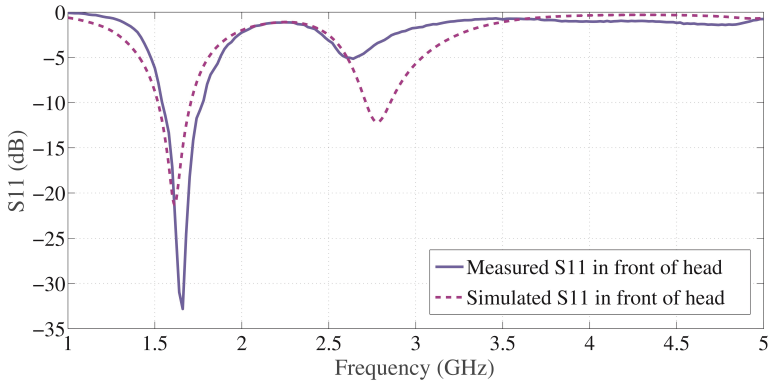

FIGURE 4.11: Simulated and measured reflection coefficient S11 of the patch antenna: (a) in free space and, (b) in front of human head.

As shown in Figure 4.11, the operational frequency is 1.6 GHz with a bandwidth over 10 %. It should be highlighted that, in both the simulation and the experimental measurements, the transmitting antenna has been placed 17 cm away from the centre of the Ella model's head and the healthy human head. It is worth noting that, the proposed triangular microstrip antenna has been fabricated in-house at London South Bank University (LSBU) and the correspondent S11 (input port voltage reflection coefficient) measurements have been taken in the anechoic chamber, both in free-space and in front of a human head using a VNA.

4.3.2 Simulation (Using the Proposed Antennas with a Healthy Head Model and a Head Model with a Haemorrhagic Stroke)

This section will continue to provide the initial data and results which are then used in the results chapter for imaging. In order to achieve this goal, different working steps have to be performed. First, the simulation has been done for two different situations, i.e. for a healthy head model which is mentioned before as Ella model and a head model with a spherical emulated haemorrhagic stroke, and for four different positions of the antenna with respect to Ella model. It should be pointed out that, rather than rotating Ella model around its longitudinal axis, the four different positions from the angles of 0°, 5°, 40° and 45°, have been synthetised by rotating the microstrip patch antenna. Figure 4.12 displays the magnitude of y-component of the electric field on an xz-plane for:

(a) Ella model (abbreviated as Ey)

(b) When the emulated stroke is included in the Ella model (denoted as Ey-WSTR) and

(c) The difference between the Ella model and the Ella model with stroke (abbreviated as dEy)

Moreover, the y-component of the electric field on one external surface of the head is calculated and used for performing the imaging, as shown in the results chapter. It should be pointed out that only the y-component of the electric field will be used for performing the imaging, due to x and z components vanishing. Specifically, the y-component of the electric field is calculated on a circular grid of points with radius of 110 mm and 6° phi sampling just outside the Ella head model. In Figure 4.12, the external ellipse with white dots represents the head contour, while the haemorrhagic stroke area is the yellow region at the bottom left of the head (located at frontal lobe of the head model) in Figure 4.12 (c).

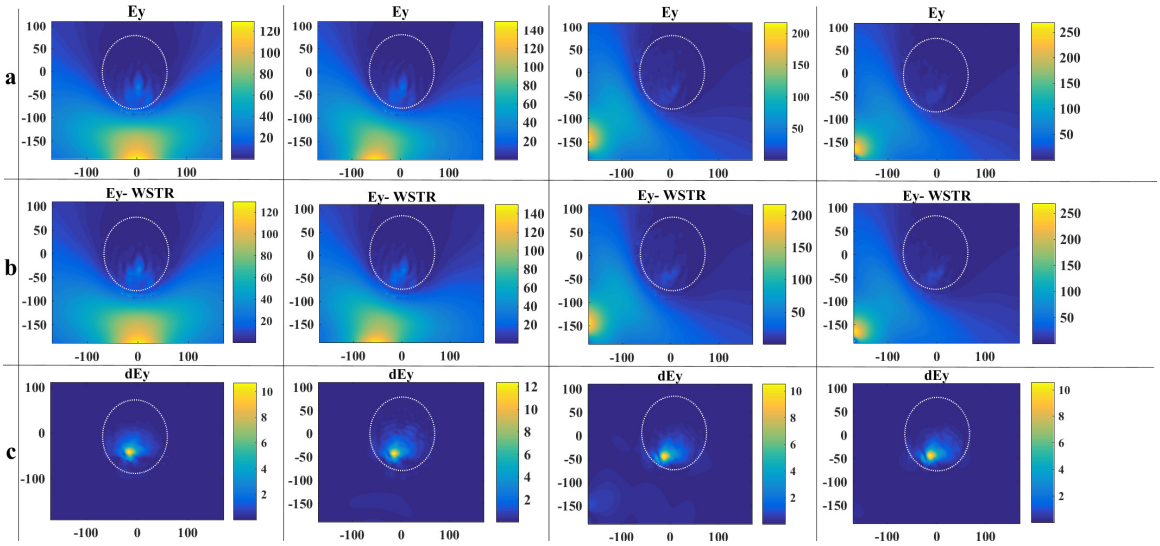

FIGURE 4.12: The y-component electric fields on an xz -plane from the angles of 0°, 5°, 40° and 45° for; (a) the Ella model, (b) when the emulated stroke is included in the Ella model and (c) the difference between the Ella model and the Ella model with stroke. The vertical colour-bar at the right of each figure indicates the intensity of the electric field (in V/m). Both x and z axes show the distance in millimetres.

In Figure 4.12, the white dots have been employed, in order to show the area of the head model and also, to indicate the position and distance of the brain haemorrhage inside the head area. The yellow region is demonstrating the exact positon of the brain haemorrhage which has been considered in frontal lobe (as we discussed previously in chapter two and the current chapter). It is worth noting that, as it is obvious in the simulation, the transmitting antenna has been located in a position which keeps the distance of 17 cm from the centre of the Ella model's head. The formations of the microwave images are not easy, as the collected signals must be processed first.

On the basis of the theory of electromagnetics, the disjointedness of a boundary would origin a huge incident reflection of the electromagnetics wave. The level of the reflection is

highly on the basis of the dielectric constant difference. Therefore, the huge reflection of the brain haemorrhagic stroke owes to the big difference of relative permittivity among the healthy and unhealthy (such as brain haemorrhage) tissues. Moreover, the proposed microstrip patch antenna is not only able to confirm that enough energy penetrates trough the phantom but also, decreases the district of the illumination.

4.4 Experimental Measurements Setup

The hemi-ellipsoidal head phantoms are also measured experimentally using VNA device. As we have discussed in the current chapter, two head phantoms have been appropriately designed and fabricated for using inside the anechoic chamber and employing with the MWI device. This section describes the measurement set up of the human head phantom using the designed and fabricated microstrip patch antenna. The human head phantoms are discussed separately; also the scatter parameters are measured using an antenna pair in the anechoic chamber and much the same in Mamowave device (using two antennas). However, in this chapter the microwave images are not presented. The scatter parameters obtained are analysed and processed in the next chapter and then applied for creating the microwave images.

4.4.1 Experimental Measurements

In this section, an experimental measurement setup applying a pair of microstrip patch antenna has been proposed. Instead of using a single microstrip patch antenna configuration (which is applied in simulation section), a pair of microstrip patch antenna have been used in the experimental measurements section. One of the antennas is used as a transmitting antenna and the second antenna is used as the receiving antenna. This procedure requires a very simple hardware setup, i.e. one transmitting antenna and one receiving antenna (that is coupled through a VNA) which rotate in free space around the object to collect the signals in a multi-bistatic fashion.

This antenna similarly to the simulated antenna (in the single antenna configuration), changes its position to scan the head phantom. For the measurements, the transfer function S21 (here, S21 is the parameter representing the complex transfer function from the transmitting antenna to the receiving antenna and the notation 1 and 2 denotes the transmitting and receiving antennas, respectively) is recorded instead of S11. The operating principles are almost the same as the one with the single antenna configuration. The incident wave is transmitted to the head phantom by the transmitting antenna, and then the receiving antenna receives the reflected wave.

The antenna pair has been shown to be a configuration which has been widely used, in the study of bistatic radar imaging systems. Both the transmitting antenna and the receiving antenna are linked to the transmitter and the receiver, correspondingly.

It is worth noting that in this study, the antenna is linked with a VNA. The VNA has the potential for measuring and displaying the scattering parameters. The main aim of this work is to study and analyse the detection of the brain haemorrhagic stroke rather than the design of the receiver and transmitter. Therefore, this VNA device, offers the possibility of using the antenna pair configuration. In the antenna pair configuration, the receiving antenna, which is coupled through a VNA, rotates around the object to collect the signals in a multi-bistatic fashion and scan the human head phantom. In comparison to the configuration of the single antenna, the antenna pair configuration employs one transmitting antenna to pass the signal through the human head phantom, and one receiving antenna to collect the received signal.

This section explains the set up in anechoic chamber with the antenna pair configuration. Frequency domain measurements have been carried out inside an anechoic chamber, to gather the transfer function S21 between the two antennas through a VNA. The fabricated microstrip antennas were used, after calibration. In more detail, the transmitting antenna was connected to port 1 of the VNA and the receiving antenna connected to port 2 of the VNA, as shown in Figure 4.13; S21 is the parameter representing the complex transfer function from the transmitting antenna to the receiving antenna.

FIGURE 4.13: The VNA used in anechoic chamber. Port 1 is connected to the transmitting antenna and port 2 is connected to the receiving antenna.

The prepared phantom was positioned at the centre of a rotating table. Figure 4.14 shows the phantom and fabricated antennas inside the anechoic chamber.

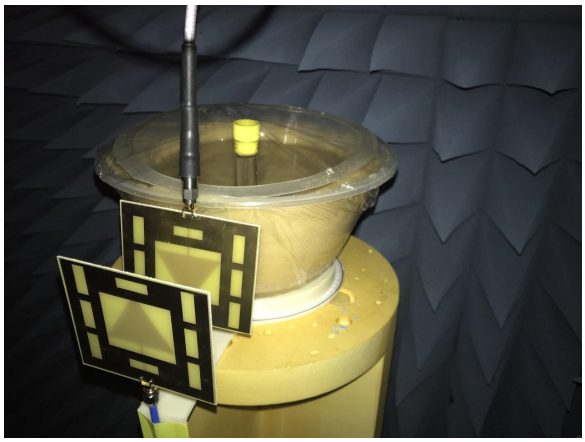

FIGURE 4.14: Phantom's position on the rotatable table inside the anechoic chamber.

The multilayer phantom contains a target inclusion having specific conductivity and/ or permittivity of blood clot. The aim is to find the existence and location of the target, using the measured field of the receiving antenna, which is collected at many points rx_{np} placed all around the phantom surface. Through both simulations and measurements, it has been verified that the field reconstructed in the medium under test will display a mismatch around the transition region of the two media, which is where the target is positioned. This mismatch permits detection. It is worth noting that for each set of measurements, the transmitting antenna has been placed 17 cm away from the centre of the rotating table, the same way it was done in simulations, whilst the position of the receiving antenna has been placed 3 cm away from the transmitting antenna and mounted on a computer controlled rotating stage, as shown in Figure 4.15.

FIGURE 4.15: The measurements setup in anechoic chamber.

Figure 4.16 shows the sketch of the measurement setup, where the hemi-ellipsoidal shape

phantom of the head is shown in light blue. The black and green dashed circles indicate the perimeter where the transmitting and receiving antennas can be moved circularly on the azimuthal plane, in order to irradiate and thereafter receive the signals from different directions. The antennas are at the same height. For each transmitting position, we recorded the S21 at N_{PT} = 60 receiving positions. Specifically, we measure S21 at the points $\mathrm{rx}_{np} \equiv (a_0; \phi_{np}) \equiv \overrightarrow{\rho}_{np}$, displaced along a circular surface having radius a_0. a_0 is the distance between the centre of the rotating table and the receiving antenna (also shown in Figure 4.14) which is 14 cm [66]:

$$\mathrm{S21}_{\mathrm{t}x_m}|_{\mathrm{r}x_{np}} = \mathrm{S21}_{np,\mathrm{t}x_m} \quad \text{with} \quad np = 1, \ldots, N_{\mathrm{PT}} \tag{4.1}$$

Subscript *m* indicates the transmitting positions tx and *np*=1, 2,. . ., N_{PT} the receiving positions. It must be emphasized that, instead of moving the transmitting antenna here, the transmitting positions are synthesised by suitably rotating the phantom. A total number of 8 transmitting positions have been synthesises (*m*=1,. . .,8), divided in four doublets displaced 90°, with doublet consisting of two closest transmitting positions displaced 5° from each other.

The doublets displaced 90° in order to show and prove that the stroke can be detected at four different places and orientations, not only at a single place in the human head phantom. It should be highlighted that the considered place should be known because during the imaging process, we need to know where is the inclusion placed exactly for distinguishing the inclusion from the artefacts inside the resulting images. To summarize, the following transmitting positions have been synthesised: 0° and 5°, 90° and 95°, 180° and 185°, 270° and 275°. For the purpose of exploiting how the signals vary at different frequencies, complex S21 values were recorded over a full range of frequency between 1 and 2 GHz, using a frequency sample spacing of 5 MHz.

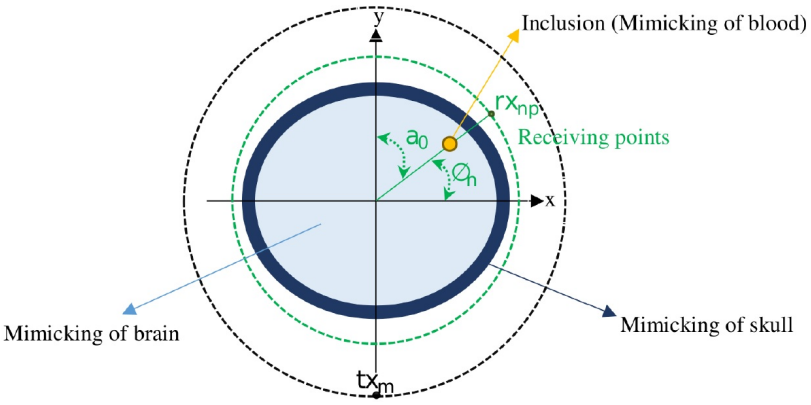

FIGURE 4.16: Pictorial view of the measurement.

4.4.2 Measurements (Using MWI Device)

MWI procedure is based on the scattering of electromagnetics waves. It is capable of fulfilling several essential requirements such as being fast, portable (in consequence of dimensions of the devices), having non-ionising nature, and reduced intensity needed for achieving imaging. These significant features of MWI not only can offer a possibility for having an appropriate and safe imaging modality for repeated medical applications, but also for applying the relevant devices at small medical centres for both monitoring and detection of a variety of cardiovascular diseases (hence MWI relies on significant differences in dielectric properties consisting of electric permittivity and conductivity between the healthy and stroke tissues). These differences provide an opportunity for a functional map of the examined anatomical district to be achieved. More in detail, a haemorrhagic stroke inside a healthy human head illuminated by an electromagnetics field transmitted by a dedicated antenna may generate a scattered field, which, if properly processed and measured, may be applied to detect and locate the brain haemorrhage itself.

Numerous MWI prototypes and devices for brain stroke diagnostics have been Offered recently [9],[23],[54],[56],[60]. Amongst the whole researches in medical MWI prototypes that we cannot fully review them here, some experimental schemes have been developed for breast cancer and brain abnormalities detection (as we have completely discussed in Section 2.4). Two prototypes (which have been recently tested on human body) are the greatest prominent types amongst MWI prototypes. The first prototype is the "Stroke-finder", which was developed by Medfield Diagnostics at Chalmers University [54],[89], and the second prominent type is the "BRIM G2" developed for brain scanning at EMTensor [56]. The Medfield Diagnostics device is a prototype used in detection, classification and discrimination between two sorts of intracranial bleedings (brain haemorrhage or brain ischemia) in order to rescuing patients at the early onset of stroke. An early diagnosis of stroke using this device can be performed on the basis of the automated classification achieved by making a comparison between the data of the measurements and the database, which has been achieved through the collected data from examined patients.

The device is categorised according to its ordinary and compact hardware and consists of 12 transmitting/receiving triangular printed antennas fixed on a support which is capable to be adapted to the patient's head (e.g. helmet shape). Although, the early clinical trials have been represented in reference [89], it is worth noting that this device cannot provide images. Hence, the expected role of "Stroke-finder" device is to accompaniment standard imaging apparatuses. The "BRIM G2" is developed to exhibit brain stroke tomography. This is a high

complexity device comprised of 177 radiating elements (rectangular ceramic-loaded antennas operating at 1 GHz) [56]. Although this prototype successfully detected the stroke and offered good experimental reconstruction results for brain monitoring, it suffers from some considerable disadvantageous. The configuration of 177 radiating elements can significantly increase both the size and cost of this device. Therefore, the EMTensor has several limitations. Moreover, to perform the image reconstruction, there is a need for processing a significant quantity of measured data and finding a solution to a nonlinear and ill-posed inverse scattering problem (as a result of using the MWT system). The need to solve inverse problems can significantly increase the computational overhead, elaboration times and possibly cause false solutions. The configuration of brain imaging MWT scanner has been studied in references [21],[90] for optimising the design of antenna array and establishing the appropriate frequencies and properties of the coupling medium. In a MWT procedure, the array antenna transmits electromagnetics waves and the object scatters this waves (the waves penetrate into the tissue). Then, the receiver will receive and collect the scattered field [91].

The MWT algorithm applied to reconstruct a map of the dielectric properties relevant to the imaged area for locating an object with unidentified dielectric properties, by finding a solution to a nonlinear and ill-posed inverse scattering problem [92],[93]. Taking into account the mentioned limitations of MWT systems and the medical necessities of brain stroke detection, another purpose of this research is to investigate and quantify the capability of our MWI device in detecting brain haemorrhage, through phantom experiments (by applying a simple human head tissue and brain haemorrhage mocking phantoms).

A robust procedure on the basis of the HP method (which will be discussed more in Chapter 5) is developed for haemorrhagic brain stroke detection using MWI technique. The head imaging is also investigated through phantom measurements in an anechoic chamber (as discussed in Section 4.4.1), using two microstrip patch antennas in free space. Since the results coming from measurements inside the anechoic chamber is not as realistic as clinical trials reports and also there is a medical requirement for a brain stroke portable imaging device, we have come to a decision on a new brain haemorrhage imaging prototype. Most research, containing the researches which have been done by LSBU, has principally been concentrated on the detection of breast cancer. Recently, a portable MWI device, which operates in free space with two azimuthally-rotating antennas, is developed and employed for breast cancer detection [23]. More in details, the two antennas rotate all around the breast to collect the signals in a multi-bistatic fashion. This research has directed to apparatus being built which has successfully detected inclusions in breast-emulating phantoms [23] and the device has been successfully verified in preliminary

clinical trials [22]. We have adapted the methods used to detect brain cancer and have produced promising research using the technology for stroke detection. Moreover, in this section, an experimental measurement will be performed using MWI device. A multi-layered phantom representing human head with a brain haemorrhage is realised, applying millimetric cylindrically shaped inclusion to emulate a haemorrhagic brain stroke.

A specific mould for using in MWI device has been designed and fabricated, as it has been completely explained and discussed before, in the current chapter. The MWI device consists of an aluminium cylindrical hub containing two antennas, one transmitting (tx) and one receiving (rx). The hub is internally covered by microwave absorbers, and is equipped with a hole with a cup, allowing the insertion of the object to be imaged. Inside the cylindrical hub there are one transmitting antenna (horn type) and one receiving antenna (vivaldi type), having voltage standing wave ratio (VSWR)<3 in the band 1 to 6.5 GHz. The antennas are installed at the same height, in free space and can rotate around the azimuth in order to collect microwave signals from different angular positions. More details can be found in reference [23]. It should be noted that we did not design the antennas and MWI device, we only used this device to measure and collect the data for obtaining images and apply different artefact removal methods. The tx and rx are connected to a 2-port VNA (S5065, Copper Mountain, Indianapolis, IN) which operates up to 6.5 GHz. Measurements have been performed by recording the complex S21 in a multi-bistatic fashion, i.e. for each transmitting position tx_m the receiving antenna is moved to measure the received signal every 4.5°, leading to a total of 80 receiving points rx_{np}. Concerning the transmitting positions, all the experiments have been done by employing 15 transmitting positions, displaced in 5 triplets cantered at 0°, 72°, 144°, 216°, and 288°.

Figure 4.17 depicts the sketch of the set up configuration of the MWI device, where the light green dashed circle indicates the perimeter where the receiving antenna can be moved circularly, in order to receive the signals from different directions. As it has been shown in Figure 4.17, for each triplet the three transmitting positions are displaced by 9°. For each transmitting and receiving positions, the complex S21 is collected from 1 to 6.5 GHz, with 5 MHz sampling. This band has demonstrated to be ideal and optimal to do brain imaging [8].

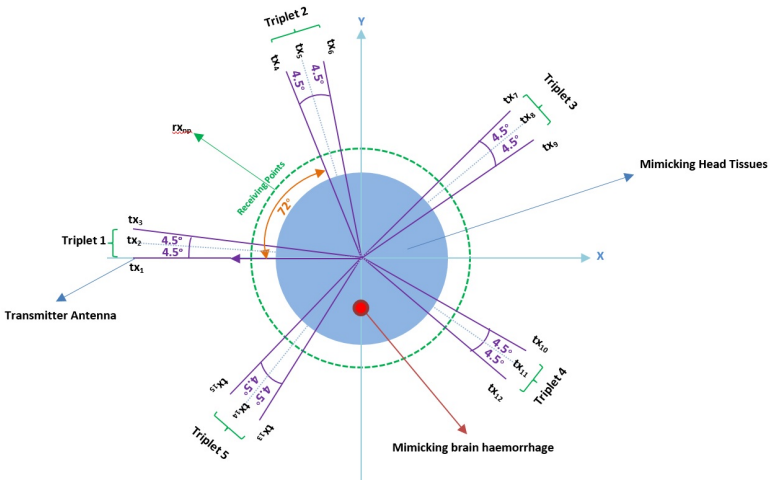

FIGURE 4.17: Pictorial view of the MWI device configuration.

As the Pictorial view of the MWI device configuration shows, the process applied three transmission points (called triplet) detached by x degrees, by each transmission measured at 80 points around the circumference of the experiment area. The points will transmit at discrete frequencies from 1 GHz to 1.5 GHz with a frequency sampling of 5MHz. This provided a total of 1101 discrete frequencies. The experiment had been repeated with changing the transmission point separation delta x, measured in degrees. The data which has been employed, is the S21 value taken at the 80 points around the circumference of the cylinder. S21 is a value normally applied with RF Engineering. As we described before, it is a complex number which shows the transmission of waves from port 1 to port 2. The complex components of the number represent the Amplitude and Phase shift of the signal. The transmitting source position x has been set as 3 transmission points spaced 4.5° apart at 0. Specifically, we measure complex S21 at the points $\mathrm{rx}_{np} \equiv (a_0; \phi_{np}) \equiv \overrightarrow{\rho}_{np}$, displaced along a circular surface having radius a_0. Radius a_0 is the distance between the centre of the azimuthal plane and the receiving antenna which is 7 cm. For each transmitting position, we recorded the S21 at N_{PT}=80 receiving positions. These definitions will be used in imaging procedure, through the next chapter. The images and results will be presented in Chapter 6.

4.5 Summary

In this chapter, two moulds for two multi-layered human head phantoms have been proposed. The first head phantom has been designed and fabricated to be used on a rotatable table inside the anechoic chamber. The other head phantom has been designed to be employed in MWI device. The second phantom has been fabricated with the same material as the first phantom.

Only the mould is differently designed to be able to use specifically in MWI device. The 3-D human head model is used in the CST Microwave software with the proposed microstrip patch antenna. Through both the simulation and measurements, it has been verified that the field reconstructed in the medium under test will display a mismatch around the transition region of the two media, which is where the target is positioned. This mismatch permits detection. Furthermore, the antenna is on the basis of the active mono-static radar system. In experimental measurements, two same microstrip patch antennas are used. One of the antennas used as the transmitting antenna, and the other one as the receiving antenna. These two proposed antennas are applied to measure the hemi-ellipsoidal head phantom inside the anechoic chamber with the complex S21 values which were recorded over a full range of frequency between 1 and 2 GHz (in the frequency domains). The transmitting antenna has been placed 17 cm away from the centre of the rotating table, the same way it was done in simulation, whilst the position of the receiving antenna has been placed 3 cm away from the transmitting antenna and mounted on a computer controlled rotating stage.

Moreover, the same system has been considered for the MWI device which comprises the aluminium cylindrical hub comprising two antennas, one as a transmitting tx and one as a receiving (rx) antenna. Also, a head phantom with a specific mould is proposed to be used with this MWI device. In addition to the description of the MWI device, the procedure of collecting the complex S21 at the frequency range of 1 to 1.5 GHz has been described by explaining the transmitting and receiving positions. These collected scattering signals would be processed to produce the microwave images in order to indicate the brain haemorrhagic stroke position, through the next chapter.

Chapter 5

Imaging Procedure and Artefact Removal

As discussed in Chapter 2, brain strokes can be categorised as haemorrhagic or ischemic strokes. Different brain strokes correspond to different diagnosis methods. In this study, we just focus on the brain haemorrhage. Also, as previously explained and discussed in Chapter 2, the most regularly applied clinical diagnostic techniques for brain stroke detection are X-ray and MRI. They are however, neither fast nor portable (owing to pertinent dimensions of the devices), nor are they usable at rustic medical centres, or carried by FRS which are seen as essential for saving a person experiencing haemorrhagic stroke.

This chapter deals with the development of new techniques for medical imaging on the basis of the extremely broadband microwave signals rather than employing ionising radiations such as X-rays. It follows that, in response to all these limitations, MWI is one promising non-ionising and non-invasive alternative screening technology. MWI can be divided into radar techniques and MWT. MWT endeavors to reconstruct the dielectric property profile of the head by finding a solution to a relatively nonlinear and ill-posed inverse scattering problem [15],[16]. One of the detrimental points of MWT is the solution instability resulted from the complex mathematical formulations.In contrast, radar imaging entails finding a solution to a simpler problem of discovering the scattering map based on contrast amongst the dielectric properties. From the hardware point of view, a difficulty of MWI technology is how to conform more antennas together to cover the region of human tissues to be investigated [20]. The coupling medium can optimise antennas' penetration, however, with great complexity [21].

In addition, the antenna is required to be immersed in a 90 % glycerine-water mixture (used as a coupling medium) to achieve broadband operation and couple energy more efficiently into the head [21]. Therefore, as the consequence of these problems, a method is required to be performed, the approach deals with the HP. With the aim of lowering hardware complexity, in this work we have used an algorithm based on HP to localise strong scatterers (similar to radar imaging).

HP is a fast, accurate, and novel MWI method on the basis of the physical optics principles. In more detail, the HP based technique allows the detection of dielectric inhomogeneities in the frequency domain [22]. Hitherto, HP has been exploited for several cancer detection applications, notably for breast and skin cancer detection [23],[24]. The procedure permits to distinguish between different tissues, or different conditions of tissues, and to get a final image, which represents a homogeneity map of the dielectric properties (dielectric constant and/or conductivity). The interaction between microwave frequency ($\sim$ 1-40 GHz) electromagnetic signals and most materials is governed by two parameters, the material's complex dielectric permittivity ($\varepsilon_r = \varepsilon^{'}$ - j$\varepsilon^{''}$) and its conductivity σ (assuming the material is not magnetic).The components of the dielectric permittivity are functions of frequency, its real part $\varepsilon^{'}$ decreases monotonically from a stationary value at low frequencies towards low values at high frequencies.

In addition to the above explanation of the procedure, the proposed microstrip patch antenna and human head phantom including a brain haemorrhage phantom design and experimental setup have also been presented. The proposed antennas, positioned parallel to the y-axis of the reference system and omni-directional in the azimuth plane were used, after a proper check of S-parameters. It is important to point out that these microstrip patch antennas are only used to perform the measurements inside the anechoic chamber. As it was previously stated in the prior chapter, the multi-bistatic frequency-domain measurements have been performed to collect the transfer function (S21) between the two antennas, once inside the anechoic chamber and then for using with MWI device by applying the multi-layered phantom mimicking a human head to both measurements procedures. The frequency domain signals, which have been collected and described in the previous chapter, must be processed first.

The measurements data will then be used in MATLAB applying several pre-processing algorithms and assess their ability to remove artefacts. This will be completed through employing a set of measured data, using a measured transmission and receiving of signals, then applying the imaging algorithms to the results. These will be led by employing different positions and locations of the inclusion to ensure accuracy across a variety of situations. The images can be obtained through HP. In this study, we will assess the capability of the proposed procedure in detecting (only) haemorrhagic stroke through both simulations and measurements in an anechoic chamber and with MWI device. In the next sections, the HP's formulation will be presented in detail. Moreover, this chapter discusses the artefact removal methods as the signal pre-processing techniques. These artefact removal methods are using the data of simulation and measurements. The simulation data are gathered from simulation using CST software. The experimental measurements include two parts, measurements inside the anechoic chamber and

measurements through MWI device. Measurements through MWI device have been done representing UWB signals transmitted onto a round-bottom cylindrical head-mimicking phantom containing an inclusion having dielectric properties imitating a haemorrhagic stroke.

To have an accurate detection and find the location of the inclusion in the resulting images,five artefact removal methods are employed in measurements. More specifically, for measurements inside the anechoic chamber we only used the rotation subtraction artefact removal method. However, more methods have been applied to the measurements through MWI device, these include subtraction, rotation subtraction, local average subtraction, differential symmetric receiver type and summed symmetric differential type. We cannot possibly test the whole reviewed artefact removal methods through our entire procedures in this research. For simulation results, the subtraction and rotation subtraction artefact removal methods have been considered.

We are going to discuss the matter further, through the current chapter. The signal processing plays a vital role in obtaining diagnosis images with low noise. It is verified that all artefact removal procedures allow detection of the brain haemorrhagic stroke. However, the results are not presented in this chapter, following on from this initial exposition, all the simulation and measurement results, will be discussed and presented in the next chapter.

5.1 Imaging Procedure Using Huygens Principle

An ordinary radar system comprises a transmitter and a receiver. The transmitter transmits the signal and after that the object scatters this signal. Then, the receiver will receive and collect the scattering signal. For the researches which are on the basis of the electromagnetic scattering mechanism, all the definitions like transmitters and receivers will be disregarded and replaced. An incident wave is used instead of transmitter whilst the observation point is employed instead of receiver.

Addressing an imaging problem involves estimating the distribution of the field within a volume V based upon observations of the field on the surface of V, and this involves estimating the distribution of dielectric properties within the target volume. Next, with the aim of investigating general problems, a new method based on the HP is introduced. More in detail, the method deals with HP. Using HP to forward propagate removes the need to solve inverse problems and significantly reduces the computational overhead. Together with its simplicity, another benefit of HP is its capability of capturing the contrast. Moreover, HP allows all the information in the frequency domain to be utilised by combining the information from the individual frequencies to construct a consistent image [22]. It is concluded that this approach is capable to recognise

and classify the existence and position of substantial scatterers in a volume. Hence, the extension of this procedure to further realistic 3-D geometries would not be negligible. Validation of the techniques through both simulation and measurements has been performed and the results presented in the next chapter, illustrating the effectiveness of the methods. Potential application would not only be brain haemorrhagic stroke detection, but also breast and skin cancer detection [23],[24]. Moreover, it can be also effective for internal organ imaging and whole body imaging. It follows that, a mismatch, which is as a result of the difference amongst the properties of the two different media, appears in the district of transition amongst two different media. This mismatch allows the possibility for capturing the contrast, which will be employed to recognise, detect and localise the inhomogeneities. This statement is true on the basis of the HP that: "Each locus of a wave excites the local matter which re-radiates secondary wavelets, and all wavelets superpose to a new, resulting wave (the envelope of those wavelets), and so on" [94]. Figure 5.1 represents the description of the HP.

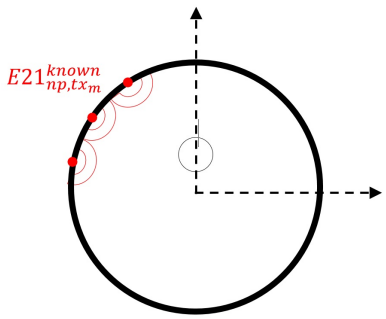

FIGURE 5.1: Pictorial description of the HP.

Hence, we investigate the opportunity to apply the HP employing $E^{\mathrm{rcstr}}_{\mathrm{HP,2D}}$ as the locus of a wave. To be exact, we consider what happens if HP is employed for reconstruction of the medium's internal field, employing the field simulated or measured on its external surface as the locus of a wave. So that, it is concluded that for exploiting such approach, we require calculating the field inside the medium as the superposition of the fields radiated by the N_{PT} receiving points in:

$$E^{\mathrm{rcstr}}_{\mathrm{HP,2D}}(\rho,\phi;\mathrm{tx}_m;f) = \Delta_s \sum_{np=1}^{N_{\mathrm{PT}}} S21_{np,\mathrm{tx}_m} G(k_1|\overrightarrow{\rho}_{np} - \overrightarrow{\rho}|) \tag{5.1}$$

where $\overrightarrow{\rho} \equiv (\rho,\phi)$ indicates the observation point; k_1 is the medium's wave number in the imaging zone; and Δ_s represents the spatial sampling. Also, subscript m indicates the transmitting

positions tx, and $np = 1, 2, \ldots, N_{\mathrm{PT}}$ the receiving positions. N_{PT} is the indexes to indicate the maximum receiving antennas. Moreover, in Equation (5.1) f represents the frequency.

S21 is the transmission coefficient which shows the transmission of waves from port 1 to port 2. In $E^{\mathrm{rcstr}}_{\mathrm{HP,2D}}$, the string rcstr indicates the "reconstructed" internal electric field, the string 2D (two dimensional) shows that my findings on the image reconstruction and artefact removal algorithms have been derived using a 2D configuration, and the string HP indicates that a HP based procedure is to be used.

Furthermore, it is noted that the reconstructed electric field depends on both the frequency and the illuminating source (as $E^{\mathrm{rcstr}}_{\mathrm{HP,2D}}$ is determined by the mentioned parameters). In Equation (5.1), the Green's function G for homogenous media is employed to forward propagate the field.

It is worth noting that the HP technique does not give the correct internal field, even while dealing with homogenous problems. The reason why the HP technique does not give the correct internal field is referring to the essence of the HP, which is formulated in far-field phenomena, i.e. it refers to the propagating wave front. However, an exact measure of the internal field is not required, only a capability to image the shape of the inclusion is desired. The desired outcome is therefore for the contrast between different tissues to be detected. To be exact, for having the capability to capture the far field, we just require having the knowledge of the E-field, as we have plane wave fronts. From the other point of view, for being capable of recovering and capturing the near field, we also require having the knowledge of the normal derivative of the E-field or the H-field.

However, for this particular circumstance, evaluating the internal field is not the purpose, actually the aim is to realise if the HP is able to capture the mismatch boundaries (which is called contrast) and subsequently detect the inclusion inside a volume. The ability to capture the contrast is due to the difference in properties amongst two different media. This has not been considered in Equation (5.1). Therefore, the reconstructed field displays a mismatch within the area of transition of the two media. The contrast provides an opportunity for a novel recognition and localisation approach. More in detail, let's assume that the external layer is irradiated from different sources (points) by a range of different frequencies; then the entire reconstructed fields would display the mismatch, and at all times it would be positioned in the area of transition of the two different media [95]. Therefore, by summing up incoherently all the solutions, i.e. the reconstructed fields, the inclusion would be recognised, detected, and localised.

In this thesis, we apply HP for the purpose of reconstructing the field. For the reconstruction procedure, by using the Green's function with the homogeneous medium, a mismatch will appear once passing from one medium to the other medium, and the ability to capture the mismatch boundaries signifies that this suggested procedure allows the detection of abnormalities.

Now, suppose that we employ N_f frequencies f_i, then the final image's intensity I is achieved through Equation (5.2), i.e. by incoherent addition of all the solutions [95]:

$$I(\rho,\phi) = \sum_{i=1}^{N_f} |E_{\mathrm{HP}}^{\mathrm{rcstr}}(\rho,\phi;\mathrm{tx}_m;f_i)|^2 \tag{5.2}$$

The intensity can be mapped by applying Equation (5.2), and the process repeated to map the internal field of a healthy human head (in simulation) or the head phantom (in measurements). The corresponding images will be presented in the results chapter. As it has been explained earlier in this section the imaging procedures with both simulation and experimental measurements data have been processed by using an imaging algorithm on the basis of the HP to generate all the images which have been presented in results chapter.

5.2 Artefact Removal Algorithms

Signal pre-processing techniques are usually used to reduce artefacts, which may be due to the direct fields and the fields reflected by the first layer. The undesirable points which appear in the created images are called artefacts and should be completely removed from the images. If the artefact is not removed successfully, it could mask strokes. The artefacts are usually brought about by the receiver which detects the input signal and the antenna reverberation, along with the interface between other areas which are not of interest (e.g. Skin-fat for breast imaging/possibly skin-skull for the head imaging) [25]. To remove the artefact, after investigating different methods of artefact removal, I decided to use five different methods of artefact removal.

1. Subtraction artefact removal method (used for the simulation and measurements data): In simulation, first we do the subtraction between the data of a healthy 3-D head model (Ella model) and the data of a head model with a brain haemorrhagic stroke. The same strategy has been used for the measurements through MWI device. More in detail, the first set of measurements is completed for the cylinder with no target (the "no target" scenario), and then the process is repeated for the cylinder which includes the 5 mm radius cylindrically shaped target (the "target" scenario).

2. Rotation subtraction artefact removal method (used for the simulation and measurements data of the anechoic chamber and the MWI device): the rotation subtraction between different transmitting positions.

3. Local average subtraction artefact removal method (used only for the measurements data obtained through MWI device). In this approach of artefact removal, we endeavour to remove the artefact with considering the average values of the recorded complex S21. The local average subtraction method will be considered for each triplet individually.

4. Differential symmetric receiver type (used only for the measurements data obtained through MWI device). In the differential symmetric receiver type method, artefact is removed by performing the subtraction between each receiver value from its symmetrically opposite receiver.

5. Summed symmetric differential (used only for the measurements data obtained through MWI device). The similarity in shape and density of the brain could be utilised to provide an artefact removal method by summing a differential matrix.

The methods of artefact removal used in this work were basically derived from the literature of references [23],[77],[96],[97]. It should be highlighted that the MWI device is able to provide the measured data from 5 different positions of the antennas. The results are then generated after using the imaging algorithm, through the different artefact removal techniques, separately for each group of antennas positions. The final image, which will be shown and discussed in the next chapter, is formed from these 5 images (a combination of 5 images). Before proceeding to perform the artefact removal methods, here, there is a need to briefly explain the results and data which will be received from the MWI device. This will later be used as the initial data for artefact removal procedures. Measurements have been performed by recording the complex S21 in a multi-bistatic fashion, as stated before. For experimental measurements using MWI device, the matrix is prepared by the received recorded complex S21. It comprises 1101 discrete frequencies f which are measured at 80 observation points, here denoted with ϕ, giving matrix A_1 in:

$$A_1 = \begin{bmatrix} f_1\phi_1 & \dots & f_{1101}\phi_1 \\ \vdots & \ddots & \vdots \\ f_1\phi_{80} & \dots & f_{1101}\phi_{80} \end{bmatrix} \tag{5.3}$$

Matrix A_1 which is collected from the recorded complex S21 for known position of the inclusion, will later be employed as the initial data for artefact removal procedures (measurements through MWI device). The results from other positions of the inclusion are positioned in matrices A_2, A_3, and A_4 in a similar fashion. Inclusion positions include 0°, 90°, 180° and 270° for measurement trough MWI device. The employment of different sets of these positions

differs in various artefact removal methods and procedures. Hence, the set of these positions applied to each artefact removal method will be specified in its section.

5.2.1 Artefact Removal Algorithms: Subtraction

The first proposed method of artefact removal can be expressed as 'Subtraction artefact removal'. This method has been applied to obtain simulation results with CST software (with the inclusion positioned at 0°, 5° , 40° , and 45°) and the measurements results through MWI device (with the inclusion positioned at 0°, 90°, 180°, 270°).

- **Simulation Using CST Software and Measurements through MWI Device**

In this method, the artefact removal has been achieved by subtracting the electric field (calculated on the circular grid of points with radius of 110 mm (ρ=110 mm) and 6° phi sampling (ϕ=6°) just outside the head) for Ella with a stroke and for Ella without stroke. The results of the subtraction artefact removal method which has been discussed in the current chapter, is called "Ideal" image. Using this name for the corresponding image is due to the fact that the subtraction method can only be applied to the simulation data, in practice. An "Ideal" image would be generated to prove the concept of the technology. This would mean that the 'Ideal' image can be used as a reference for comparison with the resulting image from using the rotation subtraction method and other artefact removal methods. We will further use this method in Section 5.3. In this approach of artefact removal, with subtracting the electric field of healthy human head model, Ella model (in simulation) from the electric field of a human head model with an emulated brain haemorrhage (in simulation), a matrix which can only indicates the differences will be left. Then, once imaged, the subtraction artefact removal method makes the opportunity available for detection of the emulated brain haemorrhagic stroke. The discussed procedure is described mathematically with "$\mathrm{S21}_{np,\mathrm{tx1}}^{\mathrm{rcstr,withstroke}} - \mathrm{S21}_{np,\mathrm{tx1}}^{\mathrm{rcstr,withoutstroke}}$,,". This expression can be used in Equation (5.1).

A similar procedure to the above mentioned method of artefact removal has been used in references [25],[77]. In reference [77], the authors apply a similar approach to the measured data for a cylindrical object with an inclusion inside and a cylindrical object without any inclusion. It indicates that the image of an inclusion will be achieved as a result of mapping the difference in intensity. The same strategy is applied to the measured data through MWI device. More in detail, two sets of experimental measurements are performed for imaging scenario; First the "no target" scenario, for a phantom with no target, secondly the "target" scenario, for the repeated procedure using a phantom with a millimetric cylindrically shaped inclusion to emulate a haemorrhagic brain stroke. The inclusion will be indicated in the image obtained

through Equation 5.2, by subtracting the recorded S21 of the "no target" scenario from that of the "target" scenario "$\mathrm{S21}^{\mathrm{rcstr,target}}_{np,\mathrm{tx1}} - \mathrm{S21}^{\mathrm{rcstr,notarget}}_{np,\mathrm{tx1}}$".This expression can be used in Equation (5.1).

It is important to point out that, for the purposes of real scenario, there is no possibility of applying the subtraction artefact removal method to medical imaging. We use this method for the simulation data to show the strong feasibility of detecting the brain haemorrhage in an ideal way; this will be presented and verified in the results chapter by proving the corresponding images and parameters.

Also, one of the efforts of the current work is to achieve an algorithm which generates as close a match as possible to the ideal result. Since with applying different artefact removal algorithms, the resulting image has potential to vary. It should be noted that there is no possibility to test the algorithm in contradiction of the imaging methods where the ideal response is not calculated or known (i.e. measured data from a real human head with a brain stroke). Hence, in clinical trials or new research the subtraction artefact removal method cannot be helpful and effective. In [25], Elahi et al. introduce, define, test and provide a comparison between 7 different artefacts removal methods specifically in the detection of the breast cancer. We have applied different artefact removal methods with the data from the simulations and measurements in order to find the best method of artefact removal specifically for the detection of the brain haemorrhagic stroke.

5.2.2 Artefact Removal Algorithms: Rotation Subtraction

Another proposed method of artefact removal can be expressed as 'rotation subtraction artefact removal'. The initial idea of this method of artefact removal has been adopted from references [95],[97], in which, Klemm, et al. have offered the rotation subtraction artefact removal method for breast cancer detection by taking two radar measurements. The first set of the measurements has been taken, then after that, the measurement apparatus has been rotated on the horizontal plane and the second reading was taken. After finishing the mentioned procedure, the results from the second set of the reading is subtracted from the first set. Moreover in [97], the authors described four methods with giving the main points, in order to draw a comparison between the achieved results using these four artefact removal algorithms. They proved that this method has been considered as an effective and successful method for breast cancer detection.

On the contrary, in [25], it was concluded that the average and rotation subtraction methods cannot be considered as the successful algorithms, whilst there is variation between the channels. Anyhow, they concluded that filter based approaches can be further robust to variation,

but the artefact window should be calculated or known, in advance. And then again, there will be no possibility to test the algorithm against the imaging methods where the ideal response is not calculated or known. Based on our conducted study into the effectiveness of the rotation subtraction method in detecting the object (e.g. the haemorrhage/ cancer/tumour) [97], and relying on the results of the tests which will be presented in the next chapter, such method offers a good detection of the brain stroke (for both simulation and measurements data).

In this thesis, rotation subtraction artefact removal method has been applied to obtain simulation results with CST software (with the inclusion positioned at 0°, 45°), the measurement results inside the anechoic chamber (with the inclusion positioned at 0°, 90°, 180°, 270°) and the measurement results through MWI device (with the inclusion positioned at 0°, 90°, 180°, and 270°).

- **Simulation Using CST Software and Measurements inside Anechoic Chamber**

As we have also explained at the beginning of the current section, in the rotation subtraction method, artefact is removed by performing the subtraction between two sets of data obtained by slightly rotating the position of the transmitting antenna around the object. Referring to the notation used in this section, we proceed by considering the expression "$\mathrm{S21}_{np,\mathrm{tx}_1} - \mathrm{S21}_{np,\mathrm{tx}_2}$" where tx_1 and tx_2 represent the two closest transmitting positions. This expression can be used in Equation (5.1), such that:

$$E^{\mathrm{rcstr}}_{\mathrm{HP,2D}}(\rho,\phi;\mathrm{tx}_m;f) = \Delta_s \sum_{np=1}^{N_{\mathrm{PT}}} \Big((\mathrm{S21}_{np,\mathrm{tx}_1} - \mathrm{S21}_{np,\mathrm{tx}_2}) \Big) G(k_1 |\overrightarrow{\rho}_{np} - \overrightarrow{\rho}|) \tag{5.4}$$

Subsequently, I is achieved through Equation (5.2). It should be emphasised that the rotation subtraction artefact removal method may be applied to both simulation and measurements. The mentioned expression is defined to explain the rotation subtraction artefact removal method for the simulation results using CST software and the results of measurements inside the anechoic chamber.

- **Measurements through MWI Device**

Following the Sections 4.4.2 and 5.1 for the measurements with the MWI device, suppose that rx have took a rotational path for measuring the received signal at the observation points $\overrightarrow{\rho} \equiv (\rho, \phi)$ displaced along a circular surface having radius a_0, the received signals are called $\mathrm{S21}_{np,\mathrm{tx}_m}$ $(a_0; \phi_{np}; \mathrm{tx}_m; f)$ with the receiving positions np=1, 2, ..., 80, m transmitting positions tx equal to m=1, 2, ..., 15, and f represents the frequency. Also, here, we apply the subtraction between S21 obtained by employing two measurements corresponding to the triplet

of the same section. Therefore, the rotation subtraction strategy is described mathematically through "$\mathrm{S21}_{np,\mathrm{t}x_m} - \mathrm{S21}_{np,\mathrm{t}x_{m+2}}$".

The current procedure has been implemented by subtracting the transmitting position m from the transmitting position $m+2$, with m and $m+2$ corresponding to the same triplet. This expression can be used in Equation (5.1), such that (N_{PT} is the number of the receiving points):

$$E^{\mathrm{rcstr}}_{\mathrm{HP,2D}}(\rho,\phi;\mathrm{tx}_m-\mathrm{tx}_{m+2};f) = \Delta_s \sum_{np=1}^{N_{\mathrm{PT}}} \left((\mathrm{S21}_{np,\mathrm{tx}_m} - \mathrm{S21}_{np,\mathrm{tx}_{m+2}}) \right) G(k_1|\overrightarrow{\rho}_{np} - \overrightarrow{\rho}|) \quad (5.5)$$

where $\overrightarrow{\rho} \equiv (\rho,\phi)$ indicates the observation point; k_1 is the medium's wave number in the imaging zone; and Δ_s represents the spatial sampling. In Equation (5.5), the receiving positions $np = 1,2,\ldots,80$, and m transmitting positions tx equal to $m = 1,2,\ldots,15$, and f represents the frequency. The intensity of the final images for the measurements results is provided through adding different images related to different transmitting triplets, each one obtained through non-coherent summation of all frequency contributions. Mathematically speaking, generating the combined image of 5 transmitting position triplets can be described in Equation (5.6) (N_f being the number of frequency samples):

$$I(\rho,\phi) = \sum_{m=1}^{5} I(\rho,\phi;\mathrm{tx}_{3m-2}-\mathrm{tx}_{3m};f_i) = \sum_{m=1}^{5}\sum_{i=1}^{N_f} |E^{\mathrm{rcstr}}_{\mathrm{HP,2D}}(\rho,\phi;\mathrm{tx}_{3m-2}-\mathrm{tx}_{3m};f_i)|^2 \quad (5.6)$$

Superscript 5 indicates the number of 5 transmitting position triplets. The combined image of 5 transmitting position triplets can be generated through Equation (5.6).

5.2.3 Artefact Removal Algorithms: Local Average Subtraction

Another proposed method of artefact removal is named 'local average subtraction artefact removal'. The local average subtraction algorithm has been applied widely by researchers with successful results [25],[66],[96]. It should be noted that this method of artefact removal is considered to be applied only to the measurements results through MWI device, since it is not feasible to test the whole reviewed artefact removal methods through our entire procedures. Technically, local average subtraction artefact removal method may be applied to both simulation and measurements data. Here, the local average subtraction artefact removal method

has been applied to obtain the measurements results through MWI device (with the inclusion positioned at 0°, 90°, 180°, and 270°).

In this approach of artefact removal, we endeavour to remove successfully the artefact using the average values of the S21 received from the transmitting positions in a same triplet. Following the Section 5.1, for the measurements with the MWI device, suppose that rx have took a rotational path for measuring the received signal at the observation points $\overrightarrow{\rho} \equiv (\rho, \phi)$ displaced along a circular surface having radius a_0, the received signals are called $\mathrm{S21}_{np,\mathrm{tx}_m}$ $(a_0; \phi_{np}; \mathrm{tx}_m; f)$ with the receiving positions $np = 1, 2, \ldots, 80, m$ transmitting positions tx equal to $m = 1, 2, \ldots, 15$, and f representing the frequency. Then the mean of received signals are calculated, i.e. $avg\{\mathrm{S21}_{np,\mathrm{tx}_m}\}$. This can be done in MATLAB by using the MATLAB mean function across the third dimension. Next, we apply the subtraction between received signals $\mathrm{S21}_{np,\mathrm{tx}_m}$ from one transmitting position and the mean of received signals of the transmitting positions in a same triplet $avg\{\mathrm{S21}_{np,\mathrm{tx}_m}\}$. Therefore, the local average subtraction strategy is described mathematically through:"$\mathrm{S21}_{np,\mathrm{tx}_m} - ave\{\mathrm{S21}_{np,\mathrm{tx}_m}\}$".

The current procedure has been implemented by subtracting the received signals $\mathrm{S21}_{np,\mathrm{tx}_m}$ and the mean of received signals $avg\{\mathrm{S21}_{np,\mathrm{tx}_m}\}$ correspond to the same triplet. The expression can be used in Equation (5.1).

Mathematically speaking, $E^{\mathrm{rcstr}}_{\mathrm{HP,2D}}$ is defined with considering multiple transmitting sources, through the following Equation:

$$E^{\mathrm{rcstr}}_{\mathrm{HP,2D}}(\rho, \phi; \mathrm{tx}_m; f) = \Delta_s \sum_{np=1}^{N_{\mathrm{PT}}} \left((\mathrm{S21}_{np,\mathrm{tx}_m} - avg\{\mathrm{S21}_{np,\mathrm{tx}_m}\}) \right) G(k_1 |\overrightarrow{\rho}_{np} - \overrightarrow{\rho}|) \quad (5.7)$$

where $avg\{\mathrm{S21}_{np,\mathrm{tx}_m}\}$ shows the average of the signals achieved from 5 different transmitter positions. The average matrix is formed from the average of the $\mathrm{S21}_{np,\mathrm{tx}_m}$. Equation (5.7) explains the local average subtraction method. The local average subtraction method represents just one method of obtaining an image of the inclusion for measurements through MWI device. Several methods have been proposed which replace the average matrix with an alternative, such as the measurements using differential symmetric receiver type by applying a differential method of obtaining the resulting image, as is the case in [66],[96],[98]. For measurements using local average subtraction method, supposing we use N_f frequencies f_i, then the intensity of the final image I can be obtained using Equation (5.2).

5.2.4 Artefact Removal Algorithms: Differential Symmetric Receiver Type

In fact, the medium we eventually will be using (the brain) has a natural symmetry. By exploiting the (eventual) object symmetry, it may be possible to apply another artefact removal method using the difference between the receivers placed symmetrically opposite. This method is initially derived from the literature of reference [98] used by Mustafa et al. In the differential symmetric receiver type method, artefact is removed by performing the subtraction between each receiver value from its symmetrically opposite receiver. Mathematically speaking, the artefact removal can be obtained through differential symmetric receiver type method using the following Equation:

$$S(\rho, \phi; N_{\text{TX}}) = \text{S21}_{np,\text{tx}_m}(\rho, \phi; N_{\text{TX}}) - \text{S21}_{np,\text{tx}_m}(\rho, N_{\text{PT}} + 2 - \phi; N_{\text{TX}}) \tag{5.8}$$

$$\text{for} \quad \phi = 1 \quad \text{to} \quad N_{\text{PT}} \quad \text{with} \quad N_{\text{PT}} + 2 - \phi = \tfrac{N_{\text{PT}}}{2} + 1 \quad \text{for} \quad \phi = 1 \quad \text{and}$$

$$\tfrac{N_{\text{PT}}}{2} + 1 = 1 \quad \text{for} \quad \phi = 1 \quad \text{for} \quad \phi = \tfrac{N_{\text{PT}}}{2} + 1$$

where N_{PT} is the maximum number of receiving antennas, N_{TX} is an index to indicate the maximum transmitting positions, and $\text{S21}(np, \text{tx}_m)$ is the original recorded complex S21. This causes a Differential (Symmetric Receiver Type) matrix S. The local average subtraction or rotation subtraction method is then applied to such matrix.

Here, the differential symmetric receiver type artefact removal method has been applied to obtain the measurements results through MWI device (with the inclusion positioned at 0°, 90°, 180°, 270°). It should be noted that this method of artefact removal is considered to be applied to the measurements results through MWI device, since it is not feasible to test the whole reviewed artefact removal methods through our entire procedures. Technically, differential symmetric receiver type artefact removal method may be applied to both simulation and measurements.

5.2.5 Artefact Removal Algorithms: Summed Symmetric Differential

The symmetric differential method above relies on the natural symmetry of some objects, such as the brain, across the left and right halves. The results of symmetric differential method will be presented in the results chapter. From the results for symmetric differential method above, it is worthwhile pointing out that the images which have used the symmetric method may contain mirrored artefact. If a method could be identified to eliminate or reduce the mirrored section, the method could be successful. The ellipsoidal shape of the human head has a distinct left-right

line of symmetry. The front-back sections of the brain also contain similar densities of tissue. Whilst not absolutely symmetrical, the resemblance in shape and density could be utilised to offer an artefact removal method by summing a differential matrix formed from the left-right differential and a second matrix formed from a front-back differential. Hence, this can provide a more intense peak at the area of inclusion, and subsequently the mirrored artefact will have a reduced intensity. A differential matrix S is constructed the same as before by applying Equation (5.8).

A second matrix R is constructed across the front-back receivers and is defined as follows:

$$R(\rho,\phi;N_{\text{TX}}) = \text{S21}_{np,\text{tx}_m}(\rho,\phi;N_{\text{TX}}) - \text{S21}_{np,\text{tx}_m}(\rho,\frac{N_{\text{PT}}}{2}+2-\phi;N_{\text{TX}}) \tag{5.9}$$

$$\text{for} \quad \phi = 1 \quad \text{to} \quad \tfrac{N_{\text{PT}}}{2}+1$$

$$\text{with} \quad \tfrac{N_{\text{PT}}}{2}+2-\phi = \tfrac{3N_{\text{PT}}}{4}+1 \quad \text{for} \quad \phi = \tfrac{N_{\text{PT}}}{4}+1$$

$$R(\rho,\phi;N_{TX}) = \text{S21}_{np,\text{tx}_m}(\rho,\phi;N_{\text{TX}}) - \text{S21}_{np,\text{tx}_m}(\rho,\frac{3N_{\text{PT}}}{2}+2-\phi;N_{\text{TX}}) \tag{5.10}$$

$$\text{for} \quad \phi = \tfrac{N_{\text{PT}}}{2}+2 \quad \text{to} \quad N_{\text{PT}}$$

$$\text{with} \quad \tfrac{3N_{\text{PT}}}{2}+2-\phi = \tfrac{N_{\text{PT}}}{4}+1 \quad \text{for} \quad \phi = \tfrac{3N_{\text{PT}}}{4}+1$$

Then the combined matrix C is composed of summing matrices S and R and used as a differential (summed symmetric receiver type) matrix. The local average subtraction or rotation subtraction method is then applied to such matrix. Here, the summed symmetric differential artefact removal method has been applied to obtain the measurement results through MWI device (with the inclusion positioned at 0°, 90°, 180°, and 270°). It should be noted that this method of artefact removal is considered to be applied to the measurement results through MWI device. Technically, summed symmetric differential artefact removal method may be applied to both simulation and measurements.

5.3 Image Quantification

Imaging performance has been investigated through image quantification. As a portion of this research, the calculation of a dedicated parameter will require to be constructed to assess the stroke detection capability and to allow performing a quantification of detection accuracy. It

has been studied through image quantification to evaluate the performance of the reconstruction algorithms. In order to quantify the imaging's detection capabilities and compare the proposed artefact removal methods, constructing a quantifiable measurement system for comparing images is of vital importance in such procedures. There are several metrics using for quantifying the stroke detection capability. Based on two scenarios discussed in this research (the " no target" scenario and the "target" scenario), we introduced here the calculation of five dedicated parameters, which allow to perform a quantification of detection accuracy. These metrics are categorised into those that rely on a reference image called "Ideal" image and those independent of that. The metrics for detection accuracy are comprised of Area Difference index, Polyshape Construction, Centroid Difference, Signal-to-Noise Ratio (SNR), Signal-to-Clutter ratio (S/C) and Structural Similarity Index Metric (SSIM). Amongst all SSIM, ArD, and CD depend on "Ideal" image. For the purposes of this experiment, an "Ideal" image has been presented as shown in Figure 5.2. Further details with reference to these metrics are explained below. Figure 5.3 represents the combination "Ideal" image of 5 transmitting position triplets.

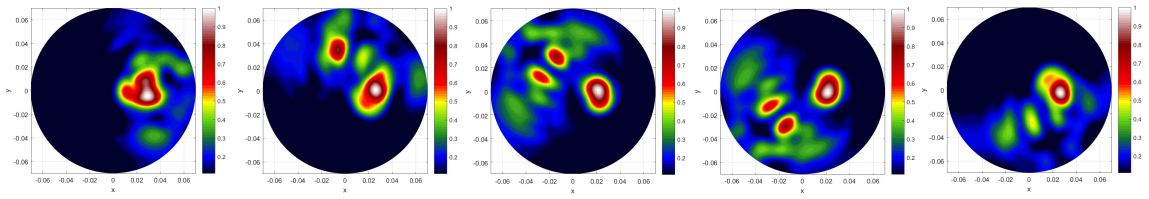

FIGURE 5.2: Images from each of the 5 transmitter groups using "Ideal" subtraction method.

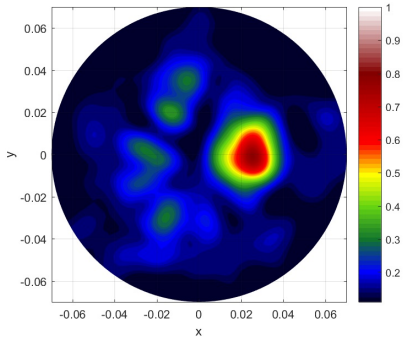

FIGURE 5.3: The combination "Ideal" image of 5 transmitting position triplets.

Loizou et al. [99] created a novel imaging toolbox using MATLAB that has been applied to draw a comparison of ultrasound imaging of the carotid artery. Although the main focus of the authors was on Despeckle filtering which fall outside the scope of this work. Loizou proposed

several metrics that offered in a toolbox which is able to be applied for assessing the quality of the images. The metrics for detection accuracy are comprised of Mean Square Error, Geometric Average Error, and Average Difference amongst others for generating a Unique Image Index. It considered a value from 1 to 0 to provide a single quantifiable result for the image quality and the calculation has been done by using all the above metrics.

Since the images may contain some clutter even following artefact removal procedures, it is appropriate to introduce a parameter in order to quantify and compare the performance in detection when using different artefact removal algorithms. Zamani and Abbosh [96] compare several clutter rejection techniques for imaging the head. A differential method involving using the difference between neighbouring receivers and a similar approach using symmetric receivers achieve good results. To assess the quality of the images, Zamani applies the SNR and distance to centre. These metrics assess the accuracy and strength of the results and would be useful to use in comparisons within this project. These will be described in more detail in the next section and the equations will be explained mathematically. As a portion of this study, the calculation of the dedicated parameters will require to be constructed to assess the stroke detection capability and to allow performing a quantification of detection accuracy. For this purpose, the parameters are as follows:

- Polyshape Construction
- Area Difference (ArD)
- Centroid Difference (CD)
- Signal-to-Noise Ratio (SNR)
- Structural Similarity Index Metric (SSIM)
- Signal-to-clutter ratio (S/C)

It is worth pointing out that all metrics are used to provide a reliable comparison between all artefact removal methods. The results will be presented in the next chapter.

5.3.1 Polyshape Construction

When evaluating an image, the inclusion in the Ideal Images is approximately made up of the normalised values which are over 75% of the maximum value. To evaluate the shape of the inclusion, here, a threshold of 0.75 has been set on the normalised image. We can therefore

set 0.75 as a threshold and assess the shape of the inclusion and how accurately it is represented. This would mean that the image is adjusted through expanding from 0.75 to 1 of the values more than 0.75 and enforcing to 0 the values less than 0.75. By applying MATLAB's `polyboundary` and `polyshape` functions, the resulting shape can be achieved [100].

5.3.2 Area Difference

This metric is related to the comparison between the size of the target area for an "Ideal" image and the size of the target area in the test image. Having set the above mentioned threshold and defined two areas as the "target" area and the "background" area, a comparison can then be drawn between the size of the target area for an "Ideal" image and the size of the target area in the test image. This is done by calculating the different between the size of the target area for an "Ideal" image and test image. This is then divided by the total number of values to give the fraction of values that differ. The values obtained from this calculation are not absolute numbers and used to indicate to what extent the "Ideal" image is similar to the images obtained through different artefact removal methods. Mathematically speaking, area difference is described in Equation (5.11).

$$\text{Area Difference} = \left| \frac{N_{\text{Experiment(test)}} - N_{\text{Ideal}}}{\text{Image Matrix Size}} \right| \tag{5.11}$$

In above, $N_{\text{Experiment(test)}}$ and N_{Ideal} are the number of values over the target threshold in the experiment image and "Ideal" image, respectively. It is worthwhile pointing out that this is a useful measure of the precision of the target area, but not the accuracy. For this another metric is required.

5.3.3 Centroid Difference (CD)

Referring to the above image quantification method to quantify the imaging's detection capabilities and test the accuracy of the image at locating an inclusion, MATLAB's `polyboundary` and `polyshape` functions were combined with MATLAB's centroid function. Evaluation of detection accuracy carries out by assessing the Euclidean difference between the centroid of an "Ideal" image polyshape and the test image. This is used to find the centre of a shape using the mathematics principles of centre of mass. Assuming the shape has a constant density; the centroid function will take a polyshape and find the exact centre of mass. Using Cartesian coordinates, if the centroid of the "Ideal" image is positioned at $\mathrm{i} = (\mathrm{i}_1, \mathrm{i}_2)$ and the centroid of the test image is positioned at $\mathrm{t} = (\mathrm{t}_1, \mathrm{t}_2)$, the distance, $\mathrm{d}(\mathrm{i}, \mathrm{t})$, is calculated using the Pythagorean

formula in 5.12. This is done using the MATLAB `pdist` function [100].

$$\mathrm{d(i,t)} = \sqrt{(\mathrm{t_1} - \mathrm{i_1})^2 + (\mathrm{t_2} - \mathrm{i_2})^2} \tag{5.12}$$

5.3.4 Signal-to-Noise Ratio

Another useful metric for quantifying the imaging's detection capabilities is the SNR. This method of image quantification has basically derived from the literature of reference [96]. The SNR is a useful metric in determining how clear any detected inclusion is by providing an assessment of the ratio between the background noise and the desired signal. It is calculated in dBs. To calculate SNR, the above threshold is used to calculate the Polyshape and SNR calculations performed based on this result. This defines the target area and background area. The calculation of the SNR are performed on the basis of this result and the Equation such that:

$$\text{SNR} = 10\log_{10}\left(\frac{Q_t - Q_b}{D_b}\right)\text{dB} \tag{5.13}$$

In above, Q_t and Q_b are the mean values of the detected target and background regions, respectively, and D_b is the standard deviation of the background.

5.3.5 Structural Similarity Index Metric

Another metric which allows performing a quantification of detection accuracy is the SSIM. This is used extensively in imaging comparison. The SSIM is an image quality metric which gives a value between 0 and 1 which indicates the similarity between two images (with 1 meaning the images are identical). We proceed by writing the following Equation:

$$\text{SSIM} = \frac{(2 \times \bar{x} \times \bar{y} + C_1)(2 \times \sigma_{xy} + C_2)}{(\sigma_x^2 + \sigma_y^2 + C_2)(\bar{x}^2 + \bar{y}^2 + C_1)} \tag{5.14}$$

Regarding the above Equation, x represents the reference image, y represents the test image, $\bar{x}$ and $\bar{y}$ are the corresponding means, σ_x and σ_y represent the corresponding variances, σ_{xy} is the covariance of the reference and test images. In above equation, C_1, and C_2 are small constants. SSIM could be calculated on the basis of two input images using the `ssim` function in MATLAB [101]. This will output both a value and a monochrome mapping which is a useful visual assessment of the quality of the image.

5.3.6 Signal-to-Clutter Ratio

The last reliable metric which is introduced and calculated in this thesis to quantify the imaging's detection capabilities, is Signal-to-clutter (S/C) ratio. Clutter comes from undesired scatter from objects within the radar beam that are not targets, and has been characterised by several distributions. To evaluate the performance of the imaging algorithm's in this project, a quantitative metric is used, which is S/C ratio. As the resulting images might possibly contain some clutter even after applying artefact removal procedures, it is applicable to present a parameter with the intention of quantifying and comparing the performance in detection when applying different artefact removal algorithms. Typically the S/C ratio has been described as the ratio of the maximum brain haemorrhage or tumour response to the maximum clutter response. Here, S/C is described as the ratio between maximum intensity evaluated in the district of the lesion divided by the maximum intensity outside the district of the lesion [102]. The S/C ratio is evaluated for each image, considering rotation subtraction and subtraction (resulting in the generated "Ideal" image) artefact removal methods. This metric evaluates the accuracy and strength of the results and would be highly effective to employ in comparisons in this study. The tables representing the corresponding values of the S/C have been offered considering all the artefact removal methods, in the results chapter.

5.4 Summary

Our team in LSBU have adapted the methods used to detect several cancers (e.g. breast, skin cancer). In this specific project, a promising research applying the technology for the detection of brain haemorrhage has been produced. The technology relies on detecting the contrast at the interface between two tissues with differing dielectric properties. MWI approach is a promising approach of the brain haemorrhage detection on the basis of the huge contrast in electrical parameters between the brain haemorrhagic stroke tissue and the surrounding healthy tissues. Therefore, several different procedures have been suggested for brain stroke detection applying the MWI techniques. The suggested procedure allows a possibility to detect and localise the brain haemorrhage both in simulation and experimental measurements. We consider what happens if HP is employed for reconstruction of the medium's internal field, employing the field simulated or measured on its external surface as the locus of a wave. HP does not give the correct internal field. There is a difference in the properties between the two different media. The reconstructed field displays a mismatch at the region of transition between the two different media. Hence, to enable imaging it is just necessary to map the mismatch. This can be done

by illuminating the object (here the human head phantom) from different points and applying a range of different frequencies. The mismatch would be presented in all the results and located at the point of transition between the two media. Therefore, an image could be achieved by summing all the solutions. A theory has been described which emphasises on this definition that with moving the transmitting sources to the different positions, better results can be achieved that would eliminate unwanted artefact. In addition to this method, four more different methods have been used to remove the artefact. These five methods are comprised of the subtraction, rotation subtraction, local average subtraction, differential symmetric receiver type, and summed symmetric differential method of artefact removal. All were described in detail, through this chapter.

Practically, the subtraction method can only be applied to the simulation data, although other reviewed artefact removal methods may be applied to both simulation and measurements data. However, the "Ideal" image is obtained by using subtraction artefact removal method and is performed as a reference for the comparison with the resulting images from using other artefact removal methods. At the end of this chapter, several metrics for performing the image quantification were proposed. For this purpose, we introduced here different metrics comprising Area Difference, Polyshape Construction, Centroid Difference, Signal-to-Noise Ratio, Structural Similarity Index Metric, and signal-to-clutter ratio. These allow performing a quantification of detection accuracy. All the metrics have been calculated for the measurements through MWI device. The S/C has also been calculated for simulation with CST software and both measurements results (measurements inside anechoic chamber and measurements through MWI device).

Chapter 6

Microwave Imaging for Brain Haemorrhage Detection

The current chapter includes the construction of the microwave images for the multi-layered brain phantom employing the received signals. Microwave images are generated on the basis of the simulation and experimental measurements results. A multi-layered head phantom which comprises of a brain haemorrhage is simulated using CST microwave software and measured applying the microstrip patch antenna, inside the anechoic chamber. For the simulation part, the microstrip patch antenna is applied to the head phantom and S11 has been previously performed and discussed. Both the simulated and measured S11 in front of human head and in free space have been presented and discussed earlier in Chapters 3 and 4. Furthermore, the experimental measurements are consisted of the measurements inside the anechoic chamber and measurements with MWI device, as explained in Chapters 4 and 5. First, the microstrip patch antenna has been used with the first head phantom, to gather the transfer function S21 between the two proposed antennas through a VNA. Then, a custom designed mould for head phantom has been fabricated in order to be employed with MWI device. It should be noted that the fabrication process for the phantom of haemorrhagic brain stroke is completely similar in both human head phantoms. The only difference is the moulds which has been designed and applied. Next, the measurements have been performed by recording the complex S21 in a multi-bistatic fashion, using second proposed head phantom in MWI device. The images through measurements will be presented and discussed in this chapter.

An algorithm based on the HP is used to localise strong scatterers, as explained in Chapter 5. We consider what happens if HP is employed for reconstruction of the medium's internal field, employing the field measured on its external surface as the locus of a wave. Then, with the aim of reducing the artefacts (which may be due to the direct fields and the fields reflected by the first layer), signal pre-processing techniques are used. To remove the artefact, we use five different methods, as following:

I. Subtraction artefact removal method (Used for the simulation and measurements data): In CST simulation, first the subtraction is perfumed between the data of a healthy 3-D head model (Ella model) and the data of a head model with a brain haemorrhagic stroke (with the inclusion positioned at 0°, 5°, 40°, and 45°). The same strategy has been used for the measurements through MWI device (with the inclusion positioned at 0°, 90°, 180°, 270°). More in detail, the first set of measurements is completed for the cylinder with no target (the "no target" scenario), and then the process is repeated for the cylinder which includes the 5 mm radius cylindrically shaped target (the "target" scenario).

II. Rotation subtraction artefact removal method (Used for the CST simulation (with the inclusion positioned at 0°, and 45°) and measurements data inside the anechoic chamber (with the inclusion positioned at 0°, 90°, 180°, and 270°) and the MWI device (with the inclusion positioned at 0°, 90°, 180° and 270°)): the rotation subtraction between different transmitting positions.

III. Local average subtraction artefact removal method (Using only for the measurements data obtained through MWI device (with the inclusion positioned at 0°, 90°, 180° and 270°)). In this approach of artefact removal, we endeavour to remove the artefact with considering the average values of the recorded complex S21. The local average subtraction method will be considered for each triplet individually.

IV. Differential symmetric receiver type (Used only for the measurements data obtained through MWI device (with the inclusion positioned at 0°, 90°, 180° and 270°)). In the differential symmetric receiver type method, artefact is removed by performing the subtraction between each receiver value from its symmetrically opposite receiver.

V. Summed symmetric differential (used only for the measurements data obtained through MWI device (with the inclusion positioned at 0°, 90°, 180° and 270°)). The similarity in shape and density of the brain could be utilised to provide an artefact removal method by summing a differential matrix.

It should be emphasised that in a real scenario the subtraction artefact removal method may only be applied to simulation data, whilst other artefact removal methods can be applied to both simulation and measurements data. In clinical trials, there is no possibility of having a human head with stroke and the same human head without stroke (for subtracting them from each other). We use this method for the simulation data to show the strong feasibility of detecting the brain haemorrhage in an ideal way. This "Ideal" image image is performed as a reference

for the comparison with the resulting image from other artefact removal methods. As a portion of this study, the calculation of the dedicated parameters will require to be constructed to assess the stroke detection capability and to allow performing a quantification of detection accuracy. These metrics evaluate the accuracy and strength of the results and would be highly effective to employ in comparisons in this study. For this purpose, the parameters are as follows:

- Polyshape Construction
- Area Difference (ArD)
- Centroid Difference (CD)
- Signal-to-Noise Ratio (SNR)
- Structural Similarity Index Metric (SSIM)
- Signal-to-clutter ratio (S/C)

These parameters have been discussed through the previous chapter. It is worth pointing out that all the metrics are calculated for each image, considering different artefact removal methods. To lead to a better understanding of this project, the results are mainly divided into three principal parts. These are comprised of the results and imaging through simulation using CST software, and the phantom imaging which is divided to two parts of results inside the anechoic chamber and through MWI device.

In the current chapter, the imaging results on the basis of the received signals are generated. By using the simulation and experimental measurements data (explained in Chapters 3 and 4), the HP procedure and the appropriate artefact removal methods (discussed in Chapter 5), the conclusion was drawn that a brain haemorrhagic has been successfully detected using the CST simulation data (in four different positions of 0°, 5°, 40°, and 45°). It should be emphasised that for simulation data only the subtraction artifact removal and rotation subtraction artifact removal methods have been applied. For the experimental measurements (inside the anechoic chamber), only the rotation subtraction artifact removal method has been used to detect the target positioned at four doublets (0° and 5°; 90° and 95°; 180° and 185°; 270° and 275°). Moreover, the brain haemorrhagic has been successfully detected in different positions of 0°, 90°, 180° and 270°, through the experimental measurements data using MWI device and the rotation subtraction artefact removal method. It should be recalled that other five reviewed artefact removal methods have been applied to obtain the measurements results through MWI device with the inclusion positioned at 0°, 90°, 180° and 270°. Thus, the proposed procedure has been validated through three processes.

6.1 Imaging through Simulations

The antenna design, simulation in CST Microwave studio has been presented and discussed in Chapter 3. A simulated microstrip patch antenna using fractal ground plane technique moves to scan the human head model (Ella model).

The corresponding initial data and results which are used in this section are explained and derived from Section 4.3.2. The simulation has been done for two different situations, i.e. first with subtraction artefact removal method; for a healthy head model which is mentioned before as Ella model (the "no target" scenario) and a head model with a spherical emulated haemorrhagic stroke (the "target" scenario), and secondly with rotation subtraction artefact removal method for four different positions of the antenna with respect to Ella model. The images which have been obtained through the subtraction artefact removal method are called "Ideal" images. The "Ideal" image is used as a reference for comparison with the resulting images from other artefact removal methods.

It should be pointed out that, for the images obtained through rotation subtraction artefact removal method, rather than rotating Ella model around its longitudinal axis, the four different positions from the angles of 0°, 5°, 40° and 45°, have been synthetised by rotating the microstrip patch antenna. Moreover, only the y-component of the electric field will be used for performing the imaging, due to x and z components vanishing. Specifically, the y-component of the electric field is calculated on a circular grid of points with radius of 110 mm and 6° phi sampling just outside the Ella head model. The images through simulation are obtained using subtraction artefact removal method are shown in Figure 6.1. Specifically, Figure 6.1 shows the images (normalised to the maximum) obtained through Equation (5.2) after subtraction artefact removal procedure for the four different transmitting positions (0°, 5°, 40° and 45°).
Imaging performance has been investigated through image quantification. For this purpose, in order to evaluate the impact of transmitting positions in achieving detection, different parameters have been introduced in Chapter 5 and calculated for the obtained images. The correspondent metrics are given in Table 6.1. It is important to point out that all the images shown here and in the following subsections were normalised and adjusted, forcing the intensity values below 0.5 to zero, whilst the S/C was always calculated before performing the image adjustment.

The images through simulation, obtained not only by using the subtraction artefact removal method, but also by employing the rotation subtraction artefact removal method. So that, the second artefact removal approach is performed using the subtraction between two sets of data (from the two closest positions of the antenna) obtained by slightly rotating the position of the antenna around the Ella head model. Figure 6.2 demonstrates the images (normalised to the

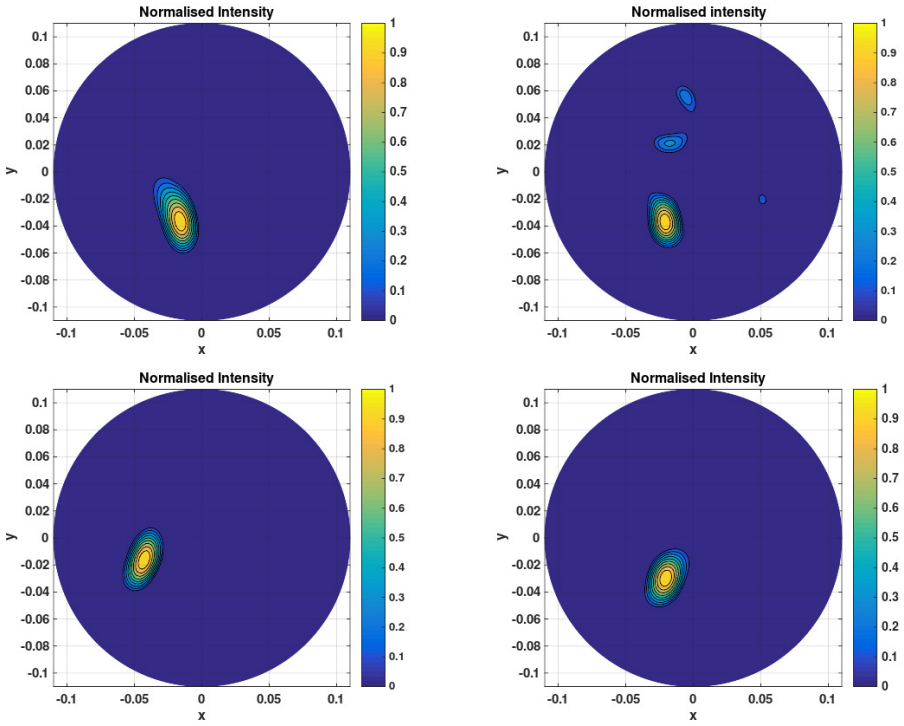

FIGURE 6.1: Images obtained using simulated data after performing artefact removal through Subtraction artefact removal method, i.e. subtracting the electric fields of Ella with a haemorrhagic stroke (calculated on a circular grid of points displaced just outside the head) and Ella without the stroke (calculated on the same grid of points). For performing subtraction, the position of the transmitting antenna has been kept fixed. The 4 images refer to the 4 different positions of the transmitting antenna used in the simulation. Images are displayed following normalisation to the maximum value and converting intensity values lower than 0.5 to 0. X and Y axes are in meters, while the intensity has an arbitrary unit.

maximum) obtained through Equation (5.2) after subtraction artefact removal procedure. As mentioned previously, the images were normalised and adjusted, forcing the intensity values below 0.5 to zero, whilst S/C was always calculated before performing the image adjustment. In Figure 6.2, the images of the head model with a haemorrhagic stroke are shown applying the rotation subtraction artefact removal procedure to simulate data, using the transmitting set 0°, 5° (left) and the transmitting set 40°, 45° (right). The corresponding S/C is given in Table 6.2.

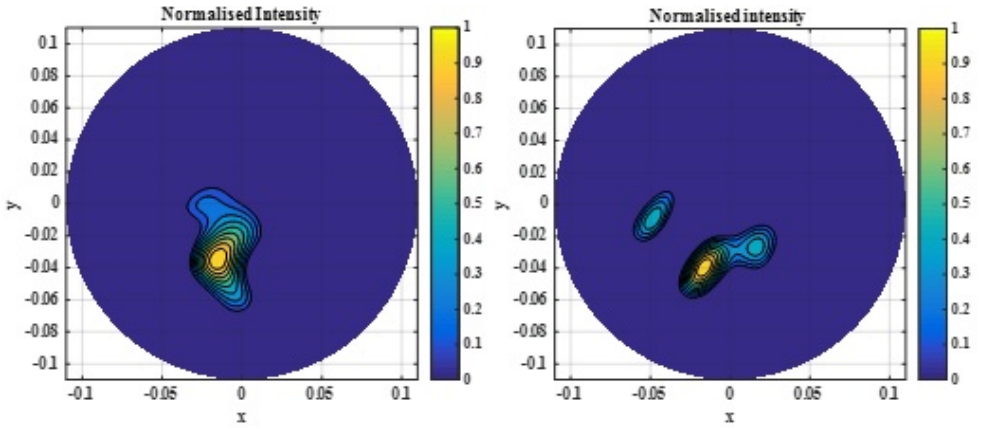

FIGURE 6.2: Images obtained using simulated data after performing artefact removal through rotation subtraction artefact removal method, i.e. subtracting two sets of data obtained by slightly rotating the position of the transmitting antenna around Ella with a haemorrhagic stroke. Images are displayed following normalisation to the maximum value and converting intensity values lower than 0.5 to 0. X and y axes are in meters, while the intensity has an arbitrary unit.

TABLE 6.1: Within-brain S/C (linear) at the frequency of 1.6 GHz (using simulation data and the Subtraction artefact removal method).

Positions	**Within-Brain S/C (linear) Subtraction**
Position 0°	2.50
Position 5°	1.91
Position 40°	1.93
Position 45°	2.49

TABLE 6.2: Within-brain S/C (linear) at the frequency of 1.6 GHz (using simulation data and the rotation subtraction artefact removal method).

Positions	**Within-Brain S/C (linear) Rotation Subtraction**
Position 0°-Position 5°	1.53
Position 40°-Position 45°	1.60

The values of S/C are different as the positions of the inclusion are different. Here, the Tables 6.1 and 6.2 are emphasizing that the position of the inclusion can vastly influence the resulting images. If the inclusion is farther from the transmitting antenna, the desired signal will be less than the clutter and consequently the value of the S/C will be less. So when the inclusion is in position 0° and 45° (in which the inclusion is closer to the transmitting antenna) the most S/C are obtained.

6.2 Phantom Imaging

6.2.1 Phantom Imaging (Measurements inside the anechoic chamber)

Frequency domain measurements have been carried out inside the anechoic chamber, to gather the transfer function S21 between the two proposed antennas through a VNA. The multi-layer phantom contains a target inclusion having specific conductivity and/or permittivity of blood. The aim is to find the existence and location of the target, using the measured field of the receiving antenna, which is collected at many points rx_{np} placed all around the phantom surface. The measurements setup inside the anechoic chamber has been explained in Chapter 4. The proposed MWI procedure is on the basis of the scattering of electromagnetic waves. Specifically, a haemorrhagic brain stroke inside a healthy tissue illuminated by an electromagnetic field transmitted by a dedicated antenna may generate a scattered field, which, if appropriately measured and processed, can be used to detect and locate the brain haemorrhage itself. In the current chapter, it is shown that the methodology permits the capturing of the extent to which different tissues, or differing conditions of tissues, can be discriminated, and hence provides contrast in the final image. As such, the dielectric constant and the conductivity of each tissue are noteworthy to be measured. Since the brain and blood clot imitating tissues contain liquids and mixtures of glycerine and water, the dielectric probe has been used here for measuring the dielectric properties, which are given in Table 6.3. As evident from the outcomes, a great agreement can be seen between the values reported in Table 6.3 and the corresponding values presented in Table 4.2 (Chapter 4). The dielectric constant and conductivity at the frequency of 1.6 GHz for the blood clot (brain haemorrhagic stroke) is equal to 60 and 1.79 S/m, respectively.

TABLE 6.3: The obtained dielectric constant and the conductivity at the frequency of 1.6 GHz for each layer of phantom.

Tissue	**Relative Permittivity(ε)**	**Conductivity**
The Brain (combination of grey matter and white matter) emulating tissue	44.75	1.05 S/m
The Skull emulating tissue	12	–
The blood clot emulating tissue	61.1	1.58 S/m

It should be emphasised that here we are interested in the results between 1 and 2 GHz, as this band is shown to be optimal for brain imaging [8]. The operating frequency of the proposed antenna is 1.6 GHz. Therefore, the obtained dielectric constant and the conductivity at the frequency of 1.6 GHz for each layer of phantom, has been presented in Table 6.3. The

average relative permittivity and conductivity (S/m) of the brain tissue are calculated by considering the average of the relative permittivity or conductivity (S/m) of the grey matter and white matter. From Table 6.3 and Table 4.2 (Chapter 4), it can be concluded that, there is an acceptable agreement between the theoretical value and real value of the dielectric constant or conductivity (S/m) of the brain, skull and blood clot (representing a brain haemorrhage). The dielectric properties of the skull mimicking tissue's mixture were measured employing the Epsilon dielectric measurement device (Biox Epsilon Model E100 fabricated at Biox System Ltd Company). The Epsilon is a device for contact measurement using a fingerprint sensor which reacts to capacitance. It is useful for measurements on isolated soft solids. It is worth mentioning that this device cannot provide the dielectric value at the frequency of interest, but can provide the permittivity values at frequency of 0 Hz.

There are a number of different ways to get an image of somebody's finger. The most common methods today are optical scanning and capacitance scanning. Both types come up with the same sort of image, but they go about it in totally different ways. The Epsilon (Biox Systems Ltd, England), is using the method of capacitance scanning. Like optical scanners, capacitive fingerprint scanners generate an image of the ridges and valleys that make up a fingerprint. But instead of sensing the print using light, the capacitors use electrical current.

A simple capacitive sensor is made up of one or more semiconductor chips containing an array of tiny cells. Each cell consist of two conductor plates, covered with an insulating layer. The cells are tiny (smaller than the width of one ridge on a finger). The sensor is connected to an integrator, an electrical circuit built around an inverting operational amplifier. The inverting amplifier is a complex semiconductor device, made up of a number of transistors, resistors and capacitors. Like any amplifier, an inverting amplifier alters one current based on fluctuations in another current.

Specifically, the inverting amplifier alters a supply voltage. The alteration is based on the relative voltage of two inputs, called the inverting terminal and the non-inverting terminal. In this case, the non-inverting terminal is connected to ground, and the inverting terminal is connected to a reference voltage supply and a feedback loop. The feedback loop, which is also connected to the amplifier output, includes the two conductor plates. To scan the finger, the processor first closes the reset switch for each cell, which shorts each amplifier's input and output to "balance" the integrator circuit. When the switch is opened again, and the processor applies a fixed charge to the integrator circuit, the capacitors charge up. The capacitance of the feedback loop's capacitor affects the voltage at the amplifier's input, which affects the amplifier's output. Since the distance to the finger alters capacitance, a finger ridge will result in a different voltage output than a finger valley. The scanner processor reads this voltage output and determines whether it

is characteristic of a ridge or a valley. By reading every cell in the sensor array, the processor can put together an overall picture of the fingerprint, similar to the image captured by an optical scanner [103].

Nevertheless, this is appropriate for a material which is made up of constituents that do not experience any changes with frequency variation like oil and flour [104],[105]. Since the skull mimicking tissue comprises mainly a high percentage of corn flour and sunflower oil, the obtained measured permittivity with this device at 0 Hz frequency has been considered equivalent to its permittivity at a frequency of 1.6 GHz.

The images through measurements, obtained using (only) rotation subtraction artefact removal method, are shown in Figure 6.3. It is worth noting that, same as other images presented in this chapter, the images were normalised and adjusted, forcing the intensity values below 0.5 to zero, whilst S/C was always calculated before performing the image adjustment. Figure 6.3 shows the microwave images of the phantom obtained through Equation (5.2), after applying rotation subtraction artefact removal to the four doublets (0° and 5°; 90° and 95°; 180° and 185°; 270° and 275°), separately. The correspondent S/C is given in Table 6.4.

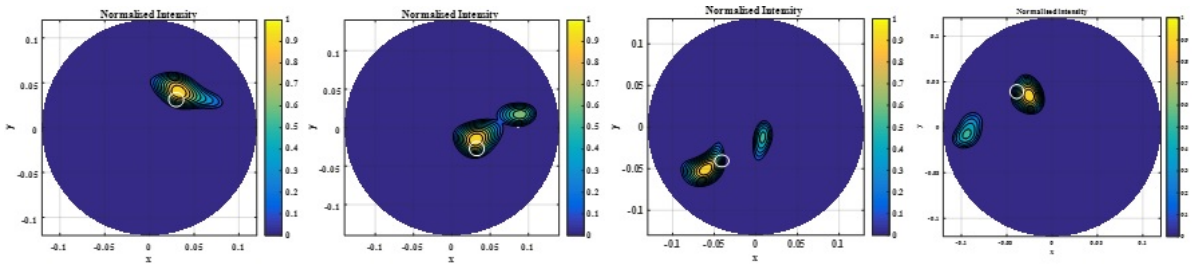

FIGURE 6.3: Images obtained using measured data (inside the anechoic chamber) after performing artefact removal through rotation Subtraction artefact removal method, i.e. subtracting four pairs of data obtained by slightly rotating the position of the transmitting antenna around the phantom with inclusion. Images are displayed following normalisation to the maximum value and converting intensity values lower than 0.5 to 0. X and y axes are in meters, while the intensity has an arbitrary unit. The white circles represent the actual location of the inclusion mimicking the haemorrhagic stroke inside the head phantom.

TABLE 6.4: S/C (linear) at the frequency of 1.6 GHz (using measurements data and the rotation subtraction artefact removal method).

Positions	Within-Brain S/C (linear) Rotation Subtraction
Position 0°-Position 5°	1.85
Position 90°-Position 95°	1.48
Position 180°-Position 185°	1.63
Position 270°-Position 275°	1.50

6.2.2 Phantom Imaging (Measurements through MWI Device)

Most research, containing the investigations which have been done by LSBU, has principally been concentrated on the detection of breast cancer. This research has provided a new application for an apparatus which has successfully detected inclusions in breast-mimicking phantoms [23] and has been successfully verified in preliminary clinical trials [22].

I have adapted the methods used to detect brain cancer and have produced promising research using the technology for stroke detection.

In this section the quantification of artefact removal procedures and the images obtained through measurements using MWI device will be performed. The description of MWI device has been given in Section 4.4.2. A phantom mimicking human head with a brain haemorrhage are realised, applying millimetric cylindrically shaped inclusion to emulate a haemorrhagic brain stroke. Moreover, the designed and fabricated specific mould for using in MWI device was used and the measurements have been performed by recording the complex S21 in a multi-bistatic fashion, i.e. for each transmitting position tx_m the receiving antenna is moved to measure the received signal every 4.5°, leading to a total of 80 receiving points rx_{np}. Concerning the transmitting positions, all the experiments have been done by employing 15 transmitting position, displaced in 5 triplets cantered at 0°, 72°, 144°, 216°, and 288°. For each triplet the three transmitting positions are displaced by 9° (The transmitting source position x was set as 3 transmission points spaced 4.5° apart at 0).

For each transmitting and receiving positions, the complex S21 is collected from 1 to 6 GHz, with 5 MHz sampling. Then during running the codes, we will consider the frequency of 1 to 1.5 GHz, as this band has demonstrated to be ideal and optimal to do brain imaging [8]. Furthermore, with the aim of proving this fact that the frequency of 1 to 1.5 GHz is the ideal and optimal frequency to do brain imaging, we have provided and presented here the resulting images at frequency 1 to 6 GHz (1.5-2 GHz, 2-2.5 GHz, 2.5-3 GHz, 3-3.5 GHz, 3.5-4 GHz, 4-4.5 GHz, 4.5-5 GHz, 5-5.5 GHz, 5.5-6 GHz). Figure 6.4 shows the "Ideal" image generated by subtracting two sets of data of the phantom with no inclusion from the one with an inclusion

(positioned at 0°, 90°, 180° and 270°) at frequency 1.5 to 2 GHz.

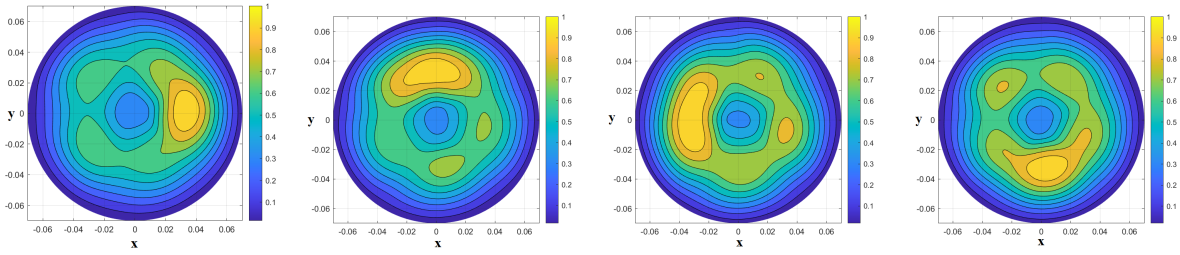

FIGURE 6.4: "Ideal" image generated by subtracting two sets of data of the phantom with no inclusion from the one with an inclusion (positioned at 0°, 90°, 180° and 270°) at frequency 1.5 to 2 GHz. X and Y axes are in meters, while the intensity has an arbitrary unit.

Figure 6.5 demonstrates a combination of 5 transmitting position triplets for inclusion positioned at 0°, 90°, 180° and 270°. The images are obtained after employing the rotation subtraction between two triplet positions, functioning as an artefact removal procedure at frequency 1.5 to 2 GHz.

Figure 6.6 presents the final images for inclusion positioned at 0°, 90°, 180° and 270°. The images are obtained after using local average subtraction artefact removal method (in a same triplet positions), functioning as an artefact removal procedure at frequency 1.5 to 2 GHz.

Figure 6.7 the final images considering the inclusion positioned at 0°, 90°, 180° and 270° and applying differential symmetric receiver type have been illustrated at frequency 1.5 to 2 GHz.

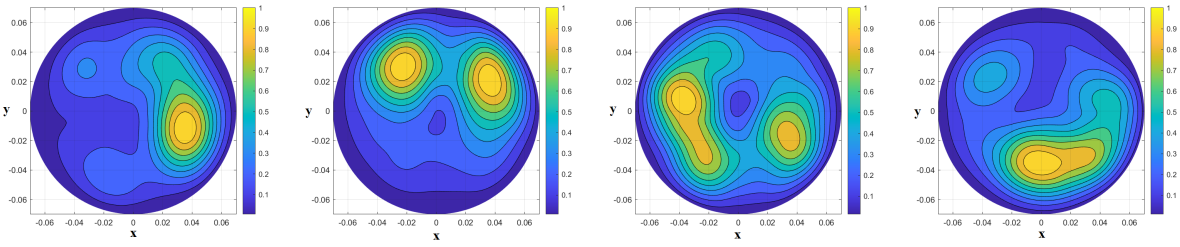

FIGURE 6.5: A combination of 5 transmitting position triplets for inclusion at 0°, 90°, 180° and 270°. Microwave images obtained using measured data with MWI device after performing artefact removal through rotation subtraction artefact removal method at frequency 1.5 to 2 GHz. X and Y axes are in meters, while the intensity has an arbitrary unit.

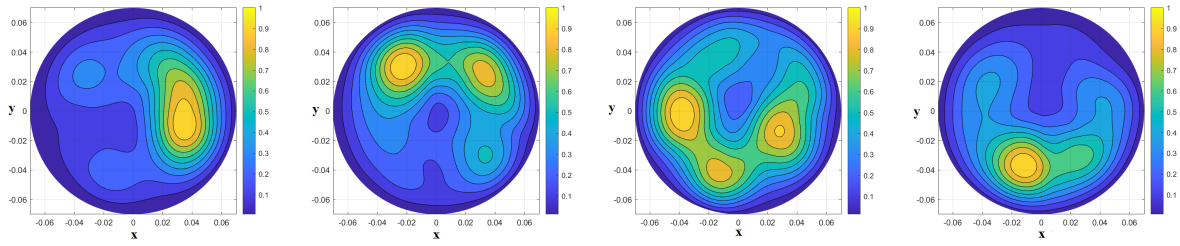

FIGURE 6.6: A combination of 5 transmitting position triplets for inclusion at 0°, 90°, 180° and 270°. Microwave images obtained using measured data with MWI device after performing artefact removal through local average subtraction artefact removal method at frequency 1.5 to 2 GHz. X and Y axes are in meters, while the intensity has an arbitrary unit.

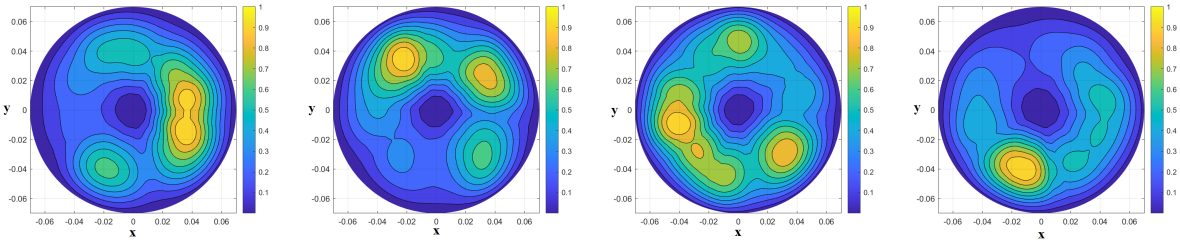

FIGURE 6.7: A combination of 5 transmitting position triplets for inclusion at 0°, 90°, 180° and 270°. Microwave images obtained using measured data with MWI device after performing artefact removal through differential symmetric receiver type artefact removal method at frequency 1.5 to 2 GHz. X and Y axes are in meters, while the intensity has an arbitrary unit.

Figure 6.8 indicates the final images for the inclusion positioned at 0°, 90°, 180°, 270° and employing summed symmetric differential artefact removal method at frequency 1.5 to 2 GHz. Figure 6.9 shows the "Ideal" image generated by subtracting two sets of data of the phantom with no inclusion from the one with an inclusion (positioned at 0°, 90°, 180° and 270°) at frequency 2 to 2.5 GHz. Figure 6.10 demonstrates a combination of 5 transmitting position triplets for inclusion positioned at 0°, 90°, 180° and 270°. The images are obtained after employing the rotation subtraction between two triplet positions, functioning as an artefact removal procedure at frequency 2 to 2.5 GHz. Figure 6.11 presents the final images for inclusion positioned at 0°, 90°, 180° and 270°. The images are obtained after using local average subtraction artefact removal method (in a same triplet positions), functioning as an artefact removal procedure at frequency 2 to 2.5 GHz.

Figure 6.12 the final images considering the inclusion positioned at 0°, 90°, 180° and 270°

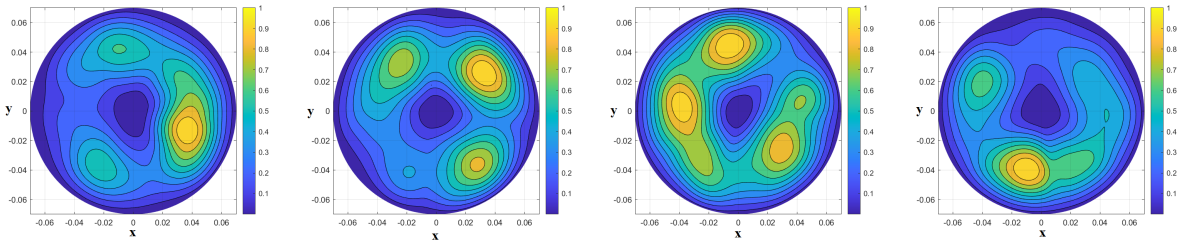

FIGURE 6.8: A combination of 5 transmitting position triplets for inclusion at 0°, 90°, 180° and 270°. Microwave images obtained using measured data with MWI device after performing artefact removal through summed symmetric differential artefact removal method at frequency 1.5 to 2 GHz. X and Y axes are in meters, while the intensity has an arbitrary unit.

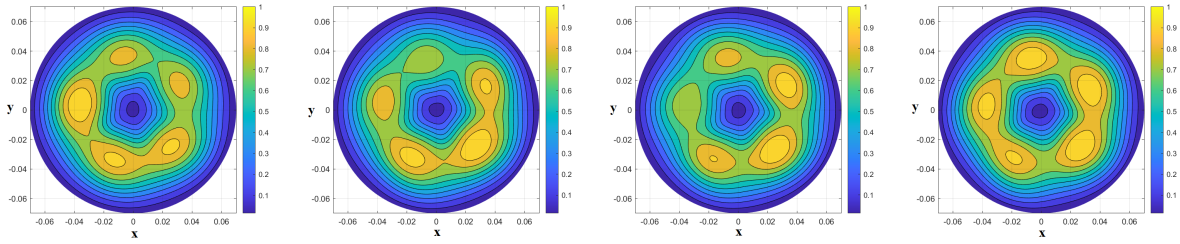

FIGURE 6.9: "Ideal" image generated by subtracting two sets of data of the phantom with no inclusion from the one with an inclusion (positioned at 0°, 90°, 180° and 270°) at frequency 2 to 2.5 GHz. X and Y axes are in meters, while the intensity has an arbitrary unit.

and applying differential symmetric receiver type have been illustrated at frequency 2 to 2.5 GHz.

Figure 6.13 indicates the final images for the inclusion positioned at 0°, 90°, 180° and 270° and employing summed symmetric differential artefact removal method at frequency 2 to 2.5 GHz.

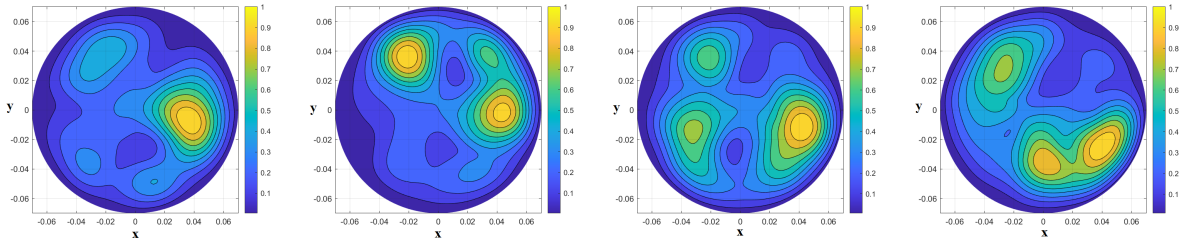

FIGURE 6.10: A combination of 5 transmitting position triplets for inclusion at 0°, 90°, 180° and 270°. Microwave images obtained using measured data with MWI device after performing artefact removal through rotation subtraction artefact removal method at frequency 2 to 2.5 GHz. X and Y axes are in meters, while the intensity has an arbitrary unit.

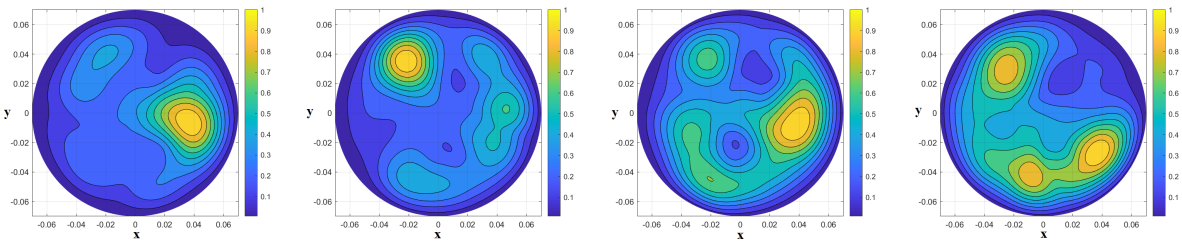

FIGURE 6.11: A combination of 5 transmitting position triplets for inclusion at 0°, 90°, 180° and 270°. Microwave images obtained using measured data with MWI device after performing artefact removal through local average subtraction artefact removal method at frequency 2 to 2.5 GHz. X and Y axes are in meters, while the intensity has an arbitrary unit.

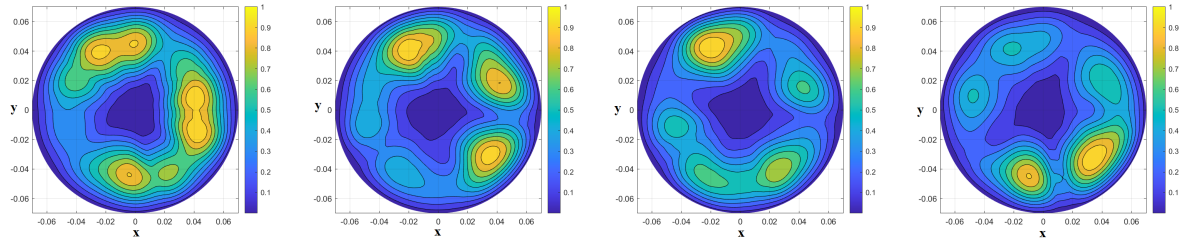

FIGURE 6.12: A combination of 5 transmitting position triplets for inclusion at 0°, 90°, 180° and 270°. Microwave images obtained using measured data with MWI device after performing artefact removal through differential symmetric receiver type artefact removal method at frequency 2 to 2.5 GHz. X and Y axes are in meters, while the intensity has an arbitrary unit.

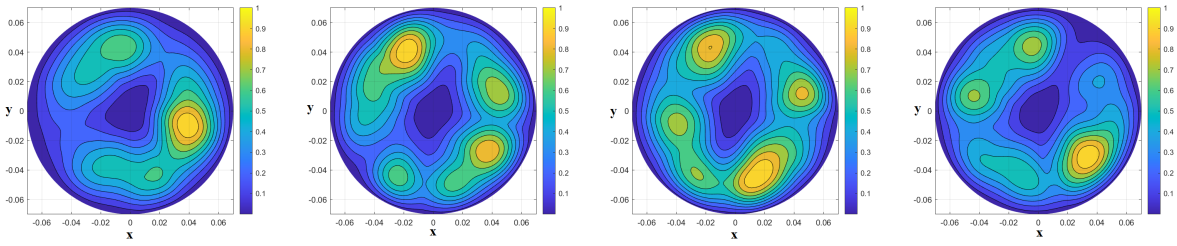

FIGURE 6.13: A combination of 5 transmitting position triplets for inclusion at 0°, 90°, 180° and 270°. Microwave images obtained using measured data with MWI device after performing artefact removal through summed symmetric differential artefact removal method at frequency 2 to 2.5 GHz. X and Y axes are in meters, while the intensity has an arbitrary unit.

Figure 6.14 shows the "Ideal" image generated by subtracting two sets of data of the phantom with no inclusion from the one with an inclusion (positioned at 0°, 90°, 180° and 270°) at frequency 2.5 to 3 GHz. Figure 6.15 demonstrates a combination of 5 transmitting position triplets for inclusion positioned at 0°, 90°, 180° and 270°. The images are obtained after employing the rotation subtraction between two triplet positions, functioning as an artefact removal procedure at frequency 2.5 to 3 GHz. Figure 6.16 presents the final images for inclusion positioned at 0°, 90°, 180° and 270°. The images are obtained after using local average subtraction artefact removal method (in a same triplet positions), functioning as an artefact removal procedure at frequency 2.5 to 3 GHz.

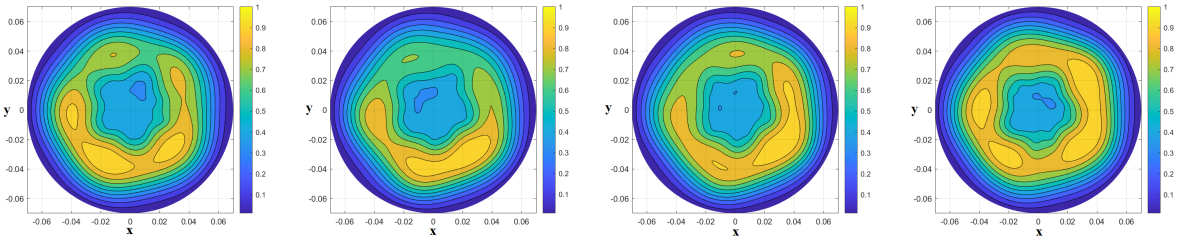

FIGURE 6.14: "Ideal" image generated by subtracting two sets of data of the phantom with no inclusion from the one with an inclusion (positioned at 0°, 90°, 180° and 270°) at frequency 2.5 to 3 GHz. X and Y axes are in meters, while the intensity has an arbitrary unit.

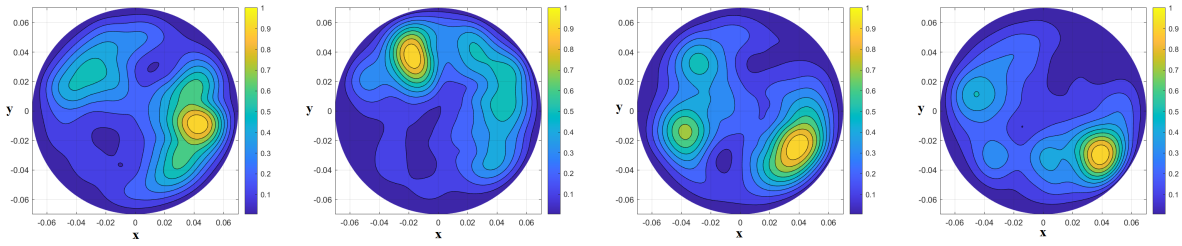

FIGURE 6.15: A combination of 5 transmitting position triplets for inclusion at 0°, 90°, 180° and 270°. Microwave images obtained using measured data with MWI device after performing artefact removal through rotation subtraction artefact removal method at frequency 2.5 to 3 GHz. X and Y axes are in meters, while the intensity has an arbitrary unit.

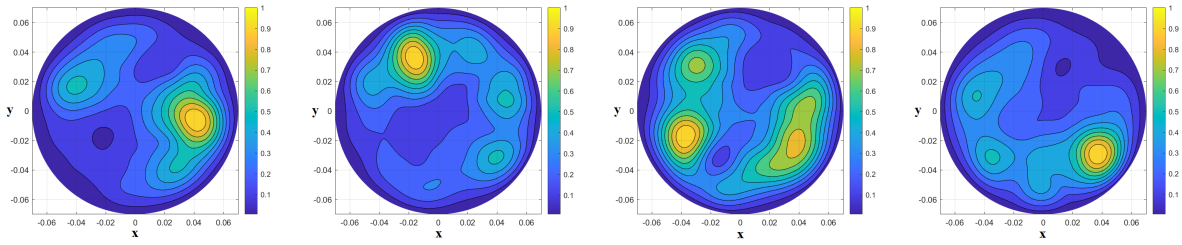

FIGURE 6.16: A combination of 5 transmitting position triplets for inclusion at 0°, 90°, 180° and 270°. Microwave images obtained using measured data with MWI device after performing artefact removal through local average subtraction artefact removal method at frequency 2.5 to 3 GHz. X and Y axes are in meters, while the intensity has an arbitrary unit.

Figure 6.17 the final images considering the inclusion positioned at 0°, 90°, 180° and 270° and applying differential symmetric receiver type have been illustrated at frequency 2.5 to 3 GHz.

Figure 6.18 indicates the final images for the inclusion positioned at 0°, 90°, 180° and 270° and employing summed symmetric differential artefact removal method at frequency 2.5 to 3 GHz.

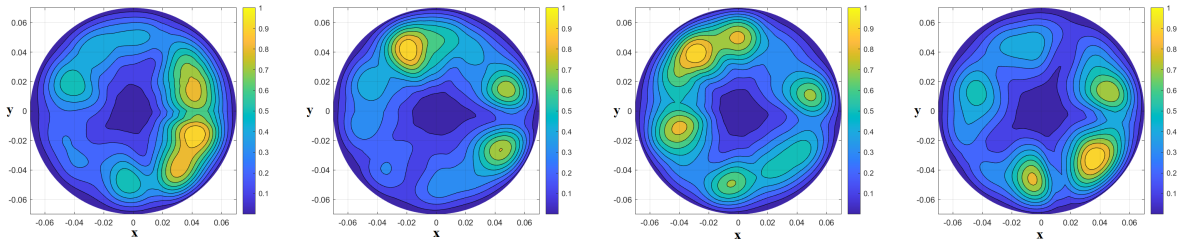

FIGURE 6.17: A combination of 5 transmitting position triplets for inclusion at 0°, 90°, 180° and 270°. Microwave images obtained using measured data with MWI device after performing artefact removal through differential symmetric receiver type artefact removal method at frequency 2.5 to 3 GHz. X and Y axes are in meters, while the intensity has an arbitrary unit.

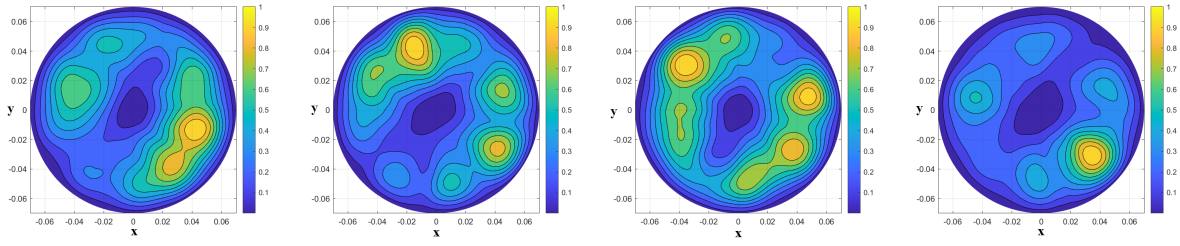

FIGURE 6.18: A combination of 5 transmitting position triplets for inclusion at 0°, 90°, 180° and 270°. Microwave images obtained using measured data with MWI device after performing artefact removal through summed symmetric differential artefact removal method at frequency 2.5 to 3 GHz. X and Y axes are in meters, while the intensity has an arbitrary unit.

Figure 6.19 shows the "Ideal" image generated by subtracting two sets of data of the phantom with no inclusion from the one with an inclusion (positioned at 0°, 90°, 180° and 270°) at frequency 3 to 3.5 GHz. Figure 6.20 demonstrates a combination of 5 transmitting position triplets for inclusion positioned at 0°, 90°, 180° and 270°. The images are obtained after employing the rotation subtraction between two triplet positions, functioning as an artefact removal procedure at frequency 3 to 3.5 GHz. Figure 6.21 presents the final images for inclusion positioned at 0°, 90°, 180° and 270°. The images are obtained after using local average subtraction artefact removal method (in a same triplet positions), functioning as an artefact removal procedure at frequency 3 to 3.5 GHz. Figure 6.22 the final images considering the inclusion positioned at 0°, 90°, 180° and 270° and applying differential symmetric receiver type have been illustrated at frequency 3 to 3.5 GHz. Figure 6.23 indicates the final images for the inclusion positioned at 0°, 90°, 180° and 270° and employing summed symmetric differential artefact

removal method at frequency 3 to 3.5 GHz.

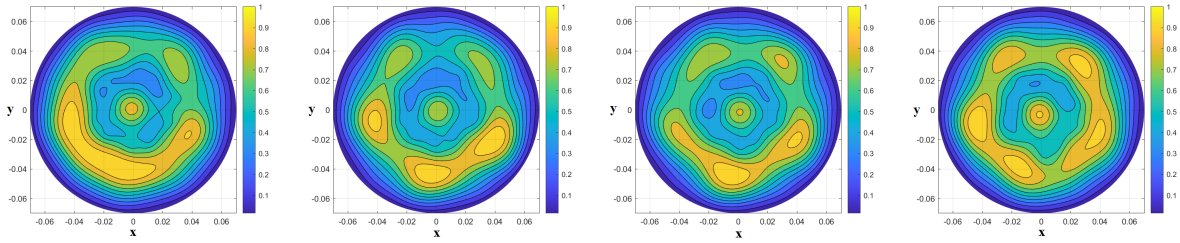

FIGURE 6.19: "Ideal" image generated by subtracting two sets of data of the phantom with no inclusion from the one with an inclusion (positioned at 0°, 90°, 180° and 270°) at frequency 3 to 3.5 GHz. X and Y axes are in meters, while the intensity has an arbitrary unit.

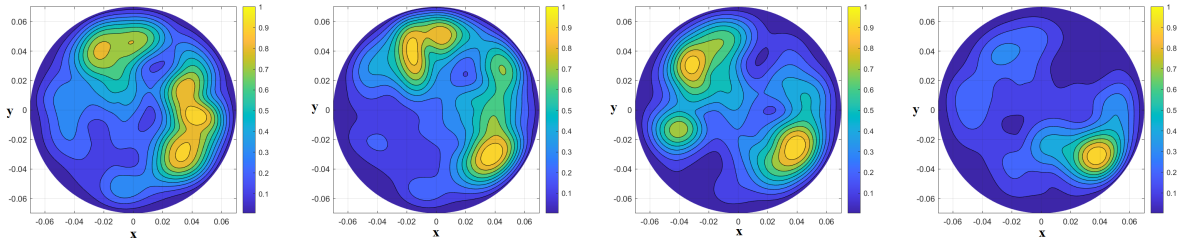

FIGURE 6.20: A combination of 5 transmitting position triplets for inclusion at 0°, 90°, 180° and 270°. Microwave images obtained using measured data with MWI device after performing artefact removal through rotation subtraction artefact removal method at frequency 3 to 3.5 GHz. X and Y axes are in meters, while the intensity has an arbitrary unit.

Figure 6.24 shows the "Ideal" image generated by subtracting two sets of data of the phantom with no inclusion from the one with an inclusion (positioned at 0°, 90°, 180° and 270°) at frequency 3.5 to 4 GHz.

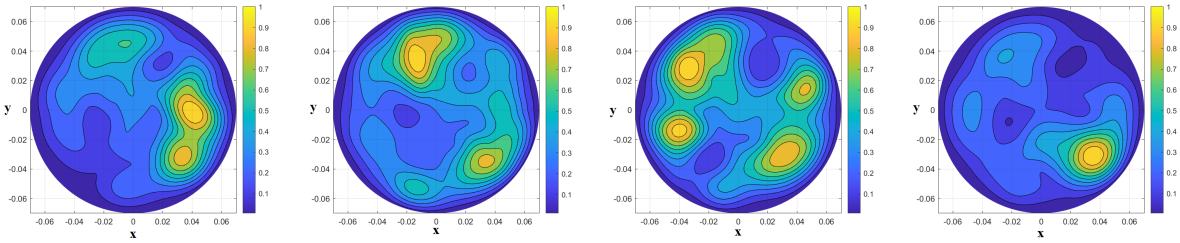

FIGURE 6.21: A combination of 5 transmitting position triplets for inclusion at 0°, 90°, 180° and 270°. Microwave images obtained using measured data with MWI device after performing artefact removal through local average subtraction artefact removal method at frequency 3 to 3.5 GHz. X and Y axes are in meters, while the intensity has an arbitrary unit.

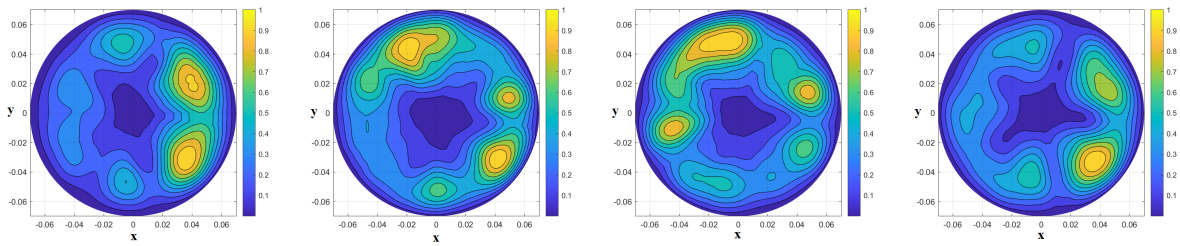

FIGURE 6.22: A combination of 5 transmitting position triplets for inclusion at 0°, 90°, 180° and 270°. Microwave images obtained using measured data with MWI device after performing artefact removal through differential symmetric receiver type artefact removal method at frequency 3 to 3.5 GHz. X and Y axes are in meters, while the intensity has an arbitrary unit.

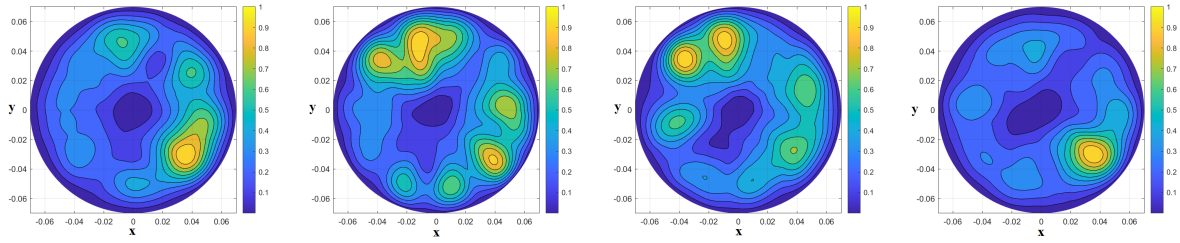

FIGURE 6.23: A combination of 5 transmitting position triplets for inclusion at 0°, 90°, 180° and 270°. Microwave images obtained using measured data with MWI device after performing artefact removal through summed symmetric differential artefact removal method at frequency 3 to 3.5 GHz. X and Y axes are in meters, while the intensity has an arbitrary unit.

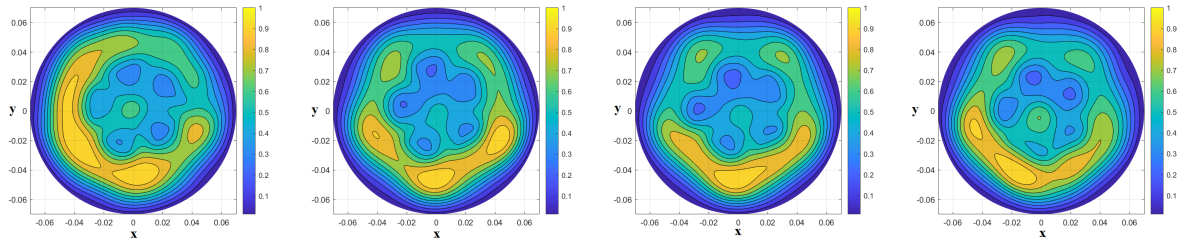

FIGURE 6.24: "Ideal" image generated by subtracting two sets of data of the phantom with no inclusion from the one with an inclusion (positioned at 0°, 90°, 180° and 270°) at frequency 3.5 to 4 GHz. X and Y axes are in meters, while the intensity has an arbitrary unit.

Figure 6.25 demonstrates a combination of 5 transmitting position triplets for inclusion positioned at 0°, 90°, 180° and 270°. The images are obtained after employing the rotation subtraction between two triplet positions, functioning as an artefact removal procedure at frequency 3.5 to 4 GHz.

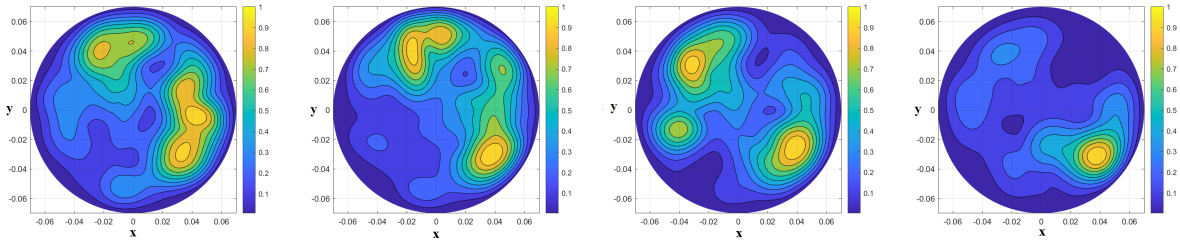

FIGURE 6.25: A combination of 5 transmitting position triplets for inclusion at 0°, 90°, 180° and 270°. Microwave images obtained using measured data with MWI device after performing artefact removal through rotation subtraction artefact removal method at frequency 3.5 to 4 GHz. X and Y axes are in meters, while the intensity has an arbitrary unit.

Figure 6.26 presents the final images for inclusion positioned at 0°, 90°, 180° and 270°. The images are obtained after using local average subtraction artefact removal method (in a same triplet positions), functioning as an artefact removal procedure at frequency 3.5 to 4 GHz.

Figure 6.27 the final images considering the inclusion positioned at 0°, 90°, 180° and 270° and applying differential symmetric receiver type have been illustrated at frequency 3.5 to 4 GHz.

Figure 6.28 indicates the final images for the inclusion positioned at 0°, 90°, 180° and 270° and employing summed symmetric differential artefact removal method at frequency 3.5 to 4 GHz.

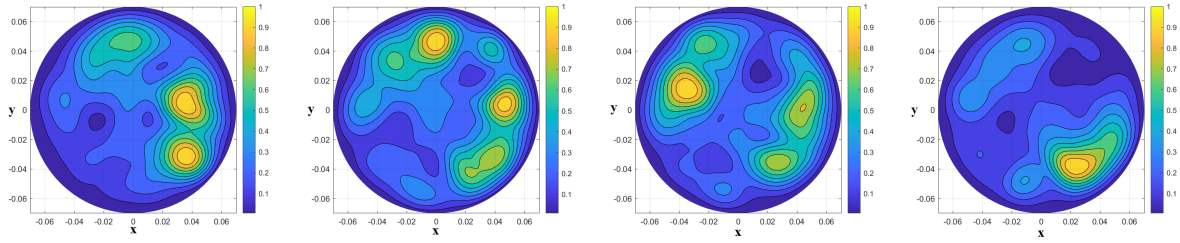

FIGURE 6.26: A combination of 5 transmitting position triplets for inclusion at 0°, 90°, 180° and 270°. Microwave images obtained using measured data with MWI device after performing artefact removal through local average subtraction artefact removal method at frequency 3.5 to 4 GHz. X and Y axes are in meters, while the intensity has an arbitrary unit.

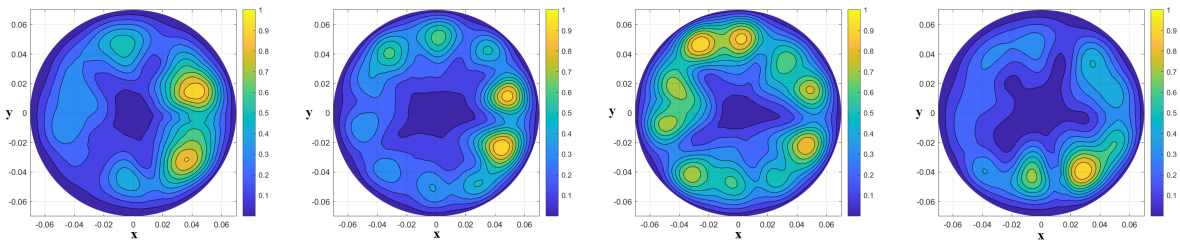

FIGURE 6.27: A combination of 5 transmitting position triplets for inclusion at 0°, 90°, 180° and 270°. Microwave images obtained using measured data with MWI device after performing artefact removal through differential symmetric receiver type artefact removal method at frequency 3.5 to 4 GHz. X and Y axes are in meters, while the intensity has an arbitrary unit.

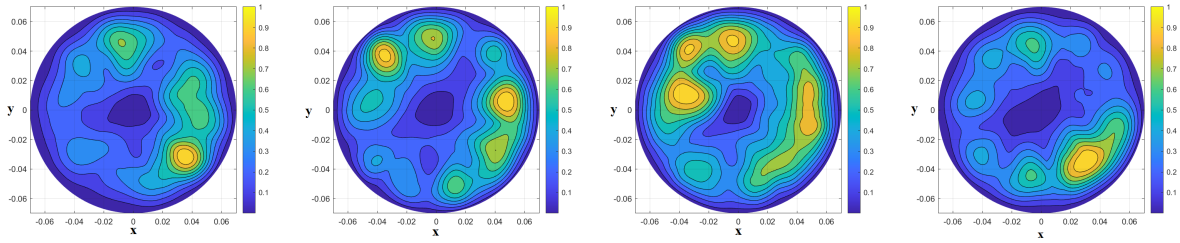

FIGURE 6.28: A combination of 5 transmitting position triplets for inclusion at 0°, 90°, 180° and 270°. Microwave images obtained using measured data with MWI device after performing artefact removal through summed symmetric differential artefact removal method at frequency 3.5 to 4 GHz. X and Y axes are in meters, while the intensity has an arbitrary unit.

Figure 6.29 shows the "Ideal" image generated by subtracting two sets of data of the phantom with no inclusion from the one with an inclusion (positioned at 0°, 90°, 180° and 270°) at frequency 4 to 4.5 GHz.

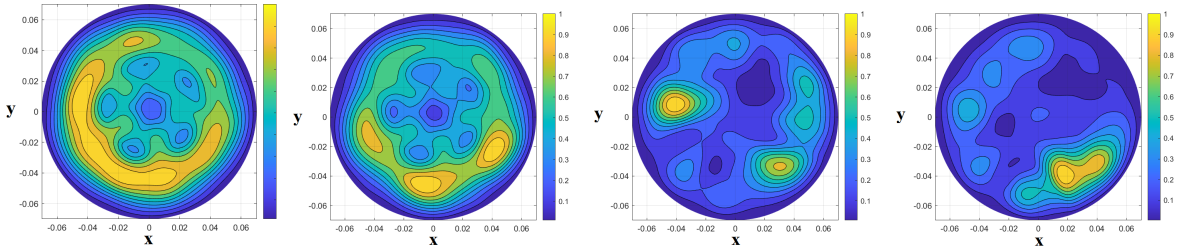

FIGURE 6.29: "Ideal" image generated by subtracting two sets of data of the phantom with no inclusion from the one with an inclusion (positioned at 0°, 90°, 180° and 270°) at frequency 4 to 4.5 GHz. X and Y axes are in meters, while the intensity has an arbitrary unit.

Figure 6.30 shows a combination of 5 transmitting position triplets for inclusion at 0°, 90°, 180° and 270°. The images are obtained after employing the rotation subtraction between two triplet positions, functioning as an artefact removal procedure at frequency 4 to 4.5 GHz.

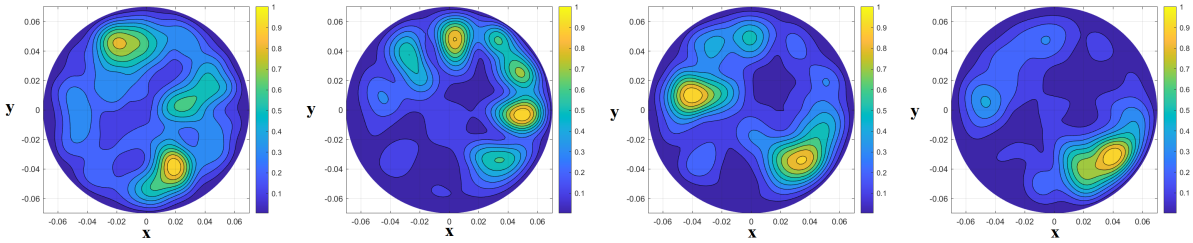

FIGURE 6.30: A combination of 5 transmitting position triplets for inclusion at 0°, 90°, 180° and 270°. Microwave images obtained using measured data with MWI device after performing artefact removal through rotation subtraction artefact removal method at frequenct 4 to 4.5 GHz. X and Y axes are in meters, while the intensity has an arbitrary unit.

Figure 6.31 presents the final images for inclusion at 0°, 90°, 180°, and 270°, using local average subtraction artefact removal method at 4 to 4.5 GHz.

In figure 6.32 the final images considering the positions of the inclusion at 0°, 90°, 180° and 270° with applying differential symmetric receiver type have been illustrated at 1 to 1.5 GHz.

Figure 6.33 indicates the final images for the inclusion positioned at 0°, 90°, 180° and 270° with employing summed symmetric differential artefact removal method.

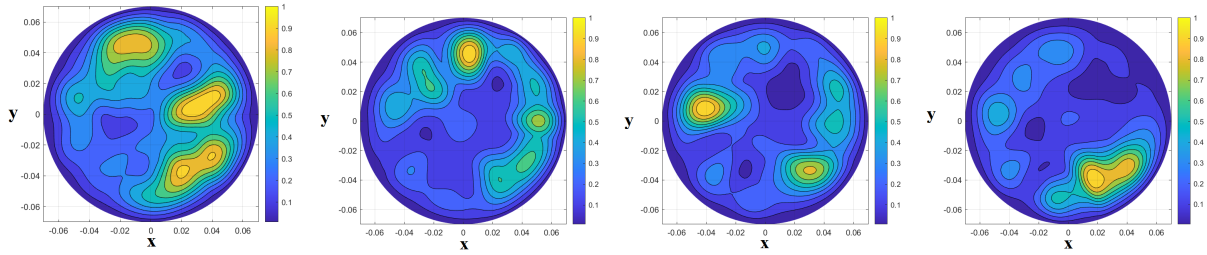

FIGURE 6.31: A combination of 5 transmitting position triplets for inclusion at 0°, 90°, 180° and 270°. Microwave images obtained using measured data with MWI device after performing artefact removal through local average subtraction artefact removal method at frequency 4 to 4.5 GHz. X and Y axes are in meters, while the intensity has an arbitrary unit.

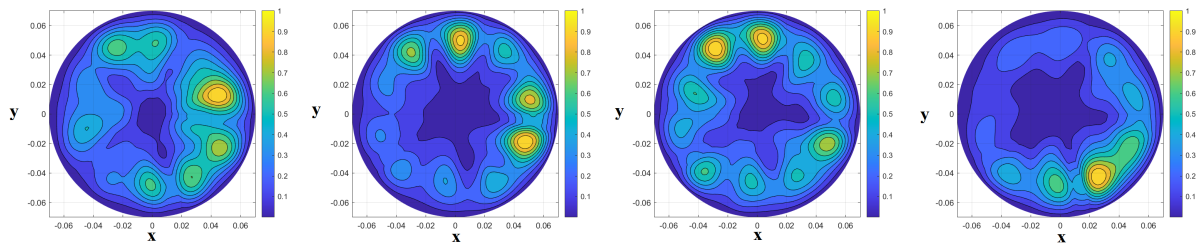

FIGURE 6.32: A combination of 5 transmitting position triplets for inclusion at 0°, 90°, 180° and 270°. Microwave images obtained using measured data with MWI device after performing artefact removal through differential symmetric receiver type artefact removal method at frequency 4 to 4.5 GHz. X and Y axes are in meters, while the intensity has an arbitrary unit.

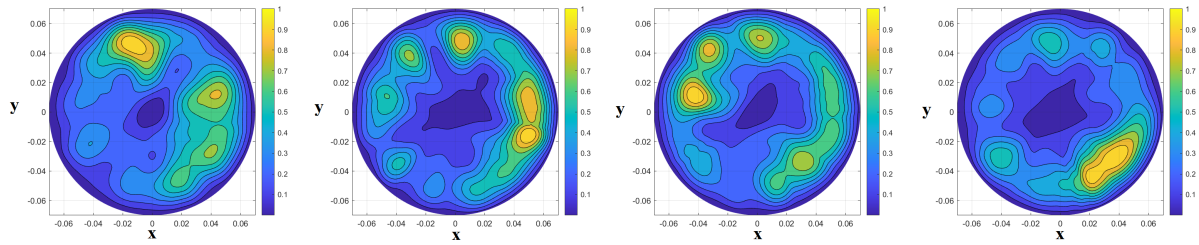

FIGURE 6.33: A combination of 5 transmitting position triplets for inclusion at 0°, 90°, 180° and 270°. Microwave images obtained using measured data with MWI device after performing artefact removal through summed symmetric differential artefact removal method at frequenct 4 to 4.5 GHz. X and Y axes are in meters, while the intensity has an arbitrary unit.

Figure 6.34 shows the "Ideal" image generated by subtracting two sets of data of the phantom with no inclusion from the one with an inclusion (positioned at 0°, 90°, 180° and 270°) at frequency 4 to 4.5 GHz.

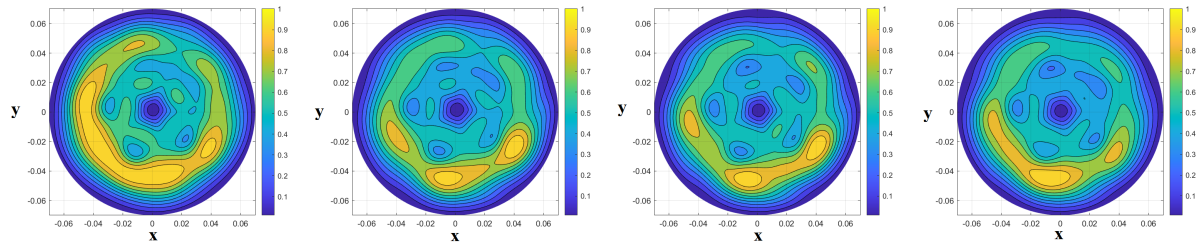

FIGURE 6.34: "Ideal" image generated by subtracting two sets of data of the phantom with no inclusion from the one with an inclusion (positioned at 0°, 90°, 180° and 270°) at frequency 4.5 to 5 GHz. X and Y axes are in meters, while the intensity has an arbitrary unit.

Figure 6.35 shows a combination of 5 transmitting position triplets for inclusion at 0°, 90°, 180° and 270°. The images are obtained after employing the rotation subtraction between two triplet positions, functioning as an artefact removal procedure at frequency 4.5 to 5 GHz.

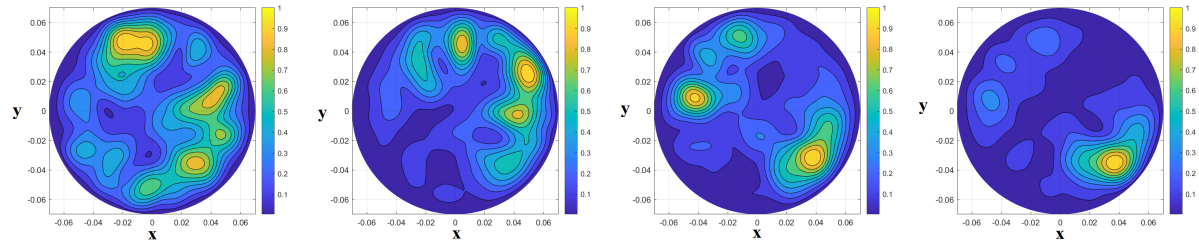

FIGURE 6.35: A combination of 5 transmitting position triplets for inclusion at 0°, 90°, 180° and 270°. Microwave images obtained using measured data with MWI device after performing artefact removal through rotation subtraction artefact removal method at frequenct 4.5 to 5 GHz. X and Y axes are in meters, while the intensity has an arbitrary unit.

Figure 6.36 presents the final images for inclusion at 0°, 90°, 180°, and 270°, using local average subtraction artefact removal method at 4.5 to 5 GHz.

In figure 6.37 the final images considering the positions of the inclusion at 0°, 90°, 180° and 270° with applying differential symmetric receiver type have been illustrated at 4.5 to 5 GHz.

Figure 6.38 indicates the final images for the inclusion positioned at 0°, 90°, 180° and 270° with employing summed symmetric differential artefact removal method.

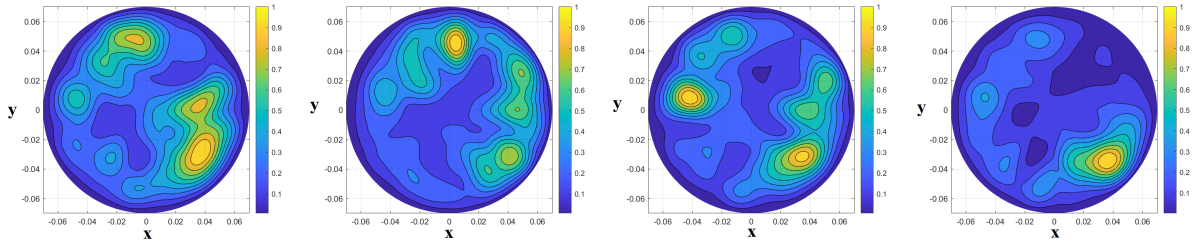

FIGURE 6.36: A combination of 5 transmitting position triplets for inclusion at 0°, 90°, 180° and 270°. Microwave images obtained using measured data with MWI device after performing artefact removal through local average subtraction artefact removal method at frequency 4.5 to 5 GHz. X and Y axes are in meters, while the intensity has an arbitrary unit.

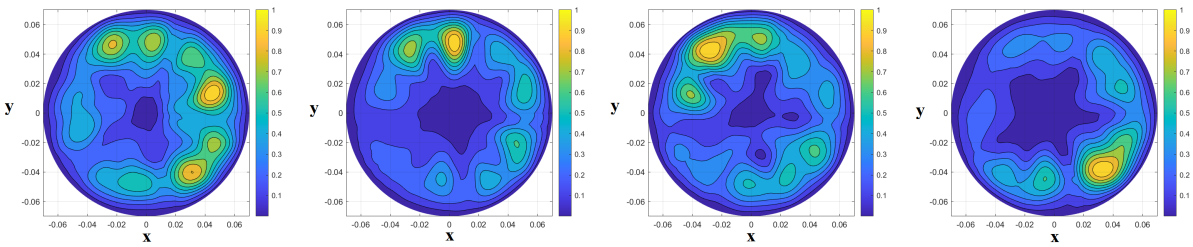

FIGURE 6.37: A combination of 5 transmitting position triplets for inclusion at 0°, 90°, 180° and 270°. Microwave images obtained using measured data with MWI device after performing artefact removal through differential symmetric receiver type artefact removal method at frequency 4.5 to 5 GHz. X and Y axes are in meters, while the intensity has an arbitrary unit.

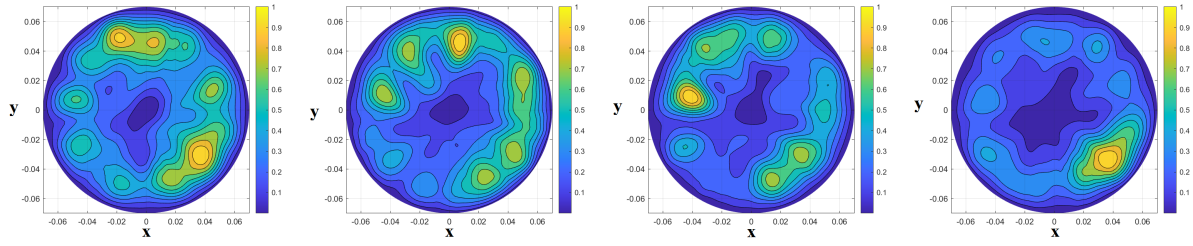

FIGURE 6.38: A combination of 5 transmitting position triplets for inclusion at 0°, 90°, 180° and 270°. Microwave images obtained using measured data with MWI device after performing artefact removal through summed symmetric differential artefact removal method at frequenct 4.5 to 5 GHz. X and Y axes are in meters, while the intensity has an arbitrary unit.

Figure 6.39 shows the "Ideal" image generated by subtracting two sets of data of the phantom with no inclusion from the one with an inclusion (positioned at 0°, 90°, 180° and 270°) at frequency 5 to 5.5 GHz.

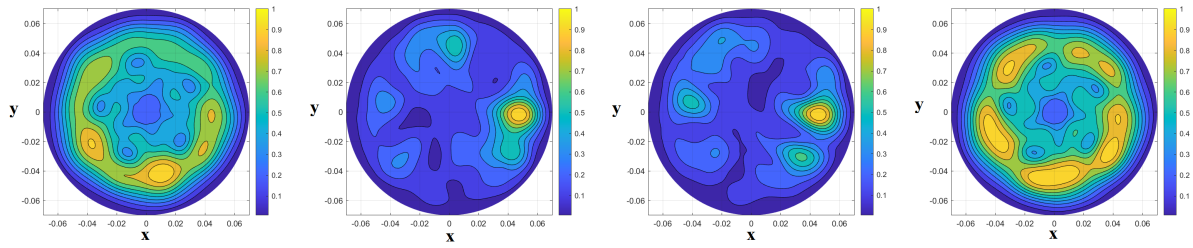

FIGURE 6.39: "Ideal" image generated by subtracting two sets of data of the phantom with no inclusion from the one with an inclusion (positioned at 0°, 90°, 180° and 270°) at frequency 5 to 5.5 GHz. X and Y axes are in meters, while the intensity has an arbitrary unit.

Figure 6.40 shows a combination of 5 transmitting position triplets for inclusion at 0°, 90°, 180° and 270°. The images are obtained after employing the rotation subtraction between two triplet positions, functioning as an artefact removal procedure at frequency 5 to 5.5 GHz.

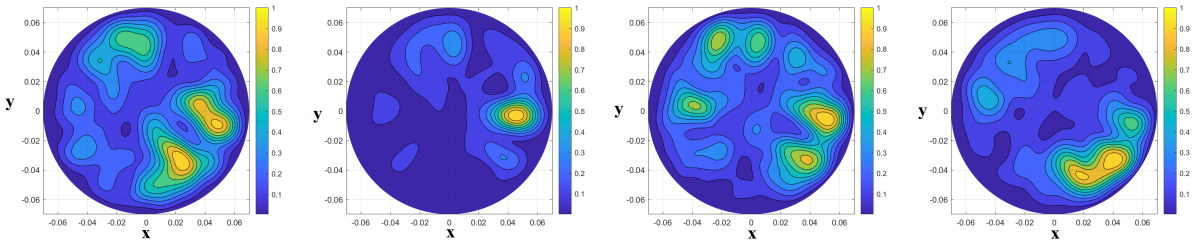

FIGURE 6.40: A combination of 5 transmitting position triplets for inclusion at 0°, 90°, 180° and 270°. Microwave images obtained using measured data with MWI device after performing artefact removal through rotation subtraction artefact removal method at frequenct 5 to 5.5 GHz. X and Y axes are in meters, while the intensity has an arbitrary unit.

Figure 6.41 presents the final images for inclusion at 0°, 90°, 180°, and 270°, using local average subtraction artefact removal method at 5 to 5.5 GHz.

In figure 6.42 the final images considering the positions of the inclusion at 0°, 90°, 180° and 270° with applying differential symmetric receiver type have been illustrated at 5 to 5.5 GHz.

Figure 6.43 indicates the final images for the inclusion positioned at 0°, 90°, 180° and 270° with employing summed symmetric differential artefact removal method.

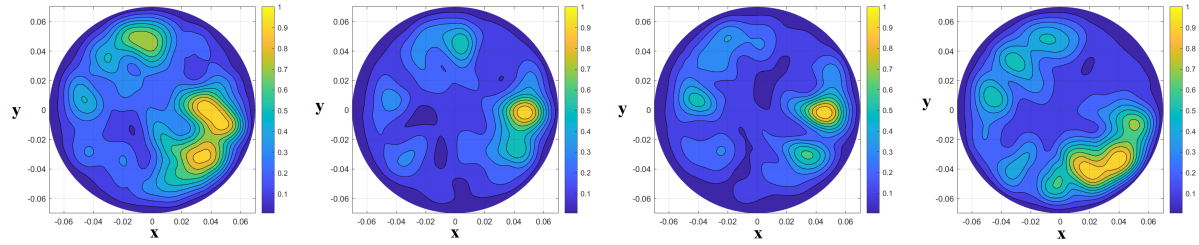

FIGURE 6.41: A combination of 5 transmitting position triplets for inclusion at 0°, 90°, 180° and 270°. Microwave images obtained using measured data with MWI device after performing artefact removal through local average subtraction artefact removal method at frequency 5 to 5.5 GHz. X and Y axes are in meters, while the intensity has an arbitrary unit.

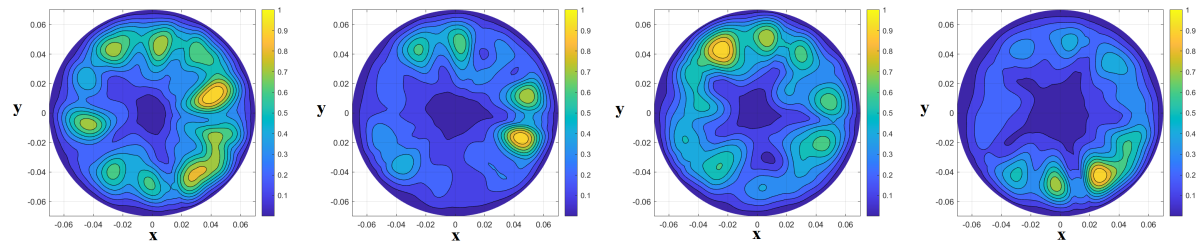

FIGURE 6.42: A combination of 5 transmitting position triplets for inclusion at 0°, 90°, 180° and 270°. Microwave images obtained using measured data with MWI device after performing artefact removal through differential symmetric receiver type artefact removal method at frequency 5 to 5.5 GHz. X and Y axes are in meters, while the intensity has an arbitrary unit.

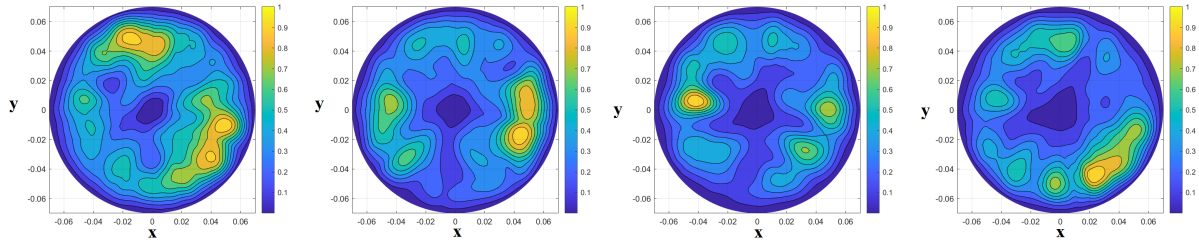

FIGURE 6.43: A combination of 5 transmitting position triplets for inclusion at 0°, 90°, 180° and 270°. Microwave images obtained using measured data with MWI device after performing artefact removal through summed symmetric differential artefact removal method at frequenct 5 to 5.5 GHz. X and Y axes are in meters, while the intensity has an arbitrary unit.

Figure 6.44 shows the "Ideal" image generated by subtracting two sets of data of the phantom with no inclusion from the one with an inclusion (positioned at 0°, 90°, 180° and 270°) at frequency 5.5 to 6 GHz.

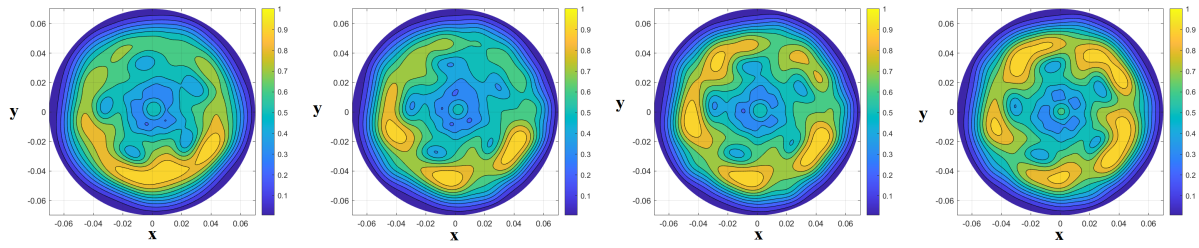

FIGURE 6.44: "Ideal" image generated by subtracting two sets of data of the phantom with no inclusion from the one with an inclusion (positioned at 0°, 90°, 180° and 270°) at frequency 5.5 to 6 GHz. X and Y axes are in meters, while the intensity has an arbitrary unit.

Figure 6.45 shows a combination of 5 transmitting position triplets for inclusion at 0°, 90°, 180° and 270°. The images are obtained after employing the rotation subtraction between two triplet positions, functioning as an artefact removal procedure at frequency 5.5 to 6 GHz.

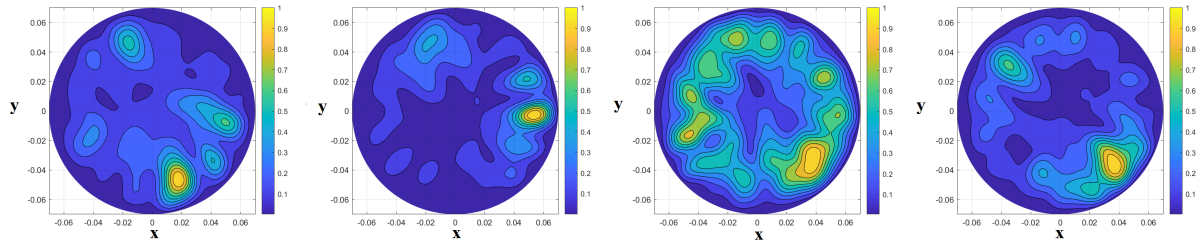

FIGURE 6.45: A combination of 5 transmitting position triplets for inclusion at 0°, 90°, 180° and 270°. Microwave images obtained using measured data with MWI device after performing artefact removal through rotation subtraction artefact removal method at frequenct 5.5 to 6 GHz. X and Y axes are in meters, while the intensity has an arbitrary unit.

Figure 6.46 presents the final images for inclusion at 0°, 90°, 180°, and 270°, using local average subtraction artefact removal method at 5.5 to 6 GHz.

In figure 6.47 the final images considering the positions of the inclusion at 0°, 90°, 180° and 270° with applying differential symmetric receiver type have been illustrated at 5.5 to 6 GHz.

Figure 6.48 indicates the final images for the inclusion positioned at 0°, 90°, 180° and 270° with employing summed symmetric differential artefact removal method.

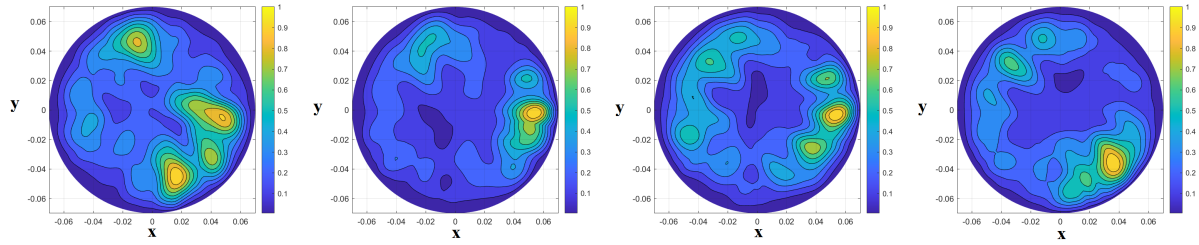

FIGURE 6.46: A combination of 5 transmitting position triplets for inclusion at 0°, 90°, 180° and 270°. Microwave images obtained using measured data with MWI device after performing artefact removal through local average subtraction artefact removal method at frequency 5.5 to 6 GHz. X and Y axes are in meters, while the intensity has an arbitrary unit.

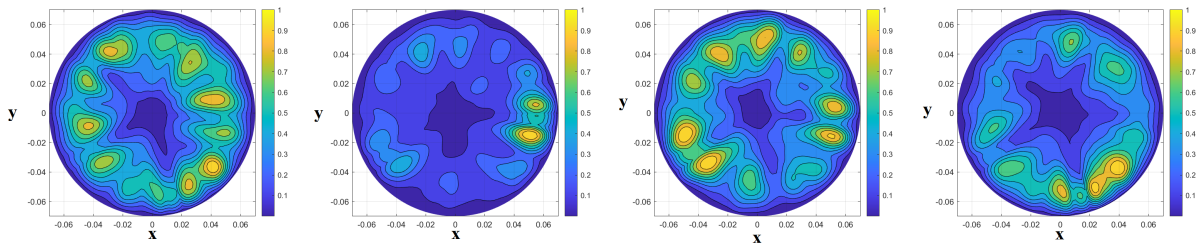

FIGURE 6.47: A combination of 5 transmitting position triplets for inclusion at 0°, 90°, 180° and 270°. Microwave images obtained using measured data with MWI device after performing artefact removal through differential symmetric receiver type artefact removal method at frequency 5.5 to 6 GHz. X and Y axes are in meters, while the intensity has an arbitrary unit.

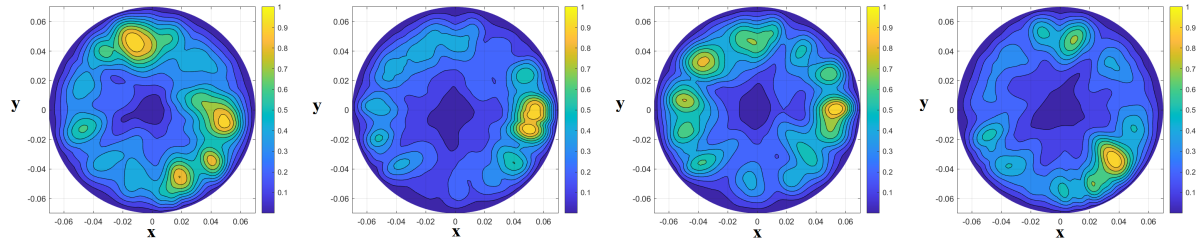

FIGURE 6.48: A combination of 5 transmitting position triplets for inclusion at 0°, 90°, 180° and 270°. Microwave images obtained using measured data with MWI device after performing artefact removal through summed symmetric differential artefact removal method at frequenct 5.5 to 6 GHz. X and Y axes are in meters, while the intensity has an arbitrary unit.

As it is obvious in the above images, the resulting images at frequency ranges of 1.5-4 GHz are including more clutters comparing to the resulting images obtained at frequency 1-1.5 GHz. From frequency range of 1.5 to 2 GHz to the higher frequency range of 3.5 to 4 GHz, the clutters have been observed more, thus the detection is getting less accurate. This is the reason why we have considered the frequency of 1 to 1.5 GHz for imaging the brain phantom. Now to continue to obtain the resulting images are obtained at frequency 1 to 1.5 GHz.

The tests have been performed by considering a combination of 5 transmitting position triplets and applying 5 artefact removal methods at frequency 1 to 1.5 GHz. For the measurements, Figure 6.49 illustrates the final normalised microwave image of such phantom with an inclusion. For this and all the subsequent figures, both x and y axes are in meters, while the intensity has an arbitrary unit. In fact, we apply the expression of subtraction artefact removal method "$S21^{\mathrm{rcstr,target}}_{np,\mathrm{tx}_1} - S21^{\mathrm{rcstr,notarget}}_{np,\mathrm{tx}_1}$", before performing imaging, with the aim of detecting the inclusion, the resulting image is shown in Figure 6.49. This figure is used as "Ideal" image for reference and comparisons (at frequency 1 to 1.5 GHz).

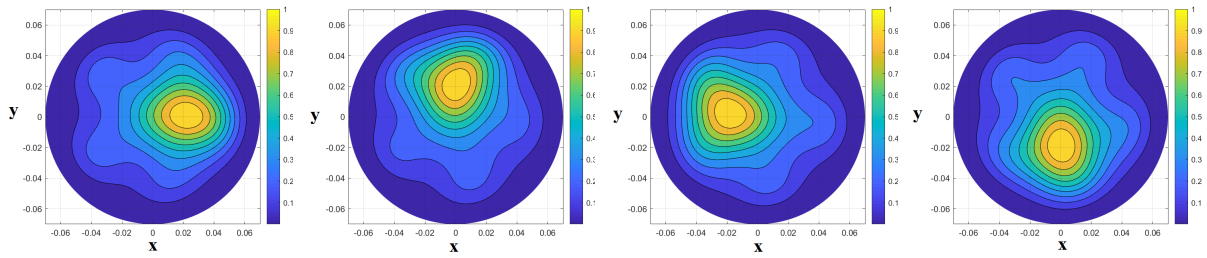

FIGURE 6.49: "Ideal" image generated by subtracting two sets of data of the phantom with no inclusion from the one with an inclusion (positioned at 0°, 90°, 180° and 270°) at frequency 1 to 1.5 GHz. X and Y axes are in meters, while the intensity has an arbitrary unit.

Figure 6.50 shows a combination of 5 transmitting position triplets for inclusion at 0°, 90°, 180° and 270°. The images are obtained after employing the rotation subtraction between two triplet positions, functioning as an artefact removal procedure at frequency 1 to 1.5 GHz.

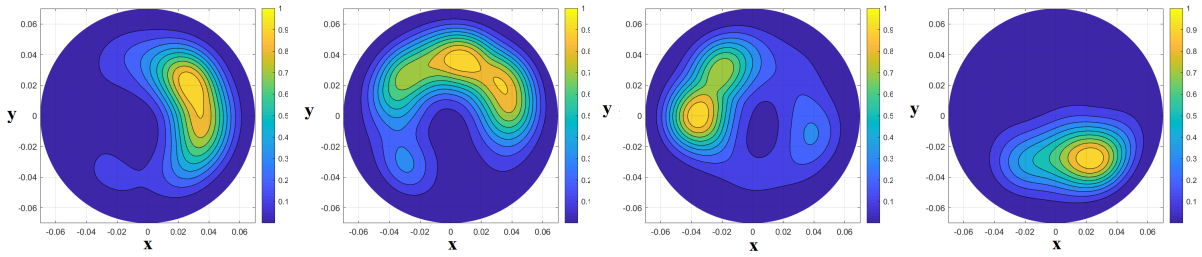

FIGURE 6.50: A combination of 5 transmitting position triplets for inclusion at 0°, 90°, 180° and 270°. Microwave images obtained using measured data with MWI device after performing artefact removal through rotation subtraction artefact removal method at frequenct 1 to 1.5 GHz. X and Y axes are in meters, while the intensity has an arbitrary unit.

Figure 6.51 presents the final images for inclusion at 0°, 90°, 180°, and 270°, using local average subtraction artefact removal method at 1 to 1.5 GHz.

In figure 6.52 the final images considering the positions of the inclusion at 0°, 90°, 180° and 270° with applying differential symmetric receiver type have been illustrated at 1 to 1.5 GHz.

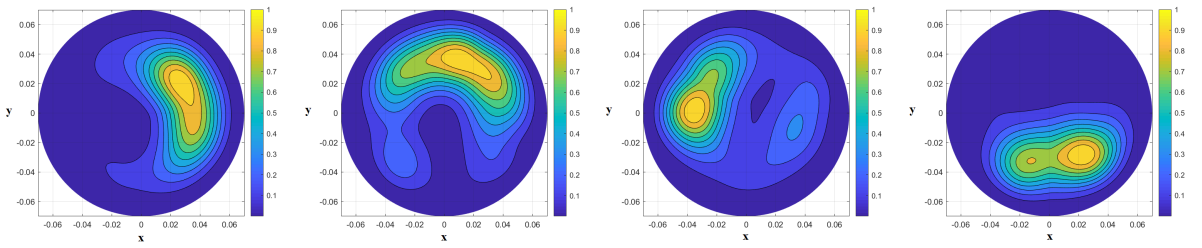

FIGURE 6.51: A combination of 5 transmitting position triplets for inclusion at 0°, 90°, 180° and 270°. Microwave images obtained using measured data with MWI device after performing artefact removal through local average subtraction artefact removal method at frequency 1 to 1.5 GHz. X and Y axes are in meters, while the intensity has an arbitrary unit.

Figure 6.53 indicates the final images for the inclusion positioned at 0°, 90°, 180° and 270° with employing summed symmetric differential artefact removal method.

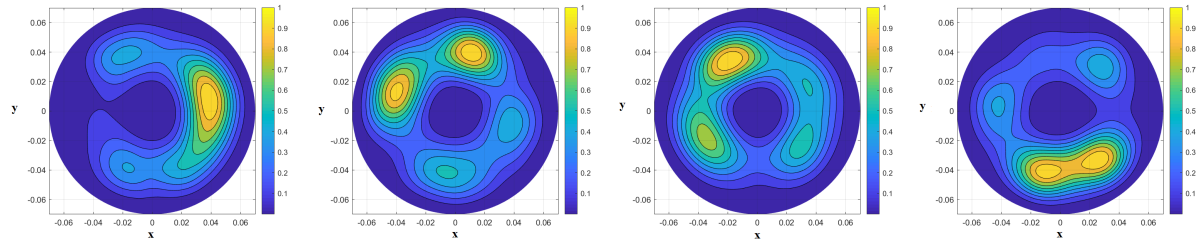

FIGURE 6.52: A combination of 5 transmitting position triplets for inclusion at 0°, 90°, 180° and 270°. Microwave images obtained using measured data with MWI device after performing artefact removal through differential symmetric receiver type artefact removal method at frequency 1 to 1.5 GHz. X and Y axes are in meters, while the intensity has an arbitrary unit.

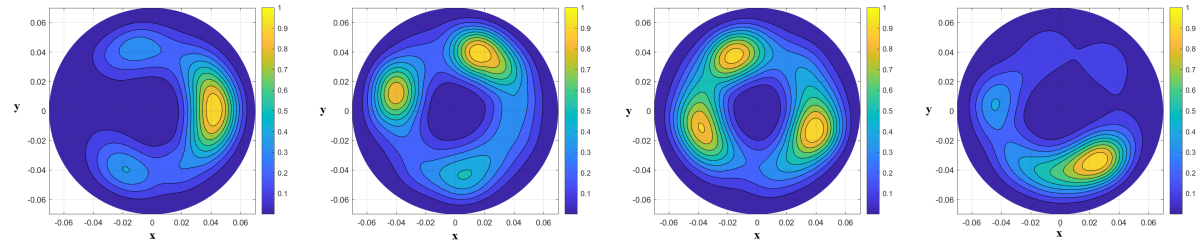

FIGURE 6.53: A combination of 5 transmitting position triplets for inclusion at 0°, 90°, 180° and 270°. Microwave images obtained using measured data with MWI device after performing artefact removal through summed symmetric differential artefact removal method at frequenct 1 to 1.5 GHz. X and Y axes are in meters, while the intensity has an arbitrary unit.

The imaging performance has been investigated through image quantification. With the aim of evaluating the impact of transmitting positions in achieving detection, here, the same as previous images, the S/C has been calculated for the obtained final images (from the combination of 5 transmitting position triplets at frequency 1 to 1.5 GHz). The correspondent S/C is given in Table 6.5 for all artefact removal methods. The methods are expressed in abbreviated form in Table 6.5.

TABLE 6.5: S/C (linear) for the frequency band between 1 to 1.5 GHz (using measurements data with MWI device and the rotation subtraction local average subtraction, differential symmetric receiver type, and summed symmetric differential type artefact removal method) and combining 5 triplets.

Positions	**RS**	**LAS**	**DSR**	**SSD**	**Ideal**
Position 0°	1.92	1.93	1.74	1.75	2.64
Position 90°	1.87	2.45	1.02	1.13	2.59
Position 180°	1.84	1.92	1.33	1.00	2.65
Position 270°	2.01	1.81	1.76	1.75	2.63
Average	1.91	2.03	1.46	1.41	2.62

It is important to mention that local average subtraction is considered for each triplet individually. The greater the value of S/C is, the higher the performance of the method is. To sum up our argument, here, the presented results in Tables 6.1, 6.2, 6.4, 6.5 and 6.6. Table 6.1 and 6.2 provide the values of S/C (linear) for the "Ideal" image obtained though subtraction and rotation subtraction artefact removal using simulated data have been discussed. Table 6.4 shows the values of S/C (linear) for measured data inside the anechoic chamber.

By comparing these three tables, we conclude that by applying the rotation subtraction artefact removal to both simulated and measured data (regardless of the method of measurements), a decrease in S/C can be observed with a minimum value of 1.48 (linear scale) for measurements inside the anechoic chamber. From Table 6.5 it can be concluded that the rotation subtraction and local average subtraction artefact removal methods are the best methods amongst the proposed artefact removal methods. The average S/C (linear) of four positions for local average subtraction and rotation subtraction are equal to 2.03 and 1.91, respectively.

The average S/C (linear) calculated for the "Ideal" artefact removal method at the frequency of 1-1.5 GHz with considering different positions of inclusion is equal to 2.62. The closest value to the value of "Ideal" method belongs to the value of local average subtraction method with 2.03. When employing different artefact removal methods to the measured data using MWI device, a decrease in S/C can be observed, with a minimum value of 1.41 (linear scale) related to summed symmetric differential method.

The images of ideal polyshape have been presented in Figure 6.54. It is important to mention that the ideal polyshape images are using ideal results obtained through subtraction artefact removal method and applying polyshape functions, as explained in Chapter 5.

Figures 6.55-6.58 indicate the results of polyshape images, which are obtained through using local average subtraction, rotation subtraction, differential symmetric receiver type, and summed symmetric differential artefact removal methods. Four different locations of the inclusion have been considered. In all four figures, x and y axes are in meters.

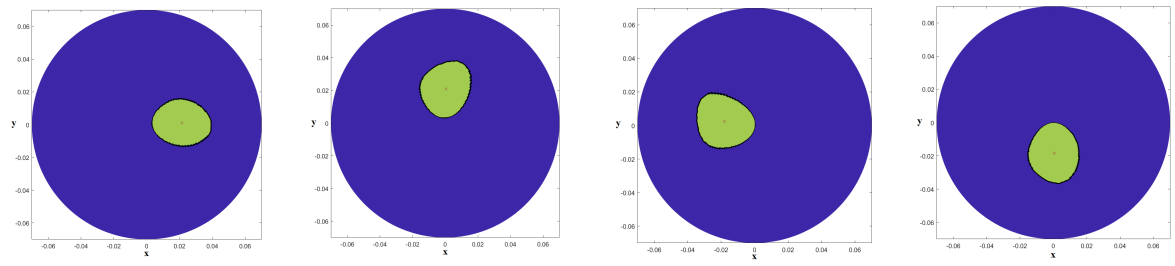

FIGURE 6.54: A combination of 5 transmitting position triplets for inclusion at 0°, 90°, 180° and 270°. Ideal polyshape image using measured data with MWI device at 1 to 1.5 GHz. X and Y axes are in meters.

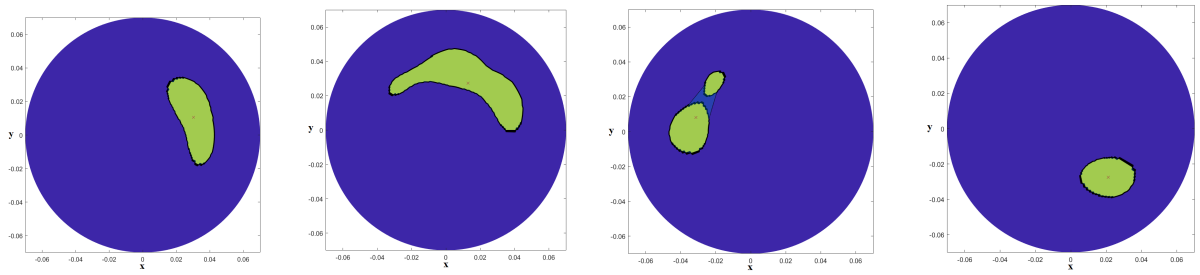

FIGURE 6.55: A combination of 5 transmitting position triplets for inclusion at 0°, 90°, 180° and 270°. Results polyshape images obtained using measured data with MWI device after performing artefact removal through rotation subtraction artefact removal method at frequency 1 to 1.5 GHz. X and Y axes are in meters.

Moreover, from the results above for both methods based on the symmetric nature of the head, it is worthwhile pointing out that the images which have used the symmetric methods may contain mirrored artefact (as shown in Figures 6.57 and 6.58). In Figures 6.59-6.62 the SSIM images have been shown using rotation subtraction, differential symmetric receiver type, and summed symmetric differential artefact removal methods. The inclusion has placed at four different positions.

Figures 6-59 to 6-62 show SSIM images which represent the similarity between the "Ideal" and reference (test) images with 1 meaning two images are completely same (an exact copy) and 0 meaning two images are totaly different (with no similarity). In SSIM images, dark areas are places where the structural difference is high and pale areas are places where the images are structurally similar.

The measurements have been performed using MWI device. Five different methods of artefact removal have been employed to remove the artefacts. The metrics are expressed in abbreviated form in Table 6.6. This table provides an accurate comparison between different artefact removal methods for the inclusion positioned at 0°, 90°, 180°, and 270°.

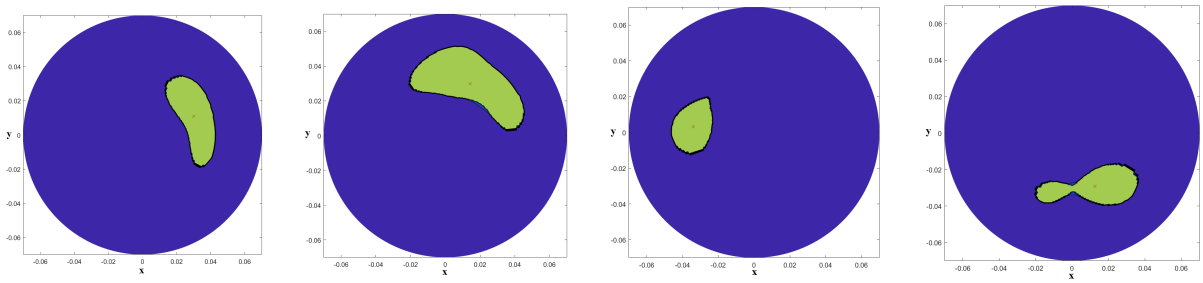

FIGURE 6.56: A combination of 5 transmitting position triplets for inclusion at 0°, 90°, 180° and 270°. Results polyshape images obtained using measured data with MWI device after performing artefact removal through local average subtraction artefact removal method at frequency 1 to 1.5 GHz. X and Y axes are in meters.

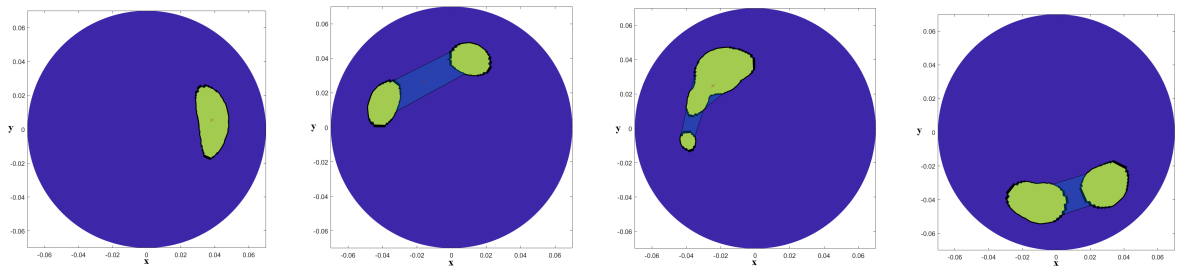

FIGURE 6.57: A combination of 5 transmitting position triplets for inclusion at 0°, 90°, 180° and 270°. Results polyshape images obtained using measured data with MWI device after performing artefact removal through differential symmetric receiver type artefact removal method at frequency 1 to 1.5 GHz. X and Y axes are in meters.

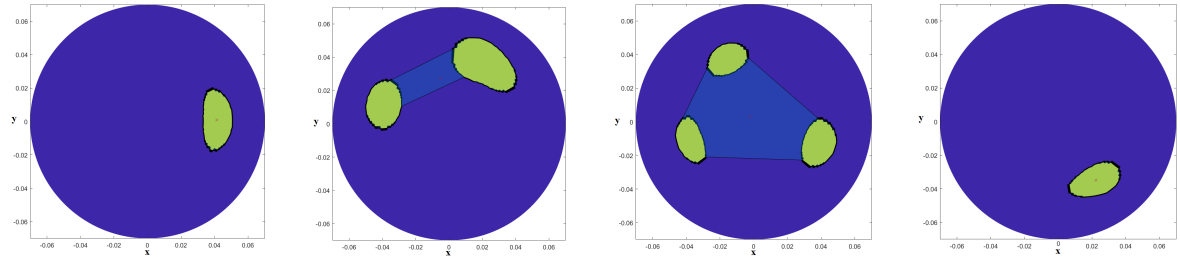

FIGURE 6.58: A combination of 5 transmitting position triplets for inclusion at 0°, 90°, 180° and 270°. Results polyshape images obtained using measured data with MWI device after performing artefact removal through summed symmetric differential artefact removal method at frequency 1 to 1.5 GHz. X and Y axes are in meters.

FIGURE 6.59: A combination of 5 transmitting position triplets for inclusion at 0°, 90°, 180° and 270°. SSIM images obtained using measured data with MWI device after performing artefact removal through rotation subtraction artefact removal method at frequency 1 to 1.5 GHz.

FIGURE 6.60: A combination of 5 transmitting position triplets for inclusion at 0°, 90°, 180° and 270°. SSIM images obtained using measured data with MWI device after performing artefact removal through local average subtraction artefact removal method at frequency 1 to 1.5 GHz.

FIGURE 6.61: A combination of 5 transmitting position triplets for inclusion at 0°, 90°, 180° and 270°. SSIM images obtained using measured data with MWI device after performing artefact removal through differential symmetric receiver type artefact removal method at frequency 1 to 1.5 GHz.

FIGURE 6.62: A combination of 5 transmitting position triplets for inclusion at 0°, 90°, 180° and 270°. SSIM images obtained using measured data with MWI device after performing artefact removal through summed symmetric differential artefact removal method at frequency 1 to 1.5 GHz.

TABLE 6.6: Artefact removal comparison.

Artefact removal methods	**ArD**	**CD**	**SNR**	**SSIM**
Rotation Subtraction	0.17	0.016	5.06	0.86
Local Average Subtraction	0.16	0.014	4.94	0.87
Differential Symmetric Receiver	0.21	0.020	4.53	0.84
Summed Symmetric differential	0.19	0.018	4.03	0.78

It is worth pointing out that for the sake of simplicity, the valid comparison is made using the average values of different inclusions positions in this table. In addition, the values are not absolute numbers and used to indicate to what extent the "Ideal" image is similar to the images obtained through different artefact removal methods.
The greater the values of SNR and SSIM and the lower ArD and CD are, the higher the performance of the method is. Ideally the SSIM, CD and ArD should be equal to one, zero and zero, respectively. From the obtained results shown in Table 6.6, we can conclude that the Local average subtraction and rotation subtraction are the best approaches to suppress artefacts, i.e. to reduce the clutter. Based on the achieved results, the highest values of SNR and SSIM and the lowest values of CD and ArD are obtained when employing the Rotation subtraction and Local average subtraction artefact removal methods.

More in detail, as given in Table 6.6, the maximum SSIM value belongs to Local average subtraction with 0.87 whilst, the maximum SNR is allocated to the rotation subtraction method with 5.06. It has also been concluded that the lowest values of both CD and ArD belong to Local average subtraction method with 0.014 (metres) and 0.16, respectively. It follows that the use of the Local average subtraction and rotation subtraction artefact removal methods in realistic scenario can be helpful to reduce artefacts.

Moreover, it is important to highlight that the results show that the position of the inclusion can vastly influence the resulting image, with every artefact removal method exhibiting differences in image quality, when the inclusion was moved. When the inclusion is positioned at 90°, with applying the summed symmetric differential and differential symmetric receiver methods, all images show a symmetric split inclusion image. This might be due to the direct fields and the fields reflected by the first layer, the same thing happens at position 180° when using the rotation subtraction, summed symmetric differential and differential symmetric receiver methods, and at position 270° when applying the local average subtraction and differential symmetric receiver methods, as shown in Figures 6.10-6.13. The results shown in this thesis, achieved through measurements using MWI device, pave the way towards the validation of the reliable artefact removal methods.

It should be noted that the artefact removal methods have been employed to suppress artefacts, i.e. the image of the transmitter and the reflections of the layers. However, it may happen that even beyond artefact removal, the residual clutter masks the inclusion, as can be seen in Figures 6.7, and 6.8 (probably due to residual clutter). Residual clutter is due to the imperfect cancelation of the transmitting antenna or inappropriate cancelation of the first layer reflection or even due to multiple reflections occurring inside the phantom that cannot be canceled completely.

6.3 Summary

In this chapter the results which can validate the hypothesis that HP-based MWI may be successfully used to detect a haemorrhagic stroke inclusion in both anthropomorphic simulation and in a multi-layered phantom, were presented. Also, the relative permittivity (ε_r) and conductivity S/m of the brain and blood clot (representing the brain haemorrhagic stroke) tissues, were presented in the corresponding table, in order to draw a comparison between the real (which has been presented in Chapter 2) and the fabricated tissues. Five artefact removal methods were applied to suppress artefact, i.e. to reduce the clutter.

Then, in order to quantify the detection capabilities of the imaging, five metrics were introduced and calculated. The images through simulation, obtained using both subtraction and rotation subtraction artefact removal methods, were presented in this chapter. Moreover, the images through measurements were presented, once obtained from measurements inside the anechoic chamber, and then by using MWI device. It is worth noting that for both procedures of the measurements, only the rotation subtraction artefact removal method was used to remove the artefact. The local average substraction, differential symmetric receiver type, and summed symmetric differential artefact removal methods are applied to the data obtained from measurements through MWI device. Furthermore, the correspondent metrics for each image and artefact removal methods were given in this chapter and the conclusion will be discussed through next chapter.

Chapter 7

Conclusions and Proposed Future Work

7.1 Conclusions

In this work, we simulated, fabricated and used WB antennas and employed a HP-based MWI technique to detect haemorrhagic stroke in multi-layered head phantoms. The capability of HP-based microwave imaging to detect bone lesions was first demonstrated through phantom measurements in an anechoic chamber. In addition, we have successfully demonstrated a promising new application for a MWI device (based on HP) which has been previously used for breast imaging through phantom measurements [33], and verified in preliminary clinical trials [23]. We have adapted the methods used to detect breast cancer and have produced promising research using the technology for brain stroke detection. The detailed description of MWI device has been given in Section 4.4.2. A multi-layered phantom mimicking human head with a brain haemorrhage has been realised, applying millimetric cylindrically shaped inclusion to emulate a haemorrhagic brain stroke. For each transmitting and receiving positions, the complex S21 is collected from 1 to 6 GHz, with 5 MHz sampling. Then during running the codes, we will consider the frequency of 1 to 1.5 GHz, as this band has demonstrated to be ideal and optimal to do brain imaging [8]. The tests have been performed by considering a combination of 5 transmitting position triplets for inclusion at 0°, 90°, 180° and 270°.

The simplicity of HP obviates the need for finding a solution to inverse problems when forward propagating the waves. Additionally, the methodology of HP allows capturing the contrast such that different material properties within the region of interest could be detected in the final image. Through both simulation and measurements, it has been verified that the field reconstructed in the medium under test will display a mismatch around the transition region of the two media, which is where the target is positioned. This mismatch permits detection. The haemorrhagic stroke detection has been achieved both in simulation and measurements, after using appropriate artefact removal algorithms to pre-process the signals.

A wide spectrum of current artefact removal algorithms, coupled with algorithms altered from ground penetrating radar applications, are provided for comparison with a variety of suitable performance metrics [98]. The methods of artefact removal used in this work were basically derived from the literature of [23],[77],[96]-[98].

Five different subtraction artefact removal method has been employed here to suppress artefact, i.e. to reduce the clutter. The images are obtained after employing each artefact removal methods for a same set of positions (i.e. doublet for measurements inside the anechoic chamber and triplet for measurements through MWI device), functioning as an artefact removal procedure. The brain haemorrhage was successfully detected for all positions.

The subtraction of the data between a healthy head model and a head model with haemorrhagic stroke has been employed in simulation and measurements. It is worthwhile pointing out that, in a realistic scenario, subtraction artefact removal can not be employed. Practically, subtraction artefact removal method may only be applied to simulation data, whilst other artefact removal methods can be applied to both simulation and measurements data. In clinical trials, there is no possibility of having a human head with stroke and the same human head without stroke (for subtracting them from each other). We use this method for the simulation data to show the strong feasibility of detecting the brain haemorrhage in an ideal way. This "Ideal" image is performed as a reference for the comparison with the resulting image from other artefact removal methods.

As a portion of this study, the calculation of the dedicated parameters will require to be constructed to assess the stroke detection capability and to allow performing a quantification of detection accuracy. These metrics evaluate the accuracy and strength of the results and would be highly effective to employ in comparisons in this study. For this purpose, the parameters are as follows:

- Polyshape Construction
- Area Difference (ArD)
- Centroid Difference (CD)
- Signal-to-Noise Ratio (SNR)
- Structural Similarity Index Metric (SSIM)
- Signal-to-clutter ratio (S/C)

These parameters have been discussed through Chapter 5. It is worth pointing out that all the metrics are calculated for each image, considering all artefact removal methods. The imaging

performance has been investigated through image quantification. The correspondent S/C is given in Chapter 6.

Regarding S/C, the highest value of S/C is obtained when employing the subtraction of the data between a healthy head model and a head model with haemorrhagic stroke (for "Ideal" images). More in detail, the maximum S/C value is 2.5 (linear scale). When employing the rotation subtraction artefact removal to both simulated and measured data, a decrease in S/C can be observed, with a minimum value of 1.48 (linear scale) for measurements inside the anechoic chamber. Also, the same strategy occurs when using the data obtained from MWI device with a minimum values of 1.91 and 2.03 through applying rotation subtraction and local average subtraction, respectively.

Although, a decrease in S/C can be observed through using the local average subtraction and rotation subtraction artefact removal methods, the stroke position is still clearly indicated. The primary goal of this work was to exhibit a procedure resulting in the fabrication of a prototype system for detecting the stroke. Recently, various system prototypes using microwaves for brain stroke diagnostics have been suggested. One example is the "Stroke-finder", developed at Chalmers University [54], which detects and classifies different types of intracranial bleedings (ischemic or haemorrhagic). The device is comprised of 12 Tx/Rx triangular patch antennas fixed on a helmet made of plastic. The plastic balloons filled with water, between the head and the patch antennas, are used to act as matching medium.

Another system, the "BRIM G2" has been developed at EMTensor [56] for brain imaging. This system is comprised of 177 rectangular ceramic-loaded waveguide antennas fixed on a hemi-spherical stainless-steel chamber. The antennas are spaced evenly at eight rings, with different heights. Moreover, these rectangular antennas are operating at 1 GHz. The matching medium used in this system is a glycerine-water mixture.The third prototype system is the one fabricated at Queensland University for imaging intracranial haematomas [60]. This system is comprised of a ring of 16 tapered and corrugated slot antennas, which operate from 1 to 4 GHz. The antennas are in air, without the use of a matching medium. The stroke imaging only relies on the monostatic data (i.e., the reflection coefficient at each antenna).

Compared to existing head imaging systems described earlier [9],[20],[21],[54],[60], the proposed procedure may be considered a practical alternative to array antennas, due to lower complexity. Specifically, it requires a very simple hardware setup, i.e. one transmitting antenna and one receiving antenna (coupled through a VNA) which rotate in free space around the object to collect the signal in a multi-bistatic fashion. The proposed procedure resorts to HP to detect the variation in dielectric properties between the healthy head tissues and the haemorrhagic stroke. The dielectric properties of the materials used in this work are a good resemblance of

the head tissue properties. The relative permittivity used in the Green's function of Equation (5.1) has been set to $\sqrt{44.75} \cong 6.7$ in order to meet the impedance matching requirements [106]. In simulations, detection has been achieved both using the subtraction artefact removal and the rotation subtraction artefact removal procedure. In measurements inside the anechoic chamber, only the rotation subtraction artefact removal procedure has been used. In measurements through MWI device, all the artefact removal methods have been used, being the more realistic case in first aid scenario.

As highlighted in the resulting images presented in Chapter 6, detection through measurements is achieved at four different phantom orientations. The results shown in this work, obtained through simulation and measurements both inside the anechoic chamber and through MWI device, pave the way towards the construction and use of a low complexity MWI device for haemorrhagic brain stroke detection, where antennas operate in free-space. The device [107] will be portable, allowing a pre-hospital use. The device will be constituted of two antennas operating in air, embedded in an appropriate cavity, which may have a cylindrically-shaped section. A cavity with a hole which will permit the insertion of the patient's head, lying in supine position, such as in emergency units. The physical appearance of the device can be derived from Figure 7.1. The antennas will rotate around the head and measure electromagnetic fields in multi-bistatic fashion from different transmitting and receiving positions. In more detail, the MWI device allows to illuminate the head of the patient using electromagnetic fields in the microwave band, with aim of measuring the correspondent scattered electromagnetic fields and processing the measured field to obtain an image. Moreover, the safety aspect is a great challenge which developers of medical imaging devices need to face. The patients are in complete safety, as the connected antennas to the dedicated VNA, are operating with very low input power (mW). Another significant aspect that should be considered here is the estimated cost of the device. The estimated cost may be in the range of tens of thousands of Euros. Finally, the clinical trials on patients with hyperacute stroke will be soon activated to assess the capability of the MWI device to detect patients with haemorrhagic strokes. Figure 7.1 presents the physical appearance and dimensions of the device for haemorrhagic brain stroke detection.

Finally, by visually comparing the result images and the metrics, It has been concluded that the rotation subtraction and local average subtraction artefact removal methods are the best approaches for removing the artefact.

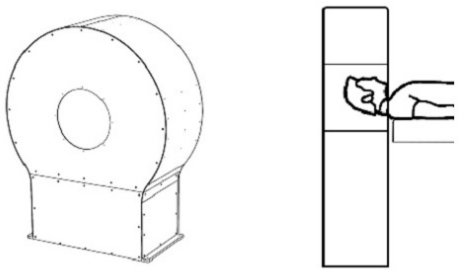

FIGURE 7.1: The physical appearance and the dimensions of the device for haemorrhagic brain stroke detection.

7.2 Contributions

- A research study of the MWI based brain stroke detection is carried out. A brain haemorrhage model is proposed and simulated using CST Microwave software. This brain phantom is then measured using the antenna pair based multi-bistatic imaging system, with the microwave images created to indicate the stroke location. To my best knowledge, similar research has never been implemented. The results show that a brain stroke can be detected using the MWI approach.

- A microstrip patch antenna with fractal ground plane is proposed, simulated and fabricated in-house at London South Bank University (LSBU). The microstrip patch antenna operates as a brain haemorrhage detector with the advantage of operating between 1 and 2 GHz, as this band has shown to be optimal for brain imaging. Therefore, a WB antenna which works efficiently across that band is a vital factor on the success of the suggested system. We have proposed an effective technique for increasing the bandwidth of the antenna and subsequently a better head image through designing an isosceles triangular patch antenna using fractal ground plain.

- A plain hemi-ellipsoidal human head phantom and a haemorrhagic brain stroke phantom are proposed, simulated and fabricated for experimental studies.

- The antenna setup is designed and proposed employing only two microstrip patch antennas. These two antenna configurations are then used to measure the human head phantom, with the simulated and measured signals recorded and analysed.

- A low complexity MWI procedure for brain imaging has been proposed by applying HP based MWI technique and signal processing techniques.

- The signal processing techniques applicable to several strokes and cancers detection are proposed and applied to the scattering signals received. The local average subtraction and rotation subtraction artefact removal methods are able to remove unwanted parts of the signals and suppress artefacts, i.e. to reduce the clutter. Compared with the traditional clutter removal technique, the proposed technique does not require a reference head phantom, and therefore can be applied in clinical work.

- The antenna configuration based microwave image is created to indicate the brain haemorrhage position. A haemorrhagic stroke with circular cross-sectional radius of 5 mm and a height of 35 mm is situated inside the brain mould. The brain haemorrhage is clearly detected in different positions. Different types of microstrip antenna have been designed and compared. These antennas are then used for gathering both simulation and experimental results. Although, a decrease in S/C can be observed through using rotation subtraction artefact removal method, the stroke position is still clearly indicated.

- The main aim of this work was to propose a portable detection system for diagnosis of various emergency circumstances.

7.3 Challenges and Recommendations for Future Work

The following possible topics are discussed for further investigation.

7.3.1 The Brain Stroke Phantom

The human head phantom is simulated and fabricated on the basis of the CST and tissue-mimicking approaches. The detailed study of stroke has been discussed in Chapter 2, which is also consisted of the stroke types. The haemorrhagic stroke has been studied, simulated and fabricated in this thesis. Distinguishing between different sorts of stroke (i.e. ischemic stroke and haemorrhagic stroke) should be the next area to be investigated. This study and research requires a long time to be investigated. Hence, the next step is to design and fabricate a realistic phantom of the brain ischemic stroke and perform a procedure resulting in distinguishing between different sorts of stroke. This target should not be difficult to be achieved and discriminated in simulation but distinguishing it through measurements or on real patients is definitely more complicated.

7.3.2 Imaging System Design

In this thesis, the antenna is connected to the VNA, with the scattering signals measured. The use of the VNA simplifies the design of multi-bistatic imaging system. However, the disadvantages of the VNA include its high cost and heavy weight.

As, we discussed in Section 7.3.1, some of the studies such as the discrimination between ischemic stroke and haemorrhagic stroke have only been carried out by simulation so far. Practical experimental work is still required.

7.3.3 Final Comment

Today's high incidence of stroke requires effective, low cost, diagnostic methods which are safe, portable and comfortable for patients to detect stroke. The MWI based stroke detection method can be an attractive solution to satisfy all of these requirements. Currently, this type of emerging technology has not been fully studied and the mainstream clinical stroke diagnostic methods are still CT-Scan, and MRI. No doubt it would generally be advantageous to apply Near-infrared spectroscopy (NIRS) in CT-Scan, and MRI. NIRS is a technology that continuously monitors regional tissue oxygenation. Originally used for assessment of oxygen saturation of the brain, its use has now been expanded to evaluation of oxygenation of tissues other than the brain. There is also growing evidence for the larger applicability of NIRS as an estimate of systemic venous saturation in correspondence with the adequacy of the circulatory status. NRIS has the advantages of:
- Being a portable ana inexpensive device for functional neuroimaging comparable to EEG, as opposed to fMRI, PET and MEG,
- It does not require severely limiting subject motion,
- It is a non-invasive measure using laser or incoherent light sources that are typically safer than laser pointers,
- It can provide quantitative measures of the changes in oxygenated and deoxygenated hemoglobin that can help resolve ambiguities in the effects of the blood flow and oxygen consumption responses to brain activation.
- It can measure these hemodynamic signals with a temporal resolution of 100 Hz or higher, significantly greater than fMRI or PET aiding in the resolution of the onset time of brain activation and in filtering physiological interference from the brain activation signals of interest.
- Finally, NIRS is compatible with fMRI, PET, MEG, EEG enabling interference free simultaneous multi-modal studies of brain activation.
However, NIRS is limited by depth sensitivity which in adult humans typically reaches 5 to 10

millimeters beneath the inner surface of the skull for brain activation. Also, spatial resolution is limited by the ill-conditioned inverse tomography problem. Most studies do not employ overlapping measurements and thus lateral resolution is approximately equal to the source-detector separation. Lateral spatial resolution can be improved by a factor of 2 or more by incorporating overlapping measurements.
Depth resolution within the brain, however, is challenged by the lack of transmission measurements through the head. The limited lateral and depth spatial resolution causes a partial volume issue that results in underestimating changes in the hemoglobin concentrations. Similar to EEG, care must be taken to insure hair does not severely block the transmission of light between the source and detector and the scalp, although conductive paste is not necessary as is the case for EEG. Whilst subjects are less physically constrained than for fMRI, PET, and MEG, care must still be taken to secure the optical probe on the head of the subject to minimize motion artifacts [108].

To summarise, in this thesis, several techniques to contribute to the study of MWI based stroke detection have been proposed and developed. It is hoped that future will see the wide use of this potential stroke detection method in our daily lives.

Bibliography

[1] Feigin, V.L., 2005. Stroke epidemiology in the developing world. The Lancet, 9478(365), pp.2160-2161.
[2] World Health Organization, 2007. The World Health Report 2004. Changing history. Geneva, Switzerland: World Health Organization, 2004.
[3] Lutz, W., Sanderson, W. and Scherbov, S., 1997. Doubling of world population unlikely. Nature, 387(6635), pp.803-805.
[4] Strong, K., Mathers, C. and Bonita, R., 2007. Preventing stroke: saving lives around the world. The Lancet Neurology, 6(2), pp.182-187.
[5] Zasler, N.D., Katz, D.I. and Zafonte, R.D. eds., 2012. Brain injury medicine: principles and practice. Demos Medical Publishing.
[6] Jauch, E.C., Saver, J.L., Adams Jr, H.P., Bruno, A., Connors, J.J., Demaerschalk, B.M., Khatri, P., McMullan Jr, P.W., Qureshi, A.I., Rosenfield, K. and Scott, P.A., 2013. Guidelines for the early management of patients with acute ischemic stroke: a guideline for healthcare professionals from the American Heart Association/American Stroke Association. Stroke, 44(3), pp.870-947.
[7] Kuhl, C.K., Schrading, S., Leutner, C.C., Morakkabati-Spitz, N., Wardelmann, E., Fimmers, R., Kuhn, W. and Schild, H.H., 2005. Mammography, breast ultrasound, and magnetic resonance imaging for surveillance of women at high familial risk for breast cancer. Journal of clinical oncology, 23(33), pp.8469-8476.
[8] Ireland, D. and Bialkowski, M.E., 2011. Microwave head imaging for stroke detection. Progress In Electromagnetics Research, 21, pp.163-175.
[9] Vasquez, J.A.T., Scapaticci, R., Turvani, G., Dassano, G., Joachimowicz, N., Duchene, B., Casu, M.R., Crocco, L. and Vipiana, F., 2018, September. First experimental assessment of a microwave imaging prototype for cerebrovascular diseases monitoring. In 2018 International Conference on Electromagnetics in Advanced Applications (ICEAA) (pp. 400-401). IEEE.
[10] Mohammed, B.J., Abbosh, A.M., Mustafa, S. and Ireland, D., 2013. Microwave system for head imaging. IEEE Transactions on Instrumentation and Measurement, 63(1), pp.117-123.
[11] Semenov, S., 2009. Microwave tomography: review of the progress towards clinical applications. Philosophical Transactions of the Royal Society A: Mathematical, Physical and Engineering Sciences, 367(1900), pp.3021-3042.

[12] Gabriel, C., Gabriel, S. and Corthout, Y.E., 1996. The dielectric properties of biological tissues: I. Literature survey. Physics in medicine & biology, 41(11), p.2231.
[13] Gabriel, S., Lau, R.W. and Gabriel, C., 1996. The dielectric properties of biological tissues: II. Measurements in the frequency range 10 Hz to 20 GHz. Physics in medicine & biology, 41(11), p.2251.
[14] Mobashsher, A.T., Mohammed, B.J., Mustafa, S. and Abbosh, A., 2013, December. Ultra wideband antenna for portable brain stroke diagnostic system. In 2013 IEEE MTT-S International Microwave Workshop Series on RF and Wireless Technologies for Biomedical and Healthcare Applications (IMWS-BIO) (pp. 1-3). IEEE.
[15] Merunka, I., Fiser, O., Vrba, D. and Vrba, J., 2018, April. Numerical analysis of microwave tomography system for brain stroke detection. In 2018 28th International Conference Radioelektronika (RADIOELEKTRONIKA) (pp. 1-4). IEEE.
[16] Coli, V.L., Tournier, P.H., Dolean, V., El Kanfoud, I., Pichot, C., Mialiaccio, C. and Blanc-Feraud, L., 2018, July. Detection of brain strokes using microwave tomography. In 2018 IEEE International Symposium on Antennas and Propagation & USNC/URSI National Radio Science Meeting (pp. 223-224). IEEE.
[17] Klemm, M., Leendertz, J.A., Gibbins, D., Craddock, I.J., Preece, A. and Benjamin, R., 2010. Microwave radar-based differential breast cancer imaging: Imaging in homogeneous breast phantoms and low contrast scenarios. IEEE Transactions on Antennas and Propagation, 58(7), pp.2337-2344.
[18] Ahsan, S., Koutsoupidou, M., Razzicchia, E., Sotiriou, I. and Kosmas, P., 2019, March. Advances towards the Development of a Brain Microwave Imaging Scanner. In 2019 13th European Conference on Antennas and Propagation (EuCAP) (pp. 1-4). IEEE.
[19] Ricci, E., Di Domenico, S., Cianca, E. and Rossi, T., 2015, August. Artifact removal algorithms for stroke detection using a multistatic MIST beamforming algorithm. In 2015 37th Annual International Conference of the IEEE Engineering in Medicine and Biology Society (EMBC) (pp. 1930-1933). IEEE.
[20] Wang, F., 2017. Assembly conformal antenna array for wearable microwave breast imaging application.
[21] Scapaticci, R., Tobon, J., Bellizzi, G., Vipiana, F. and Crocco, L., 2018. Design and numerical characterization of a low-complexity microwave device for brain stroke monitoring. IEEE Transactions on Antennas and Propagation, 66(12), pp.7328-7338.
[22] Sani, L., Ghavami, N., Vispa, A., Paoli, M., Raspa, G., Ghavami, M., Sacchetti, F., Vannini, E., Ercolani, S., Saracini, A. and Duranti, M., 2019. Novel microwave apparatus for

breast lesions detection: Preliminary clinical results. Biomedical Signal Processing and Control, 52, pp.257-263.
[23] Vispa, A., Sani, L., Paoli, M., Bigotti, A., Raspa, G., Ghavami, N., Caschera, S., Ghavami, M., Duranti, M. and Tiberi, G., 2019. UWB device for breast microwave imaging: phantom and clinical validations. Measurement, 146, pp.582-589.
[24] Ghavami, N., Tiberi, G., Ghavami, M., Dudley, S. and Lane, M., 2016, July. Huygens principle based UWB microwave imaging method for skin cancer detection. In 2016 10th International Symposium on Communication Systems, Networks and Digital Signal Processing (CSNDSP) (pp. 1-4). IEEE.
[25] Elahi, M.A., Glavin, M., Jones, E. and O'Halloran, M., 2013. Artifact removal algorithms for microwave imaging of the breast. Progress In Electromagnetics Research, 141, pp.185-200.
[26] Pancera, E., 2010, November. Medical applications of the Ultra Wideband technology. In 2010 Loughborough Antennas & Propagation Conference (pp. 52-56). IEEE.
[27] Nilavalan, R., Leendertz, J., Craddock, I.J., Benjamin, R. and Preece, A., 2005. Breast tumour detection using a flat 16 element array. EMC Zurich.
[28] Standring, S., 2016. Gray's Anatomy (41tst ed.).
[29] Lillie, E.M., Urban, J.E., Lynch, S.K., Weaver, A.A. and Stitzel, J.D., 2016. Evaluation of skull cortical thickness changes with age and sex from computed tomography scans. Journal of Bone and Mineral Research, 31(2), pp.299-307.
[30] WikiJournal of Medicine/Medical gallery of Blausen Medical 2014. (2020, July 17). Wikiversity.Retrieved 00:28, July 17, 2020 from https://en.wikiversity.org/w/index.php.
[31] World Health Organization, 2002. The world health report 2002: reducing risks, promoting healthy life. World Health Organization.
[32] Sacco, R.L., Kasner, S.E., Broderick, J.P., Caplan, L.R., Connors, J.J., Culebras, A., Elkind, M.S., George, M.G., Hamdan, A.D., Higashida, R.T. and Hoh, B.L., 2013. An updated definition of stroke for the 21st century: a statement for healthcare professionals from the American Heart Association/American Stroke Association. Stroke, 44(7), pp.2064-2089.
[33] Kim, A.S., Cahill, E. and Cheng, N.T., 2015. Global stroke belt: geographic variation in stroke burden worldwide. Stroke, 46(12), pp.3564-3570.
[34] Mozaffarian, D., Benjamin, E.J., Go, A.S., Arnett, D.K., Blaha, M.J., Cushman, M., De Ferranti, S., Despres, J.P., Fullerton, H.J., Howard, V.J. and Huffman, M.D., 2015. Executive summary: heart disease and stroke statistics-2015 update: a report from the American Heart Association. Circulation, 131(4), pp.434-441.

[35] Bejot, Y., Benatru, I., Rouaud, O., Fromont, A., Besancenot, J.P., Moreau, T. and Giroud, M., 2007. Epidemiology of stroke in Europe: geographic and environmental differences. Journal of the neurological sciences, 262(1-2), pp.85-88.
[36] Lawrence, E.S., Coshall, C., Dundas, R., Stewart, J., Rudd, A.G., Howard, R. and Wolfe, C.D., 2001. Estimates of the prevalence of acute stroke impairments and disability in a multiethnic population. Stroke, 32(6), pp.1279-1284.
[37] Langhorne, P., Bernhardt, J. and Kwakkel, G., 2011. Stroke rehabilitation. The Lancet, 377(9778), pp.1693-1702.
[38] Connolly Jr, E.S., Rabinstein, A.A., Carhuapoma, J.R., Derdeyn, C.P., Dion, J., Higashida, R.T., Hoh, B.L., Kirkness, C.J., Naidech, A.M., Ogilvy, C.S. and Patel, A.B., 2012. Guidelines for the management of aneurysmal subarachnoid hemorrhage: a guideline for healthcare professionals from the American Heart Association/American Stroke Association. Stroke, 43(6), pp.1711-1737.
[39] Thrane, N., Steffensen, F.H., Mortensen, J.T., SCHONHEYDER, H.C. and SORENSEN, H.T., 1999. A population-based study of antibiotic prescriptions for Danish children. The pediatric infectious disease journal, 18(4), pp.333-337.
[40] Sondergaard, C., Skajaa, E. and Henriksen, T.B., 2000. Fetal growth and infantile colic. Archives of Disease in Childhood-Fetal and Neonatal Edition, 83(1), pp.F44-F47.
[41] Olesen, C., Sondergaard, C., Thrane, N., Nielsen, G.L., de Jong-van den Berg, L. and Olsen, J., 2001. Do pregnant women report use of dispensed medications. Epidemiology, 12(5), pp.497-501.
[42] Gregersen, H., Ibsen, J.S., Mellemkjoer, L., Dahlerup, J.F., Olsen, J.H. and Sorensen, H.T., 2001. Mortality and causes of death in patients with monoclonal gammopathy of undetermined significance. British journal of haematology, 112(2), pp.353-357.
[43] Headway / about brain injury from https://www.headway.org.uk/about-brain-injury/individuals/types-of-brain-injury/stroke/.
[44] O'donnell, M.J., Xavier, D., Liu, L., Zhang, H., Chin, S.L., Rao-Melacini, P., Rangarajan, S., Islam, S., Pais, P., McQueen, M.J. and Mondo, C., 2010. Risk factors for ischaemic and intracerebral haemorrhagic stroke in 22 countries (the INTERSTROKE study): a case-control study. The Lancet, 376(9735), pp.112-123.
[45] Jensen, E.S., Lundbye-Christensen, S., Samuelsson, S., Sorensen, H.T. and Schonheyder, H.C., 2004. A 20-year ecological study of the temporal association between influenza and meningococcal disease. European journal of epidemiology, 19(2), pp.181-187.
[46] Lazebnik, M., McCartney, L., Popovic, D., Watkins, C.B., Lindstrom, M.J., Harter, J., Sewall, S., Magliocco, A., Booske, J.H., Okoniewski, M. and Hagness, S.C., 2007. A

large-scale study of the ultrawideband microwave dielectric properties of normal breast tissue obtained from reduction surgeries. Physics in medicine & biology, 52(10), p.2637.
[47] Gabriel, C., 1996. Compilation of the dielectric properties of body tissues at RF and microwave frequencies. King's Coll London (United Kingdom) Dept of Physics.
[48] Soffietti, R., Baumert, B.G., Bello, L., Von Deimling, A., Duffau, H., Frenay, M., Grisold, W., Grant, R., Graus, F., Hoang-Xuan, K. and Klein, M., 2010. Guidelines on management of low-grade gliomas: report of an EFNS-EANO Task Force. European Journal of Neurology, 17(9), pp.1124-1133.
[49] Strokeforum from https://www.strokeforum.com/acute-stroke-management/imaging-in-stroke.
[50] Tahir, M.N., 2018. Classification and characterization of brain tumor MRI by using gray scaled segmentation and DNN.
[51] Sarafianou, M., Gibbins, D.R., Craddock, I.J., Klemm, M., Leendertz, J.A., Preece, A. and Benjamin, R., 2010, April. Breast surface reconstruction algorithm for a multi-static radar-based breast imaging system. In Proceedings of the Fourth European Conference on Antennas and Propagation (pp. 1-5). IEEE.
[52] Meaney, P.M., Fanning, M.W., Li, D., Poplack, S.P. and Paulsen, K.D., 2000. A clinical prototype for active microwave imaging of the breast. IEEE Transactions on Microwave Theory and Techniques, 48(11), pp.1841-1853.
[53] Zhurbenko, V., 2011. Challenges in the design of microwave imaging systems for breast cancer detection. Advances in Electrical and Computer Engineering, 11(1), pp.91-96.
[54] Candefjord, S., Winges, J., Malik, A.A., Yu, Y., Rylander, T., McKelvey, T., Fhager, A., Elam, M. and Persson, M., 2017. Microwave technology for detecting traumatic intracranial bleedings: tests on phantom of subdural hematoma and numerical simulations. Medical & biological engineering & computing, 55(8), pp.1177-1188.
[55] Stroke Finder, projects, 08 March 2017, (01/January/2011- 31/ December/ 2014), from https://www.chalmers.se/en/projects/Pages/Strokefinder.aspx.
[56] Hopfer, M., Planas, R., Hamidipour, A., Henriksson, T. and Semenov, S., 2017. Electromagnetic Tomography for Detection, Differentiation, and Monitoring of Brain Stroke: A Virtual Data and Human Head Phantom Study. IEEE Antennas and Propagation Magazine, 59(5), pp.86-97.
[57] Bonazzoli, M., Dolean, V., Graham, I., Spence, E. and Tournier, P.H., 2019. Domain decomposition preconditioning for the high-frequency time-harmonic Maxwell equations with absorption. Mathematics of Computation, 88(320), pp.2559-2604.

[58] Sill, J.M. and Fear, E.C., 2005. Tissue sensing adaptive radar for breast cancer detection-Experimental investigation of simple tumor models. IEEE Transactions on Microwave theory and Techniques, 53(11), pp.3312-3319.
[59] Jayalakshmi, C. and Sathiyasekar, K., 2016, May. Analysis of brain tumor using intelligent techniques. In 2016 International Conference on Advanced Communication Control and Computing Technologies (ICACCCT) (pp. 48-52). IEEE.
[60] Mobashsher, A.T. and Abbosh, A.M., 2016. On-site rapid diagnosis of intracranial hematoma using portable multi-slice microwave imaging system. Scientific reports, 6, p.37620.
[61] Amineh, R.K., Ravan, M., Trehan, A. and Nikolova, N.K., 2010. Near-field microwave imaging based on aperture raster scanning with TEM horn antennas. IEEE Transactions on Antennas and Propagation, 59(3), pp.928-940.
[62] Semenov, S., Kellam, J., Althausen, P., Williams, T., Abubakar, A., Bulyshev, A. and Sizov, Y., 2007. Microwave tomography for functional imaging of extremity soft tissues: feasibility assessment. Physics in Medicine & Biology, 52(18), p.5705.
[63] Craddock, I.J., Klemm, M., Leendertz, J., Preece, A.W. and Benjamin, R., 2008, March. Development and application of a UWB radar system for breast imaging. In 2008 Loughborough Antennas and Propagation Conference (pp. 24-27). IEEE.
[64] Gibbins, D., Klemm, M., Craddock, I.J., Leendertz, J.A., Preece, A. and Benjamin, R., 2009. A comparison of a wide-slot and a stacked patch antenna for the purpose of breast cancer detection. IEEE transactions on antennas and propagation, 58(3), pp.665-674.
[65] Federal Communications Commission, 2002. First report and order 02-48. FCC, February.
[66] Ghavami, N., Tiberi, G., Edwards, D.J. and Monorchio, A., 2011. UWB microwave imaging of objects with canonical shape. IEEE Transactions on Antennas and Propagation, 60(1), pp.231-239.
[67] Balanis, C.A., 2016. Antenna theory: analysis and design. John wiley & sons.
[68] Pozar, D.M., 1992. Microstrip antennas. Proceedings of the IEEE, 80(1), pp.79-91.
[69] Boualleg, A. and Merabtine, N., 2005. Analysis of radiation patterns of rectangular microstrip antennas with uniform substrate. Semiconductor Physics Quantum Electronics & Optoelectronics.
[70] Paul, L.C. and Sultan, N., 2013. Design, simulation and performance analysis of a line feed rectangular micro-strip patch antenna. International Journal of Engineering Sciences & Emerging Technologies, 4(2), pp.117-126.

[71] Udofia, K.M. and Saturday, J.C., 2019. Parametric comparison of circular, triangular and rectangular dual band microstrip antennas for wireless communication. European Journal of Engineering and Technology Vol, 7(3).
[72] Errifi, H., Baghdad, A., Badri, A. and Sahel, A., 2015. Design and analysis of directive microstrip patch array antennas with series, corporate and series-corporate feed network. International Journal of Electronics and Electrical Engineering, 3(6), pp.416-423.
[73] Ekke, V.R. and Zade, P.L., 2016. Design and Implementation of T-junction Triangular Microstrip Patch Antenna Array for Wireless Applications. International Journal of Engineering and Technology, 8(5), pp.2105-2114.
[74] Yu, Y., Huang, Z., Zheng, C. and Wu, Y., 2014. A Miniature Antenna for 2.45 GHz RFID Tag. JCP, 9(2), pp.404-411.
[75] AL-Husain, Z.A.A., 2014. Design of Ultra-Wideband Microstrip Antennas with Slots and Fractal Based Ground Plane. Al-Rafidain University College For Sciences, (34), pp.244-258.
[76] Semenov, S.Y. and Corfield, D.R., 2008. Microwave tomography for brain imaging: Feasibility assessment for stroke detection. International Journal of Antennas and Propagation, 2008.
[77] Tiberi, G., Ghavami, N., Edwards, D.J. and Monorchio, A., 2011. Novel techniques for UWB microwave imaging of objects with canonical shape. In Progress in Electromagnetics Research Symposium, PIERS 2011 Marrakesh (pp. 808-812).
[78] Aldhaeebi, M. and Elshafiey, I., 2014, March. New antenna design for hyperthermia treatment of human head. In 2014 UKSim-AMSS 16th International Conference on Computer Modelling and Simulation (pp. 96-100). IEEE.
[79] Schwerdt, H.N., Chae, J. and Miranda, F.A., 2012, July. Wireless performance of a fully passive neurorecording microsystem embedded in dispersive human head phantom. In Proceedings of the 2012 IEEE International Symposium on Antennas and Propagation (pp. 1-2). IEEE.
[80] Mahinda, H.A.M. and Murty, O.P., 2009. Variability in thickness of human skull bones and sternum-An autopsy experience. Journal of Forensic Medicine and Toxicology, 26(2), pp.26-31.
[81] Human skull/ Authored by: Boundless.com from https://courses.lumenlearning.com/boundless-ap/chapter/the-skull/.
[82] Lazebnik, M., Madsen, E.L., Frank, G.R. and Hagness, S.C., 2005. Tissue-mimicking phantom materials for narrowband and ultrawideband microwave applications. Physics in Medicine & Biology, 50(18), p.4245.

[83] Sperandio, M., Guermandi, M. and Guerrieri, R., 2011. A four-shell diffusion phantom of the head for electrical impedance tomography. IEEE transactions on biomedical engineering, 59(2), pp.383-389.
[84] Akter, M., Hirai, T., Hiai, Y., Kitajima, M., Komi, M., Murakami, R., Fukuoka, H., Sasao, A., Toya, R., Haacke, E.M. and Takahashi, M., 2007. Detection of hemorrhagic hypointense foci in the brain on susceptibility-weighted imaging: clinical and phantom studies. Academic radiology, 14(9), pp.1011-1019.
[85] Mobashsher, A.T., Abbosh, A.M. and Wang, Y., 2014. Microwave system to detect traumatic brain injuries using compact unidirectional antenna and wideband transceiver with verification on realistic head phantom. IEEE Transactions on Microwave Theory and Techniques, 62(9), pp.1826-1836.
[86] Mobashsher, A.T., Nguyen, P.T. and Abbosh, A., 2013, December. Detection and localization of brain strokes in realistic 3-D human head phantom. In 2013 IEEE MTT-S International Microwave Workshop Series on RF and Wireless Technologies for Biomedical and Healthcare Applications (IMWS-BIO) (pp. 1-3). IEEE.
[87] Symeonidis, S., Whittow, W.G. and Panagamuwa, C., 2017. Design and characterization of a three material anatomical bone phantom for implanted antenna applications.
[88] Meaney, P.M., Fox, C.J., Geimer, S.D. and Paulsen, K.D., 2017. Electrical characterization of glycerin: Water mixtures: Implications for use as a coupling medium in microwave tomography. IEEE transactions on microwave theory and techniques, 65(5), pp.1471-1478.
[89] Persson, M., Fhager, A., Trefna, H.D., Yu, Y., McKelvey, T., Pegenius, G., Karlsson, J.E. and Elam, M., 2014. Microwave-based stroke diagnosis making global prehospital thrombolytic treatment possible. IEEE Transactions on Biomedical Engineering, 61(11), pp.2806-2817.
[90] Scapaticci, R., Di Donato, L., Catapano, I. and Crocco, L., 2012. A feasibility study on microwave imaging for brain stroke monitoring. Progress In Electromagnetics Research, 40, pp.305-324.
[91] Koutsoupidou, M., Kosmas, P., Ahsan, S., Miao, Z., Sotiriou, I. and Kallos, T., 2017, September. Towards a microwave imaging prototype based on the DBIM-TwIST algorithm and a custom-made transceiver system. In 2017 International Conference on Electromagnetics in Advanced Applications (ICEAA) (pp. 1004-1007). IEEE.
[92] Shea, J.D., Kosmas, P., Hagness, S.C. and Van Veen, B.D., 2010. Three-dimensional microwave imaging of realistic numerical breast phantoms via a multiple-frequency inverse scattering technique. Medical physics, 37(8), pp.4210-4226.

[93] Azghani, M., Kosmas, P. and Marvasti, F., 2014. Microwave medical imaging based on sparsity and an iterative method with adaptive thresholding. IEEE transactions on medical imaging, 34(2), pp.357-365.
[94] Enders, P., 2009. Huygens' principle as universal model of propagation. Latin-American Journal of Physics Education, 3(1), p.4.
[95] Tiberi, G.I.A.N.L.U.I.G.I., Ghavami, N., Edwards, D.J. and Monorchio, A.G.O.S.T.I.N.O., 2011. Ultrawideband microwave imaging of cylindrical objects with inclusions. IET microwaves, antennas & propagation, 5(12), pp.1440-1446.
[96] Zamani, A. and Abbosh, A.M., 2015, November. Clutter rejection techniques for microwave head imaging. In 2015 International Symposium on Antennas and Propagation (ISAP) (pp. 1-4). IEEE.
[97] Klemm, M., Craddock, I.J., Leendertz, J.A., Preece, A. and Benjamin, R., 2008. Improved delay-and-sum beamforming algorithm for breast cancer detection. International Journal of Antennas and Propagation, 2008.
[98] Mustafa, S., Mohammed, B. and Abbosh, A., 2013. Novel preprocessing techniques for accurate microwave imaging of human brain. IEEE Antennas and Wireless Propagation Letters, 12, pp.460-463.
[99] Loizou, C.P., Theofanous, C., Pantziaris, M. and Kasparis, T., 2014. Despeckle filtering software toolbox for ultrasound imaging of the common carotid artery. Computer methods and programs in biomedicine, 114(1), pp.109-124.
[100] Moore, H. and Hui-Sheng, G., 2011. MATLAB Practical Guide.
[101] Documentation, M.A.T.L.A.B., 2012. Matlab documentation. Matlab, p.R2012b.
[102] Fear, E.C., Li, X., Hagness, S.C. and Stuchly, M.A., 2002. Confocal microwave imaging for breast cancer detection: Localization of tumors in three dimensions. IEEE Transactions on biomedical engineering, 49(8), pp.812-822.
[103] howstuffworks/ about analysis of capacitance scanning from https://computer.howstuffworks.com/fingerprint-scanner.htm.
[104] Vrba, J. and Vrba, D., 2013. Temperature and frequency dependent empirical models of dielectric properties of sunflower and olive oil. Radioengineering, 22(4), pp.1281-1287.
[105] Bansal, N., Dhaliwal, A.S. and Mann, K.S., 2015. Dielectric properties of corn flour from 0.2 to 10 GHz. Journal of Food Engineering, 166, pp.255-262.
[106] Tiberi, G., Ghavami, N., Edwards, D.J. and Monorchio, A., 2012. UWB body area network channel modeling: An analytical approach. AEU-International Journal of Electronics and Communications, 66(11), pp.913-919.

[107] Tiberi, G. and Raspa, G., Ubt SRL, 2019. Apparatus for testing the integrity of mammary tissues. U.S. Patent 10,349,863.
[108] Moerman, A. and Wouters, P., 2010. Near-infrared spectroscopy (NIRS) monitoring in contemporary anesthesia and critical care. Acta anaesthesiologica Belgica. 61(4), pp.185-194.